THE SPATIAL DISTRIBUTION OF THE DIFFUSE COMPONENT OF COSMIC X-RAYS

Daniel Alan Schwartz

Department of Physics

UNIVERSITY OF CALIFORNIA
SAN DIEGO

La Jolla, California

Department of Physics

Space Physics Group

THE SPATIAL DISTRIBUTION OF THE DIFFUSE COMPONENT OF COSMIC X-RAYS

Daniel Alan Schwartz

Department of Physics

University of California, San Diego

La Jolla, California, 92037

A dissertation submitted in partial satisfaction of the
requirements for the degree of Doctor of Philosophy
in Physics

September 1969

Chairman: Professor Laurence E. Peterson

UNIVERSITY OF CALIFORNIA

San Diego

The Spatial Distribution of the Diffuse Component of Cosmic X-rays

A dissertation submitted in partial satisfaction of the requirements for the degree of Doctor of Philosophy in Physics

by

Daniel Alan Schwartz

Committee in charge:

Professor Laurence E. Peterson, Chairman
Professor James R. Arnold
Professor Jules A. Fejer
Professor Robert J. Gould
Professor Carl E. McIlwain

1969

We approve the dissertation of Daniel Alan Schwartz, and find it acceptable in quality and form for publication on microfilm:

Jules A. Feijer

Carl P. McElwain

Robert J. Gould

James P. Arnold

Laurence Petticoon

Committee Chairman

University of California, San Diego

TABLE OF CONTENTS

LIST OF TABLES

LIST OF FIGURES

ACKNOWLEDGMENTS

This thesis represents only a portion of output from the S-57 X-ray telescope project. Thus I include here the acknowledgments of many previous UCSD X-ray and γ-ray astronomy group publications: to Ball Brothers Research Corporation for construction, qualification and integration of the UCSD experiment and the Orbiting Solar Observatory; to the OSO project management, data acquisition, and satellite operations personnel at Goddard Space Flight Center; and to the many graduate student and technical personnel at UCSD who participated in laboratory and balloon-borne checkouts of the prototype X-ray telescope prior to launch.

Professor Laurence E. Peterson originally conceived the experiment and detector design, and suggested this thesis problem. He has given me invaluable guidance and reassurance, and generous support. I appreciate conversations with A. Wolfe, who has pointed out the cosmological significance of this data; H. Hudson and D. McKenzie, who have analyzed the solar X-ray data; and A. Jacobson, who conducted balloon-borne investigations of the detector and shield.

The data reduction and analysis have depended heavily on the diligence of many undergraduate assistants. Of these, W. Alberty and S. Bossert have especially acquired independent competence in many phases of the reduction coding and checkout, and J. Rosenthal has carefully typed this manuscript.

L. Huszar provided much information on the coding and debugging of computer routines. The UCSD Computer Center provided facilities for data reduction.

I acknowledge generous support from NASA Grant NGR-05-005-003, and Goddard Space Flight Center Contract NAS 5-3177.

VITA

[redacted] - Born - [redacted]

1963 - B.S., Washington University, St. Louis

1963-1969 - Research Assistant, Department of Physics,
University of California, San Diego

1966 - M.S., University of California, San Diego

1968-1969 - Unpaid Teaching Assistant, Department of Physics,
University of California, San Diego

PUBLICATIONS

"Cosmic-Ray Produced γ-Rays to 10 Mev," D. A. Schwartz, L. E. Peterson, Trans. AGU, 46, 129 (1965).

"Atmospheric Gamma Rays Produced by Cosmic Rays to 3 gm/cm^2 at $\lambda = 40^\circ$," D. A. Schwartz, L. E. Peterson, Trans. AGU, 47, 158 (1966).

"The Upper Limit Solar Gamma Ray Spectrum to 10 Mev," L. E. Peterson, D. A. Schwartz, R. M. Pelling, and D. McKenzie, JGR, 71, 5778 (1966).

"Satellite Observations of Discrete Cosmic X-Ray Sources," D. A. Schwartz, H. S. Hudson, L. E. Peterson, Bull. Am. Phys. Soc., 12, 1058 (1967).

"Observations of X-Rays in the Range 7.7-210 keV from the Quiet Sun and from Solar Active Regions," H. S. Hudson, D. A. Schwartz, and L. E. Peterson, Bull. Am. Phys. Soc., 12, 1066 (1967).

"Hard Solar X-Ray Bursts Observed by OSO-III," H. S. Hudson, D. A. Schwartz, and L. E. Peterson, A.J., 73, 5 (1968).

"Solar and Cosmic X-Rays Above 7.7 keV," H. S. Hudson, L. E. Peterson, and D. A. Schwartz, Solar Physics, 6, 205-215 (1968).

"Observations of Solar X-Rays above 7.7 keV and Their Correlation with Ionospheric Disturbances," H. S. Hudson, D. A. Schwartz, and L. E. Peterson, Trans. AGU, 49, 274 (1968).

"Observations of Cosmic X-Ray Sources in the 10-250 keV Range," L. E. Peterson, A. S. Jacobson, R. M. Pelling, and D. A. Schwartz, Can. J. of Phys., 46, S437 (1968).

"The Time Structure of Solar X-Ray Bursts Above 7.7 keV," H. S. Hudson, L. E. Peterson, and D. A. Schwartz, Space Research (to be published).

"Satellite Observations of Albedo X-Rays Between 7.7 and 210 keV," D. A. Schwartz, H. S. Hudson, L. E. Peterson, Trans. AGU, 49, 720 (1968).

"X-Ray Observations of Limb Flares," H. S. Hudson, D. A. Schwartz, L. E. Peterson, H. Zirin, and W. H. Ingham, Trans. AGU, 49, 725 (1968).

"The Hard Solar X-Ray Spectrum Observed from the Third Orbiting Solar Observatory," H. S. Hudson, L. E. Peterson, and D. A. Schwartz, Ap. J., 157, 389 (1969).

FIELDS OF STUDY

Major Field: Physics

Studies in Classical Electrodynamics
Professors Francis R. Halpern and Nguyen-Huu Xuong

Studies in Advanced Mechanics
Professor Carl Eckart

Studies in Quantum Mechanics
Professors Norman M. Kroll and Harry Suhl

Studies in Astrophysics
Professor E. Margaret Burbidge

ABSTRACT OF THE DISSERTATION

The Spatial Distribution of the Diffuse Component of Cosmic X-rays

by

Daniel Alan Schwartz

Doctor of Philosophy in Physics

University of California, San Diego, 1969

Professor Laurence E. Peterson, Chairman

The Third Orbiting Solar Observatory (OSO-III) carried an X-ray detector collimated to a 23° full width at half maximum aperture, and sensitive to photons between 7.7 and 210 keV. I have analyzed the data in five logarithmically spaced energy channels between 7.7 and 110 keV to study the spectrum and angular distribution of the diffuse component of cosmic X-rays. (I use the term "diffuse," although this experiment cannot eliminate the possibility that the X-rays actually emanate from numerous discrete sources.) Because this single instrument has scanned almost the entire sky, I can confidently look for relative angular variations even in the presence of systematic errors.

I subtract the following sources of background from the raw count rates: phototube noise, counts due to cosmic ray induced γ-rays, and counts due to γ-rays associated with the β-decay of Na^{24}. At 10 keV about 98 percent of the counts represent diffuse X-rays; at 85 keV only about 25 percent remain after background correction. The programs eliminate a large portion of the data because of possible contamination by charged particles, albedo X-rays, solar X-rays, and X-rays from the discrete galactic sources.

A program compiles counts within 30° of the galactic poles to study the energy spectrum. Considering photon counting statistics and estimated errors in the background correction, the four lowest channels have standard deviations from 1.5 to 3 percent, and 14 percent for the 65-110 keV channel. A power law with a constant index cannot represent the data. Considering the detector efficiency and resolution, the lowest three channels fit a power law of index 1.7 ± 0.1 with a normalization constant 16.7 photons $(\text{keV})^{0.7}$ $(\text{cm}^2 \text{ sec ster})^{-1}$. A discontinuity of 0.6 to 1.5 in the index between 32 and 46 keV can then fit the two highest channels.

After avoiding all known galactic discrete sources, only 20° strips around longitudes 150° and 230° remain on the galactic plane. These areas have an excess emission in the lowest channel of 0.012 ± 0.004 photons $(\text{cm}^2 \text{ sec rad})^{-1}$ at 10 keV, if interpreted as a line source. The present experiment cannot distinguish between a point or a line source.

No other anisotropies appear in the data. Whether the diffuse component arises from inverse Compton scattering in intergalactic

space, or from the integrated effect of individual galaxies, sources at distances of the order of the Hubble radius must contribute significantly. Limits as low as five percent to inhomogeneities or to a 12-hour periodic component apply to much of the sky. The limit of one percent to the 24-hour period in any direction corresponds to an upper limit of 800 km/sec for the earth's resultant velocity relative to any rest frame in which the X-rays appear isotropic. The lack of lumpiness sets a lower limit of 10^5 to the number of necessary discrete sources in the sky, if discrete sources produce the measured diffuse X-rays.

I. INTRODUCTION

Many experiments have shown the existence of a diffuse, apparently isotropic component of extraterrestrial X-rays in the energy range 0.25 to 10^5 keV. The data between 0.25 and 100 keV have resulted from rocket-borne counters, most effective below 15 keV, and balloon-borne counters, most sensitive above 30 keV. The absence of anisotropy, to roughly 20 percent limits, strongly suggested that these X-rays have extragalactic origin. Because of the inadequacy of local sources to provide the measured diffuse X-ray strength, and because of the transparency of the interstellar and intergalactic media above a few keV, a substantial contribution to the X-ray intensity at earth must originate at redshifts $z = \Delta\lambda/\lambda \geq 1$. This thesis presents measurements of the angular structure and energy spectrum of diffuse X-rays between 7.7 and 110 keV. A single X-ray telescope successfully operating for a year aboard OSO-III has provided data with an order of magnitude greater accuracy than obtained on previous individual experiments. The X-ray telescope scanned most of the celestial sphere in that time, thus a study of the angular dependence provides information on the isotropy and homogeneity of the universe over the entire sky. Although several different theories might explain the diffuse component, the measurement of the spectrum can provide some constraints, and gives values for physical parameters on a cosmological scale if one assumes a given emission mechanism.

A. Diffuse Cosmic X-rays

Electromagnetic quanta can travel along straight lines through space, preserving the direction of their emission. In the optical and radio range this property includes the penetration of the atmosphere. X-ray and gamma ray astronomy, suggested as a valuable source of data by radio and cosmic ray evidence for high energy processes in galaxies [Morrison (1958)] and by explosive events in stellar evolution [Savedoff (1959)], had to await the development of vehicles for carrying detectors above the earth's atmosphere. Sounding rocket observation of solar ultra-violet and soft X-rays in 1948 [Burnight (1949)], and balloon observation of hard solar X-rays during flares [Peterson and Winckler (1959)], showed the feasibility of detecting extra-terrestrial X-rays. On June 18, 1962, American Science and Engineering (ASE) rocket-borne Geiger counters sensitive to 1.6 to 6.2 keV X-rays, detected a strong source of such X-rays in the galactic center region, superimposed on a sky background which seemed isotropic within the statistical accuracy of roughly 20 percent [Giacconi, et al. (1962)]. Since then many rocket experiments have detected a total of about 25 localized cosmic X-ray sources [Friedman, et al. (1967)]. These sources appear as point objects to a detector with spatial resolution of 1^{o}. The Crab Nebula does have an angular extent of about one arc minute [Bowyer, et al. (1964); Oda, et al. (1967)]; no measurement has shown finite size for any other discrete object, and an upper limit of 20 arc seconds exists for Sco X-1 [Gursky, et al. (1966)].

In all these experiments the count rate did not become zero for any part of the sky, even after subtracting background due to charged particles. This background may consist of direct counting of cosmic rays or geomagnetically trapped particles, or of X-rays produced by cosmic ray interactions in the detector vehicle or in the earth's atmosphere. The relative importance of these background components depends on the exact vehicle and detector configuration, thus preventing detailed intensity versus celestial position comparisons between different experiments.

To establish an apparently isotropic background count rate as due to cosmic X-rays required much indirect evidence. Balloon-borne experiments provided evidence for a diffuse component of X-rays incident on the atmosphere [Rocchia, et al. (1966); Hudson, et al. (1966); Bleeker, et al. (1968)]. Figure 1 schematically shows count rates as a function of the residual atmospheric depth for an X-ray detector. X-rays in the atmosphere result from electron-photon degradation of the primary cosmic ray energy. The photons show a transition maximum at about 90 gm/cm^2, and then decrease at higher altitudes. However, within a few mean free paths of the top of the atmosphere the count rate again increases, and with the depth dependence expected due to attenuation of an extra-terrestrial source. From the total count rate R_1 at ceiling, one subtracts an extrapolation R_2 of the atmospheric X-rays, and the true detector background R_3 (the count rate with the aperture blocked) and divides by the average atmospheric absorption:

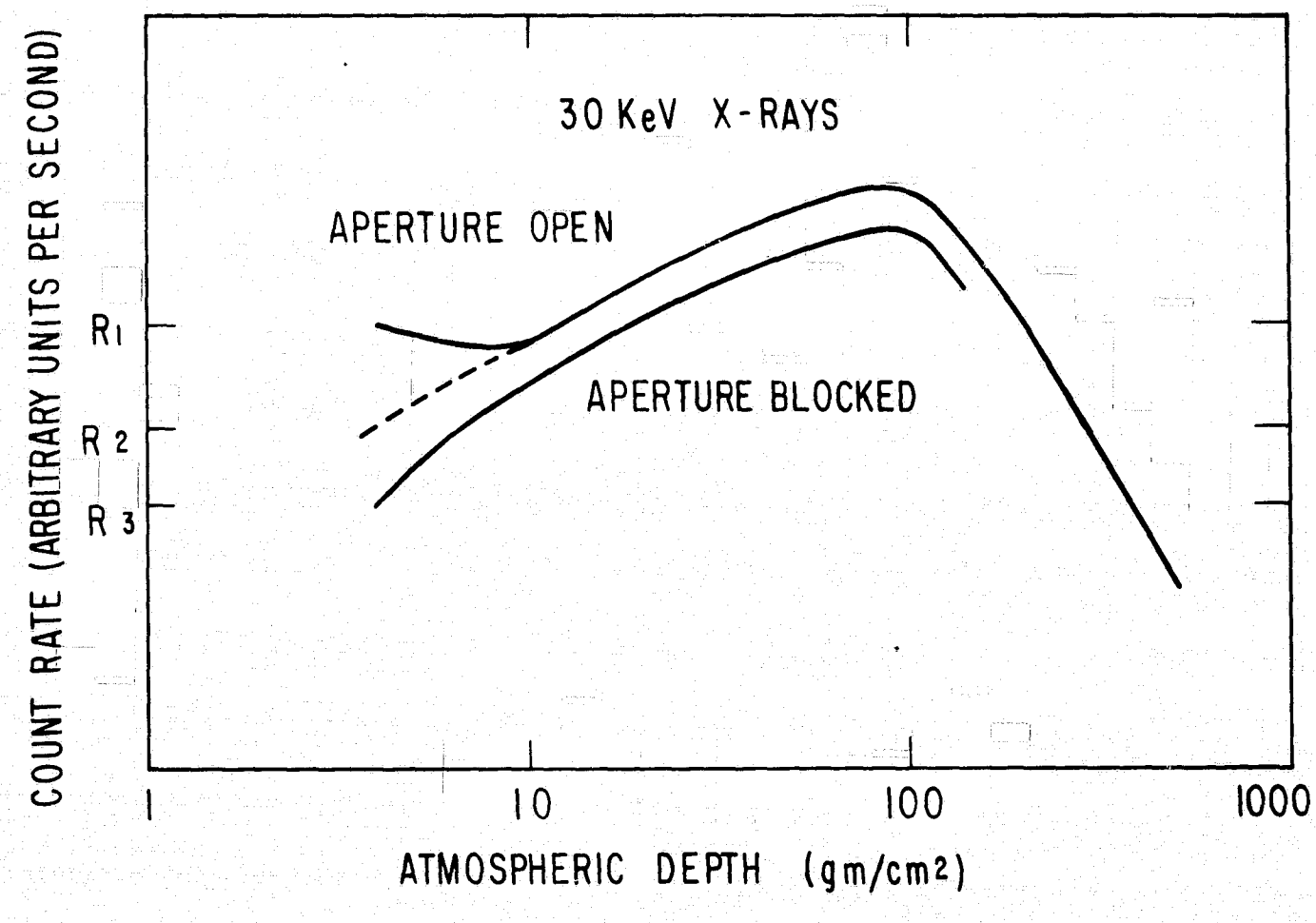

Fig. 1 Qualitative picture of count rates of a vertically mounted, wide-aperture telescope. Diffuse X-rays cause the turn-up of the "aperture open" curve. One must estimate the atmospheric contribution (dashed line) to deduce the diffuse intensity.

$$R\ (\text{cosmic X-rays at top of atmosphere}) = (R_1 - R_2 - R_3)\ e^{\tau}, \qquad (1)$$

τ = average X-ray optical depth at ceiling.

Any effect due to cosmic rays should show a latitude dependence. A Leiden-Nagoya group flew identical X-ray telescopes from balloons at geomagnetic latitudes 53°N and 25°N [Bleeker, et al. (1968)]. These had a NaI(Tl) scintillation counter detector, surrounded by a passive collimator and a plastic veto scintillator. A rotating collimator periodically blocked the aperture to give the background estimate. The deduced diffuse intensities, in the range 30-150 keV, agreed very well within the estimated accuracy of about 20 percent. For comparison, their data show a factor of 5 higher flux of 20-40 keV atmospheric X-rays at 7 gm/cm^2 at the northern latitude.

A Tokyo-Nagoya group constructed a rocket-borne proportional counter with a rotating collimator having three different apertures [Matsuoka, et al. (1968)]. They found a portion of the count rate directly proportional to the aperture solid angle, and therefore due to a diffuse intensity entering the aperture.

The Ranger-III gamma ray experiment [Arnold, et al. (1962); Metzger, et al. (1964)] provided key evidence that the diffuse component originates outside the earth. The rates of a scintillation counter, pulse height analyzed between 70 keV and about 1 Mev, with phoswich rejection of charged particles, did not vary from the outer radiation belts to about 60 earth radii. Gamma rays produced in the spacecraft plus any diffuse component should thus account for the observed rates. In mid-flight a boom extended the detector 6 feet

from the satellite, so that the solid angle of the satellite subtended at the detector decreased by a factor of 13. Count rates decreased by less than factors of 2 and 3 at 0.2 and 1 Mev. After eliminating local radioactivity or the Sun as contributors, the experimenters concluded that an extra-planetary component provided most of the counts in the extended position.

A Lawrence Radiation Laboratory group [Seward, et al. (1967)] combined data from a proportional counter rocket flight and a scintillation counter flight and classified counts as high galactic latitude ($|b|>40^{\circ}$) or low galactic latitude ($|b|<40^{\circ}$, and including the plane). The two spectral intensities between 4 and 40 keV differed by only the 10 percent statistical accuracy, thus giving a 20 percent upper limit to a galactic emission. This indicates that the diffuse X-rays must originate within a sphere of radius the order of the scale height of the galactic disk, about 100 pc, or originate in metagalactic space. The complete transparency of the interstellar medium to X-rays above a few keV [Felten and Gould (1966)] rules out the former possibility because then special emission processes would have to take place only in the solar neighborhood. In fact, no likely mechanism can explain the total diffuse intensity in terms of emission within our galaxy or halo [Gould (1965); Gould and Burbidge (1965); Felten and Morrison (1966)].

Gould (1967) compiled the spectral measurements of many observers, and fit a power law $N(E) = K E^{-2.3}$ to the differential number spectrum between 1 keV and 1 Mev. Synchrotron or Compton effect emission by a power law spectrum of relativistic electrons

(the term "electrons" includes positrons) can give such a power law spectrum of high energy photons. The scatter of data obtained in different experiments and caused by large systematic errors allowed this single power law fit. Individual experiments, over perhaps one decade or less energy range, often resulted in a smaller spectral index. Recent experiments [Henry, et al. (1968); Gorenstein, et al. (1969); Boldt, et al. (1969); Bleeker and Deerenberg (1969)] have suggested a discontinuity in power law index of from 0.5 to 1.0, occurring between 10 and 60 keV. I discuss these other measurements further, together with the present results, in Chapter III.

B. Theories of the Diffuse Component

Currently the two theories most discussed explain the diffuse component as the observation of unresolved point sources in individual galaxies, or of Compton scattering of high energy electrons by an ambient intergalactic photon gas, namely the measured microwave radiation attributed to a 3° K blackbody. As recent reviews have pointed out [Gould (1967); Morrison (1967)], the diffuse component then contains information about energetic processes in galaxies, or about intergalactic space. For either theory sources at distances of the Hubble radius, $R_H = c/H \sim 10^{28}$ cm, must contribute significantly, therefore the spectrum and the intensity also carry information on evolutionary effects and the angular distribution provides information on the large scale structure of the universe. I discuss the theories basically to see what angular structure they predict.

Considering both the diffuse and discrete cosmic X-ray sources, Gould and Burbidge (1965) reviewed processes that can produce a continuous X-ray spectrum: electron bremsstrahlung by Coulomb interactions or by synchrotron radiation, and Compton scattering of high energy electrons by low energy photons. The spectral photon intensity

$$\frac{dN}{dE}(E) \quad \left[\frac{\text{photons}}{\text{cm}^2 \text{ ster sec keV}}\right] = \frac{1}{E}\frac{dI}{dE}(E) = \frac{1}{4\pi E}\int_0^\infty \frac{dP}{dE}\, dr \,, \qquad (2)$$

where $I(E)$ represents the spectral energy intensity, dP the power lost into the energy interval E to $E+dE$ by interactions in a unit volume of space, and $1/4\pi$ converts a total flux to a directional intensity under the assumption that, averaged over a large volume, the local high energy electron intensity appears isotropic and the target particles or fields do not have any preferred direction. In practice, the integration extends only over some region in which the process of interest takes place. The calculations generally use a power law representation of the high energy electron spectrum:

$$n(\gamma) \quad \left[\frac{\text{electrons}}{(\text{interval of } \gamma)\ \text{cm}^3}\right] = K\,\gamma^{-m} \qquad (3)$$

with γ the ratio of total to rest mass energy. The spectral index m may depend on the range of γ under consideration. This shape agrees with direct observations of cosmic-ray electrons [Fanselow (1968)], with the synchrotron explanation of the power law radio emission from galaxies, and with the calculated electron spectrum due to secondary production from the observed power law spectrum of cosmic ray protons [Gould and Burbidge (1965)].

$$\frac{dP}{dE} = \int_1^\infty n(\gamma)\ S_x(\gamma,E)d\gamma,$$

where $S_x(\gamma,E)dE$ gives the rate at which an electron of energy γ loses energy into (E, E+dE) in an arbitrary process denoted by x. The smearing of the exact spectral loss $S_x(\gamma,E)$ by the power law electron spectrum generally allows the approximation that the total power emitted by the electron,

$$S_x(\gamma) = \int_0^\infty S_x(\gamma,E)dE$$

occurs at some characteristic photon energy E_x, of the order of the E for which $S_x(\gamma,E)$ has a maximum:

$$S_x(\gamma,E) = S_x(\gamma)\ \delta(E-E_x).$$

$S_x(\gamma)$ now depends on the cross section for the process x, and the parameters of the target. Gould and Burbidge (1965) give the average loss rates

$$S_B(\gamma) = 4\ m_o c^3 r_o^2 \alpha\ n_H \gamma\ \ln(1/\alpha), \quad E_B = mc^2\gamma$$

for bremsstrahlung in an average local hydrogen density n_H;

$$S_s(\gamma) = \frac{2}{3}\ c r_o^2\ H^2\gamma^2, \quad E_s = h\nu_L\ \gamma^2$$

for synchrotron radiation in the presence of a magnetic field of mean square strength H^2. Felten and Morrison (1966) give

$$S_c(\gamma) = \frac{4}{3}\left(\frac{8\pi}{3} r_o^2\right) c\rho\gamma^2, \quad E_c = 3.6\, kT\gamma^2$$

for Compton scattering by a blackbody distribution of photons with energy density ρ and temperature T. The classical electron radius $r_o = \frac{e^2}{m_o c^2} = 2.8 \times 10^{-13}$cm, $\alpha = 1/137$, and the Larmor frequency

$$\nu_L = \frac{eH}{2\pi m_o c}.$$

The intensity of the various processes depends on the dr integration in the given direction:

$$\left(\frac{dN}{dE}\right)_B = \frac{c r_o^2 \alpha \ln 1/\alpha}{\pi m_o c^2} \int_o^\infty \left(\frac{m_o c^2}{E}\right)^m K n_H dr \quad \text{for } E > m_o c^2, \qquad (4)$$

$$\left(\frac{dN}{dE}\right)_S = \frac{2c r_o^2}{12\pi\sqrt{E}} \int_o^\infty \left(\frac{2\pi m_o c}{he}\right)^{\frac{3-m}{2}} \frac{KH^{\frac{1+m}{2}}}{E^{m/2}} dr, \qquad (5)$$

$$\left(\frac{dN}{dE}\right)_C = \frac{8 r_o^2 c}{18\sqrt{E}} \int_o^\infty K\rho\, T^{\frac{m-3}{2}} \frac{(3.6k)^{\frac{m-3}{2}}}{E^{m/2}} dr. \qquad (6)$$

Rigorously, K, m, n_H, H, ρ, and T all depend on position in space, varying with r and also with the angular coordinates. Except for some measurements of galactic hydrogen, one has no detailed information on spatial structure, and values for the parameters represent an average in some volume. Then, independently of the production mechanism, angular variations depend on

$$\int_0^{R_{max}(\theta)} dr = R_{max}(\theta) ,$$

the distance viewed from earth through some astronomical structure. Gould and Burbidge (1965) discussed the electron spectrum in detail, and showed that bremsstrahlung or synchrotron radiation either within the galactic halo or metagalactic space fall at least five orders of magnitude short of the 10-100 keV diffuse intensity. Felten and Morrison (1966) showed that metagalactic Compton scattering of $T = 3^{\circ}K$ blackbody photons can give the required diffuse intensity strength. Their model requires a 100-fold larger metagalactic electron flux than derived by straightforward estimates of halo electron leakage or injection by radio galaxies; but they suggest either the presence of more electrons than implied by equipartition arguments in radio galaxies or even a primordial universal electron flux. The Compton model seems attractive because it can explain the spectral shape between 1 and 10^5 keV by relation to a single electron spectrum. This model also gives information about magnetic fields. Normalizing the electron density to the Compton X-rays, the observed (or upper limit) synchrotron radio emission constrains H through equation (5).

In considering complex models of angular variations, note that a measured value of a total number or total energy density of electrons correlates any variation of K and m. Also, because the ambient magnetic field, photon, and gas densities determine the equilibrium electron spectrum, their associated parameters cannot vary strictly independently of K and m.

If metagalactic Compton photons produce the measured diffuse component, cosmological effects deserve consideration and the dr integration in equation (6) replacement by an integration over the red shift parameter $z = \Delta\lambda/\lambda$ from $z = 0$ to some z_{max} where the X-ray optical depth becomes greater than unity. The observed spectrum has the emitted spectral shape for a positive index (decreasing) power law [Felten (1965)], (except below a cutoff which must occur at some low energy). The received intensity at a given energy then depends on

$$\rho_o \, T_o^{\frac{m-3}{2}} \, \bar{K} \, R(\theta,\varphi), \tag{7}$$

with ρ_o and T_o the observed $3^{\circ}K$ blackbody energy density and temperature. I have formally incorporated the angular dependence into the effective radius $R(\theta,\varphi)$ in the direction (θ,φ), which may vary by a factor of 2 or 3 from the Hubble radius depending on the cosmological model [Gould (1967)]. To account for the diffuse magnitude, the average $\bar{K} = \frac{1}{R} \int_o^{z_{max}} K(z)\, dz$ must include evolutionary effects which increase the total amount of energy in relativistic electrons at early stages of the universe. (The function $K(z)$ must also include red shift and time dilation effects.) In a homogeneous isotropic universe, equation (7) gives an isotropic diffuse intensity, except for a possible 24-hour component caused by a Doppler shift due to the earth's motion relative to a stationary reference [Stewart and Sciama (1967)].

The integrated effect of numerous discrete sources [Gould and Burbidge (1963)] can account for the diffuse component. An average

volume density n_x of sources of kind x, times their average spectral emission $J_x(E)$[photons/sec-keV] at some energy E, gives an observed differential number intensity

$$\frac{dN_x}{dE}(E) \left[\frac{\text{photons}}{\text{cm}^2 \text{ sec keV ster}}\right] = \frac{1}{4\pi} J_x(E)\, n_x\, R(\theta,\varphi). \qquad (8)$$

Estimating the distance of the measured discrete galactic sources to obtain their intrinsic X-ray luminosity, guessing their total number in our galaxy, and assuming the resulting $J_x(E)$ represents an average for normal galaxies give estimates roughly 10 percent of the observed intensity [Gould and Burbidge (1963); Hayakawa, et al. (1966); Friedman, et al. (1967)]. Considering the uncertainties, such agreement establishes the plausibility of a discrete source model. Silk (1968) showed how evolutionary effects could increase the intensity due to normal galaxies.

One might associate n_x with any special class of objects. For example, Gould (1967) compared the ratio of the measured X-ray to 178 MHz radio background to the ratio of measured X-ray to 178 MHz flux from the strong radio galaxy M87. These agreed within a factor of 3, so strong radio sources might emit most of the diffuse X-rays.

The above discrete source models have the weakness that they do not predict any spectral shape. Rees (1967), and Bergamini, et al. (1967), have discussed the X-ray spectrum produced by Compton scattering in strong radio sources at large z. Competition for the electron energy loss from synchrotron emission in the magnetic fields assumed in the radio source model, provides the most stringent constraint for

the X-ray production. Felten and Rees (1969) have sketched a model incorporating radio source evolution to illustrate the possibility of distant radio galaxies producing the measured spectrum of diffuse X-rays, including the spectral break, and the constraints then placed on such models by the X-ray observations.

C. Experimental Objectives

Professor Laurence E. Peterson designed the UCSD X-ray telescope for an Orbiting Solar Observatory (OSO) as an instrument to survey the unknown X-ray sky. The necessity for contract specification and extensive instrument qualification before launch froze the design in September, 1963, when very few measurements of cosmic X-ray intensities existed. The instrument has proved to have sufficient dynamic range to give excellent data on diffuse X-rays, as well as on X-rays from the sun [Hudson, et al. (1967, 1968a, b, c, 1969b, c)], the earth [Schwartz, et al. (1968b)], and discrete sources [Schwartz, et al. (1967, 1968a); Peterson, et al. (1967); Hudson, et al. (1969a)].

I use the OSO-III data to prepare a map of the X-ray sky in five energy channels between 7.7 and 110 keV. The UCSD X-ray telescope provides data from the entire celestial sphere for the first time by a single instrument. This enables the detection of angular variations an order of magnitude smaller than possible in previous X-ray experiments, even with some unknown error in a constant background correction. Current microwave observations have about 0.1 percent relative accuracy [Partridge and Wilkinson (1967); Conklin and Bracewell (1967); Conklin (1969); Penzias, et al. (1969)] but cover

only a limited region of the sky, at most a constant declination circle. The present diffuse component study thus provides the first information on the isotropy of the entire celestial sphere at cosmological distances. I eliminate all contributions from the known discrete galactic sources in order to study just the diffuse component. The one year of orbital operation used in this study provides enough photon counts from most of the sky to allow systematic investigation of a connection between the diffuse component and various observed or postulated structures such as the galaxy, a galactic halo, or the local cluster and supercluster. I also look for small (12^{o} radius circles) anomalous areas of X-ray emission. This thesis stresses presentation of the measured X-ray data, rather than deriving a continuous function representation of a "true" diffuse intensity.

I omit most details of the many computer programs and their checkouts written to convert some 300,000,000 bits of OSO-III data into a few physically meaningful numbers. These details will appear along with the submission of reduced data to the National Space Science Data Center, and as part of the OSO-III Contract Final Report.

II. THE X-RAY TELESCOPE ON THE THIRD ORBITING SOLAR OBSERVATORY

A. The X-ray Telescope

The Ball Brothers Research Corporation (BBRC) of Boulder, Colorado, constructed the telescope and performed many of the check-outs [Hicks, et al. (1965)]. A cylindrical NaI(Tl) scintillation counter, 0.5 cm thick with 9.57 cm^2 end area, serves as the central detector. A co-axial cylindrical cup of CsI(Tl) scintillator provides active collimation (Figure 2).

1. Telescope Properties

Figure 3 illustrates the efficiency of the shield as a function of X-ray energy. In an isotropic intensity of unit strength the number of photons incident on the central detector equals the telescope factor T,

$$T = \iint d\Omega \ (\cos\theta \ dA)$$

with the dA integration carried out over the entire crystal surface and the $d\Omega$ integration carried out over all solid angles accessible to the element dA. For photons entering through the aperture the telescope factor T_a = 1.35 cm^2 ster; for photons at any other incident angle (through the solid angle occupied by the shield), T_s = 76.0 cm^2 ster. In an isotropic intensity,

$$76 \ \overline{P}(E) = 1.35 \ R$$

with $\overline{P}(E)$ that average probability for shield penetration at energy E which gives the ratio R of leakage counts to counts entering the forward aperture.

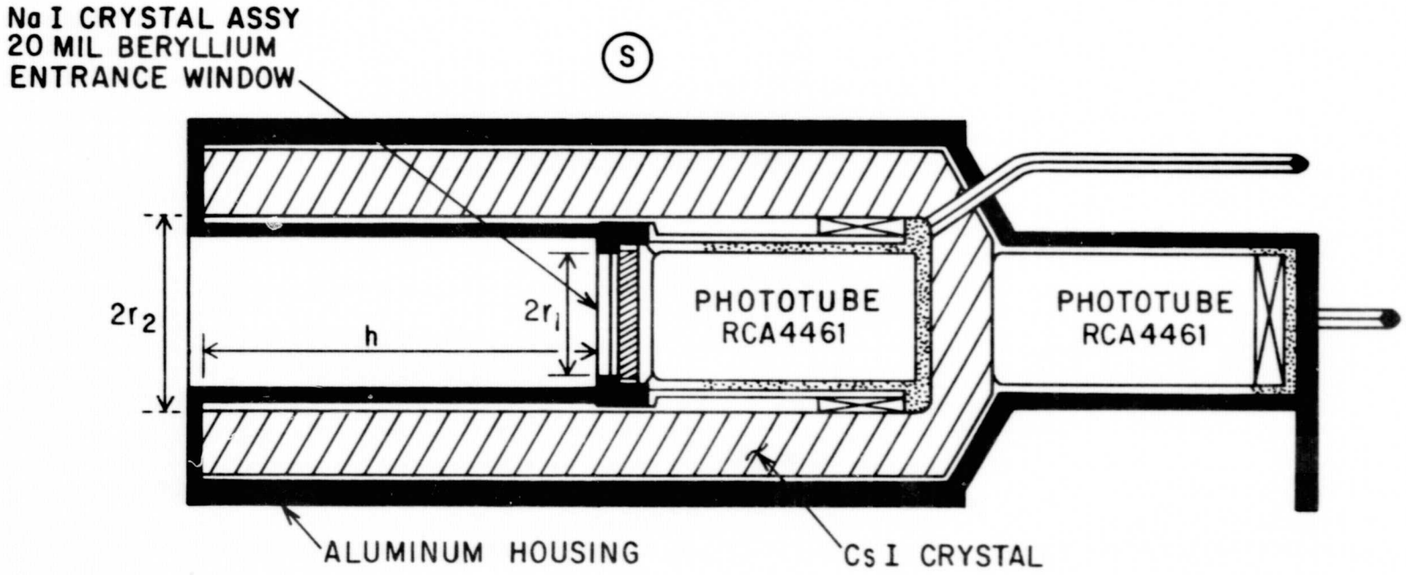

DETECTOR GEOMETRICAL PROPERTIES	
NaI AREA	9.57 cm^2
50 % RESPONSE HALF ANGLE	11.5°
1 % RESPONSE HALF ANGLE	19°
LINE SOURCE RESPONSE FACTOR	3.84 cm^2 rad
TELESCOPE FACTOR	1.35 cm^2 ster
r_1	1.746 cm
r_2	2.70 cm
h	12.32 cm

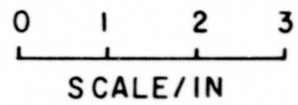

Fig. 2 Cross section of the UCSD X-ray telescope, with the geometrical parameters of the OSO-III flight model. Calibration of the shield occurred with a source in position S.

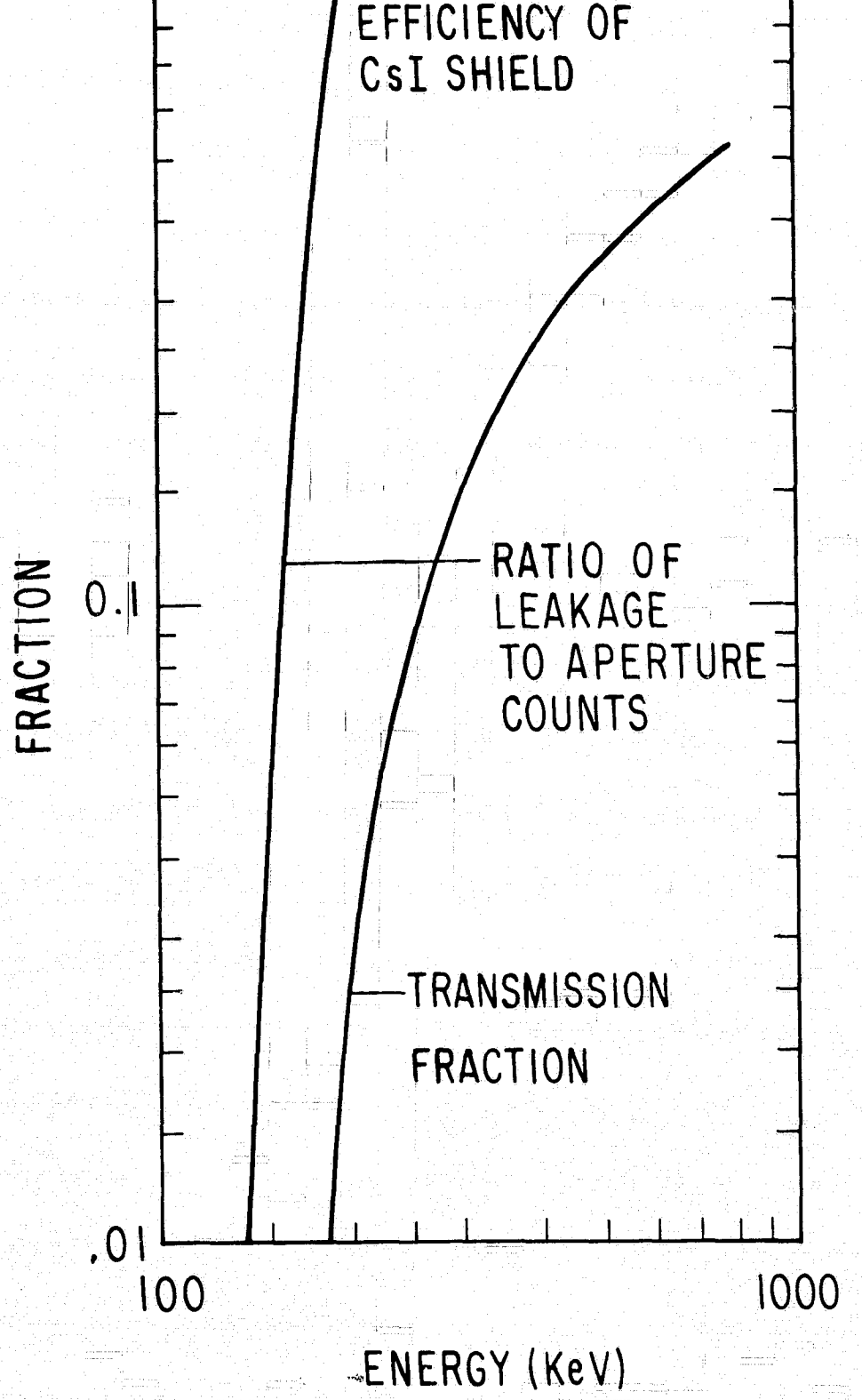

Fig. 3 The ratio of leakage to aperture counts measures the collimating ability by giving the fraction of the measured count rate which did not come from the aperture. The transmission fraction gives the probability that a single photon can penetrate the shield.

$$\bar{P}(E) = e^{-k(E)\bar{\ell}},$$

with k(E) the CsI absorption coefficient per cm at E, and $\bar{\ell}$ an average length through the shield. Even with the minimum length $\bar{\ell}$ = 1.95 cm, R = .01 at 132 keV, 0.1 at 152 keV, and 1.0 at 184 keV. With a more realistic $\bar{\ell} = \sqrt{2}\ 1.95$ (45° incidence to the shield surface), R = .01 at 150 keV and R = 1.0 at 215 keV. Thus the collimating property of the shield breaks down at about 170 keV, still within the highest energy channel. Note that the shield still absorbs half of the normally incident photons at 620 keV, and half of the 45° incident photons up to 1.0 Mev.

The CsI phototube charge pulse can trigger two different anti-coincidence pulses. Nominally, a 100 keV energy loss triggers a 7 μ-sec "lower level discriminator" (LLD) pulse, and a 4 Mev energy loss triggers a 200 μ-sec "upper level discriminator" (ULD) pulse. A minimum ionizing cosmic ray loses 16 Mev passing normally through the 1.95 cm CsI wall. The discriminator level calibrations occurred with a source parallel to the central detector, position S in Figure 2; because of poor light collection a photon interacting near the aperture must lose about twice the nominal energy to trigger the same levels. A long term gain deterioration of the photomultiplier tube had increased the effective energy thresholds by about a factor of 3 at the end of one year in orbit.

A .02 inch (92 mg/cm^2) beryllium window covers the face of the NaI crystal. For X-rays the optical depth $\tau = 53.6\ E^{-3}$, so the window has a slight effect in the case of a steep spectrum, where 5 keV X-rays

may trigger the channel two threshold, due to the broad resolution. The window attenuates a minimum ionizing particle by about 180 keV, but allows electrons of energy 280 to 390 keV or protons of energy about 7.6 Mev to penetrate with a residual 7.7 to 210 keV. Such charged particles thus appear identical to X-ray events.

The pulse height analyzer for the NaI phototube consists of seven threshold discriminators, providing six logarithmically spaced differential energy channels between 7.7 and 210 keV (according to prelaunch calibration), and two integral channels for all events above each of those energy limits (Table 1). The last three columns of Table 1 give factors which multiply the count rate to give the differential spectrum of a point, line, or diffuse source, assumed to have a power law spectrum of index 2.0. These factors change about 1 percent for a 0.2 change in the spectral index.

X-ray interaction occurs with 98 percent probability below the upper edge of channel 6, but falls off to 45 percent probability at the upper edge of channel 7. I calculate the telescope properties for photons below 115 keV by assuming an opaque shield and equal detection of all X-rays incident at any angle on the NaI face. For concentric cylindrical detector and collimator, the detector radius r_1, the collimator radius r_2, and the distance h between detector face and top edge of the collimator determine the angular response. I use the values reported on the final machine drawings, and shown in Figure 2.

The area of the detector perpendicular to a broad parallel beam at an angle θ to the cylinder axis equals $\cos\theta\ A(\theta)$, where $A(\theta)$ equals the area illuminated by the beam, $A(\theta) = \iint_{\text{illuminated area}} dx\ dy$.

Table 1

NaI Analyzer Channel Assignments and Conversion Factors

Channel Number	Function	Energy (keV)	Conversion of Count Rate to Average Spectral Density for $\frac{dn}{dE} \propto E^{-2}$		
			Point Source (photons/cm^2 sec keV)	Line Source (photons/cm^2 sec keV rad)	Diffuse Source (photons/cm^2 sec keV ster)
1	Integral	≥ 7.7			
2	Differential	7.7 - 12.5	.0226	.0565	.160
3	Differential	12.5 - 22	.0116	.0290	.0822
4	Differential	22 - 38	.00687	.0172	.0486
5	Differential	38 - 65	.00406	.0102	.0288
6	Differential	65 - 113	.00229	.00573	.0162
7	Differential	113 - 210	.00115	.00288	.00814
8	Integral	≥ 210			

Figure 4 shows the exact calculation of $\cos\theta\ A(\theta)$, compared with the approximation

$$\cos\theta\ A(\theta) = \cos\theta\ 9.57 \begin{cases} 1 & \theta < \theta_1 = 4.6^\circ \\ 1 - \dfrac{\theta - \theta_1}{3\theta_1} & \theta_1 \leq \theta < 4\theta_1 \\ 0 & 4\theta_1 \leq \theta\ , \end{cases} \qquad (9)$$

and with laboratory measurements on the prototype version of the detector. The laboratory calibration consisted of measuring spectra with a Co^{57} radioactive source, (γ-ray energy 123 keV), about 10 feet from the aperture at various protractor measured angles, and subtracting a background spectrum obtained without the source. The three agree very well; I will generally use the trapezoidal approximation.

As Bracewell and Roberts (1954) discussed for the case of recovering a true distribution from an observed radio brightness distribution, one can measure those (spatial) Fourier components of the true distribution for which the Fourier transform of the telescope response function does not vanish. The slope discontinuity where $A(\theta)$ becomes zero (Figure 4) implies that the Fourier transform approaches zero only asymptotically. Thus with precise knowledge of the telescope optical axis position, sufficient counting statistics, and good background elimination one could obtain information on very rapid angular variations even with the 23° full width at half maximum aperture. Photon counting statistics sets the limiting resolution of 6° attempted in the present work.

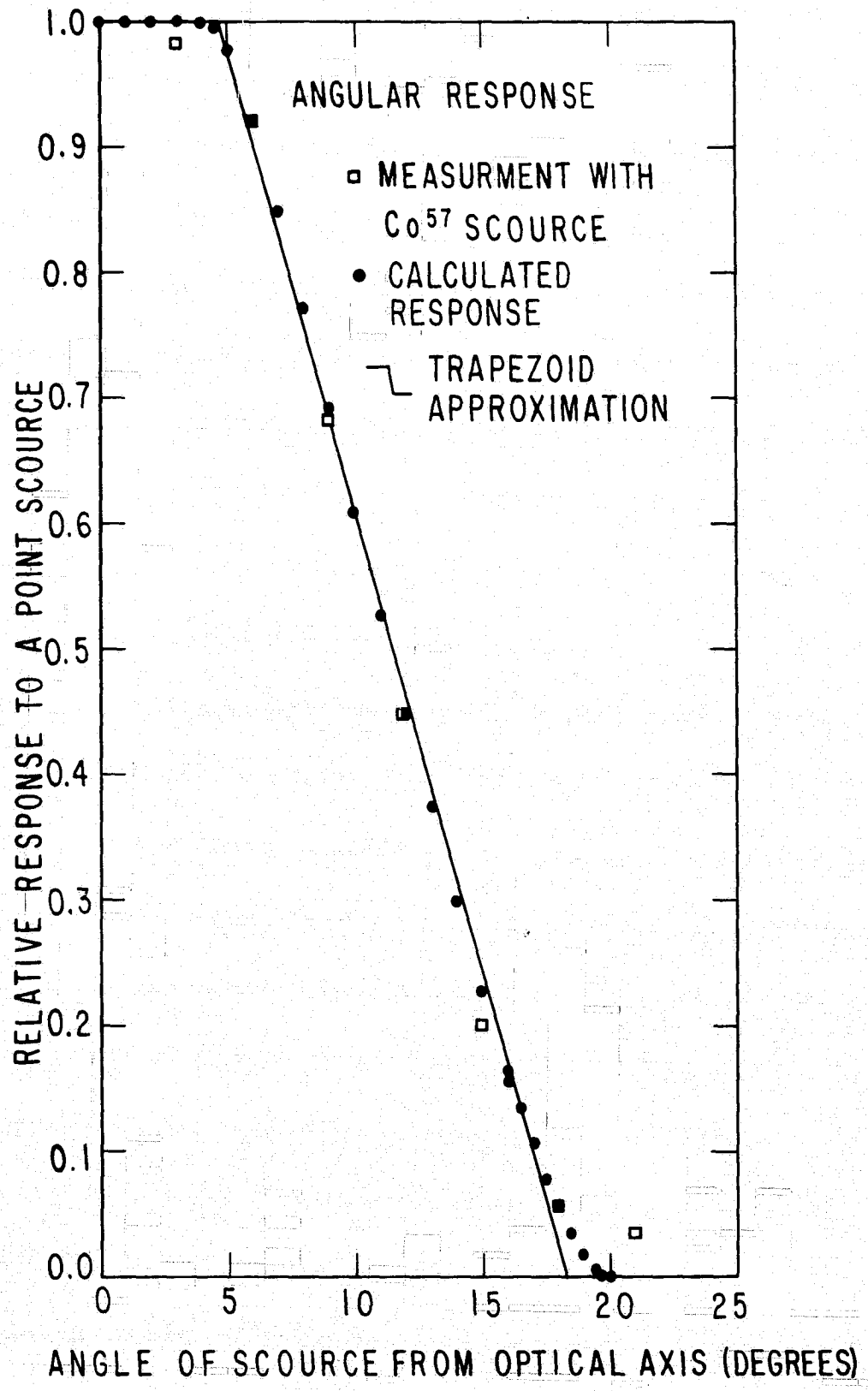

Fig. 4 Relative response to a point source vs. angle from the source to the telescope axis. The trapezoidal approximation agrees very well with both measured and calculated responses, and has the same telescope factor as calculated from the exact response function.

The telescope factor for photons entering the forward aperture

$$T_a = \iint \cos\theta\, A(\theta)\, d\Omega = 2\pi \int_0^{\pi} \cos\theta\, A(\theta)\, \sin\theta\, d\theta.$$

The integrals simplify if we first integrate over solid angle, and then over projected detector area.

$$T_a = \int_{\substack{\text{illuminated} \\ \text{NaI surface}}} \; \int_{\substack{\text{accessible} \\ \text{solid angle}}} \cos\theta \; d\Omega \, dA.$$

Neglecting terms less than $\frac{(r_1 r_2)^4}{h^6}$,

$$T_a = \pi^2 \frac{r_1^2 r_2^2}{h^2 + r_1^2 + r_2^2} = 1.35 \text{ cm}^2 \text{ ster.} \qquad (10)$$

2. Spectrometer Properties

If an X-ray of energy E_o interacts in the NaI crystal, the charge pulse presented to the analyzer will correspond to an energy E, related to E_o by the probability of complete energy loss, light collection efficiency, and statistical photomultiplication. Scintillation counters transform the energy which charged particles give to crystal excitations into optical photons. Only about 8 percent of the particle energy appears as optical energy, but the light output varies fairly linearly with total energy loss [Birks (1964)]. An X-ray thus must first give its energy to an electron, via photoelectric absorption or Compton scattering. The probability density of energy loss E' by a photon of energy E_o,

$$P_L(E', E_o) =$$

$$P_A(E_o)\,[(1-f(E_o))\cdot\delta(E'-E_o) + f(E_o)\cdot\delta(E'-(E_o-E_k))] + P_c(E', E_o),$$

with P_A the probability of photoelectric absorption of the incident photon, f the fraction of photoelectric events which result in the escape of an iodine K-shell X-ray, of mean energy E_K = 29.4 keV, and P_c the probability density that Compton scattering of the photon of energy E_o ultimately results in an energy loss E'.

$$P_A(E_o) = (\text{probability of interaction}) \times (\text{fraction of photoelectric to total interactions})$$
$$= (1 - e^{-\mu t})\,(\mu_p/\mu),$$

with t = 0.5 cm the crystal thickness, μ_p and μ the photoelectric and total linear absorption coefficients for NaI at the energy E_o. Because of the approximate Z^4 dependence of μ_p on atomic number, one need only consider the photoelectric absorption by the iodine atoms. Liden and Starfelt (1954) derived the formulas

$$f_1(E_o) = \tfrac{1}{2}\,\omega_K\,\delta_K\,\frac{\mu_p(E_o)}{\mu(E_o)}\left\{1 - \frac{\mu_K}{\mu(E_o)}\ln\left(1 + \frac{\mu(E_o)}{\mu_K}\right)\right\}$$

and

$$f_2(E_o) = \tfrac{1}{2}\,\omega_K\,\delta_K\,\exp(-\mu(E_o)t)\cdot\frac{\mu_p(E_o)}{\mu(E_o)}\cdot$$
$$\left\{\frac{\mu_K}{\mu(E_o)}\ln\left(\frac{\mu_K}{\mu_K - \mu(E_o)}\right) - 1\right\}$$

for the fraction of incident photons resulting in escape of a K-shell

X-ray from the illuminated face and rear face respectively, for a crystal of large radius and thickness compared to the mean free path $1/\mu_K = 1/\mu(E_K) \sim .04$ cm of the K-shell X-ray. They gave the values .84 for the K-fluorescence yield ω_K, and .80 for the fraction δ_K of the photoelectric processes involving a K-shell electron. Thus,

$$f(E_o) = \frac{f_1(E_o) + f_2(E_o)}{P_A(E_o)}.$$

To calculate P_c one must follow the Compton scattered photon to see if it undergoes further Compton or photoelectric interactions. I calculated P_c numerically using the Monte Carlo method of Jacobson (1968). Below about 300 keV, the Compton scattering primarily adds counts to the photo and K escape-peaks, and to the "plateau" region corresponding to energies below the maximum possible energy loss E_c in a single Compton interaction. I thus approximate

$$P_c(E', E_o) = a_1(E_o)\ \delta(E'-E_o) + a_2(E_o)\ \delta(E'-(E_o-E_K)) + a_3(E_o)\ H(E_c-E'),$$

where $$H(x) = \begin{cases} 0 & x < 0 \\ 1 & x \geq 0 \end{cases},$$

and the Compton edge

$$E_c(E_o) = \frac{E_o}{1 + \frac{511}{2E_o}} \quad [\text{keV}].$$

Figure 5 shows the calculated coefficients a_1, a_2, and a_3 as functions of incident photon energy.

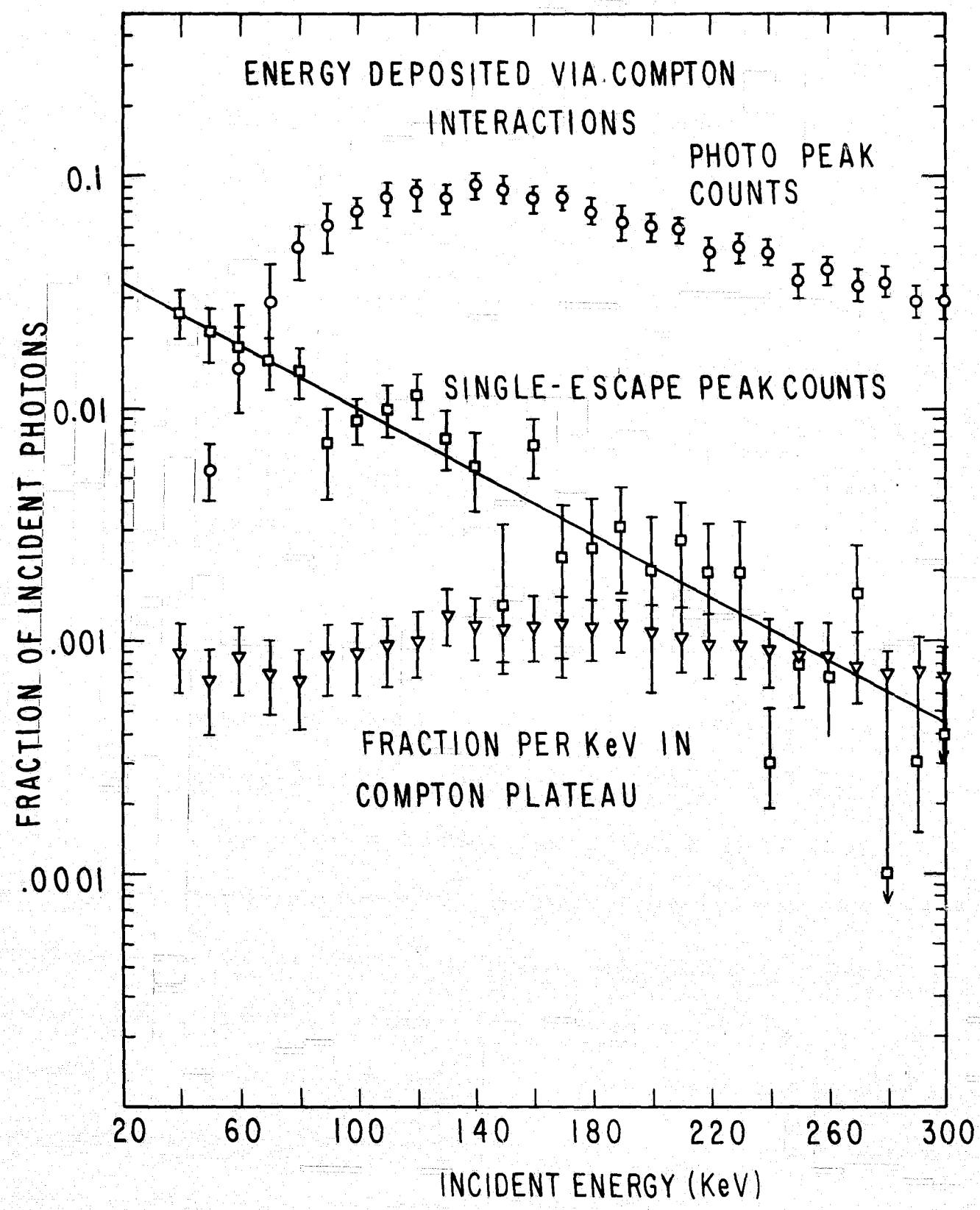

Fig. 5 These coefficients give the fraction of all incident photons, which initially Compton scatter with a final energy loss equal to the incident energy (a_1), incident energy minus 29.4 keV (a_2), or in a 1 keV band below the Compton edge (a_3). The programs use the straight line approximation to a_2.

The optical photons eject a few electrons from the RCA type 4461 photomultiplier tube cathode, and these electrons undergo 10 stage multiplication, by a factor of 4 or 5 at each stage. Fluctuations in the number of photons collected at the photocathode and in the electron multiplication at the first few dynodes result in a distribution of charge pulse heights for a fixed energy loss E'. For a charge pulse resulting from the sum of an indefinitely large number N of independent interactions, one expects the probability distribution of equivalent pulse height energy to approach a normal distribution with mean E' and variance $\sigma^2 \propto N \propto E'$. Generally, other effects degrade the resolution. Pulse height distributions measured at BBRC with a 400 channel analyzer showed several γ-ray sources with normal shaped peaks about their mean energies. Figure 6 shows the standard deviations, obtained from the pulse height graphs by $\sigma = .424 \cdot$(full width of peak at half maximum). From Figure 6 I use $\sigma(E) = 0.65E^{0.67}$.

The resolution probability density that an energy loss E' results in a charge pulse equivalent to E,

$$P_R(E, E') = \frac{1}{\sqrt{2\pi}\,\sigma(E')}\, e^{-\frac{(E-E')^2}{2\,\sigma^2(E')}}.$$

The independence of the energy loss processes and the resolution effects implies that the probability density for measuring an incident photon of energy E_o to have energy E,

$$P(E, E_o) = \int_0^{E_o} P_R(E, E')\, P_L(E', E_o)\, dE'. \qquad (11)$$

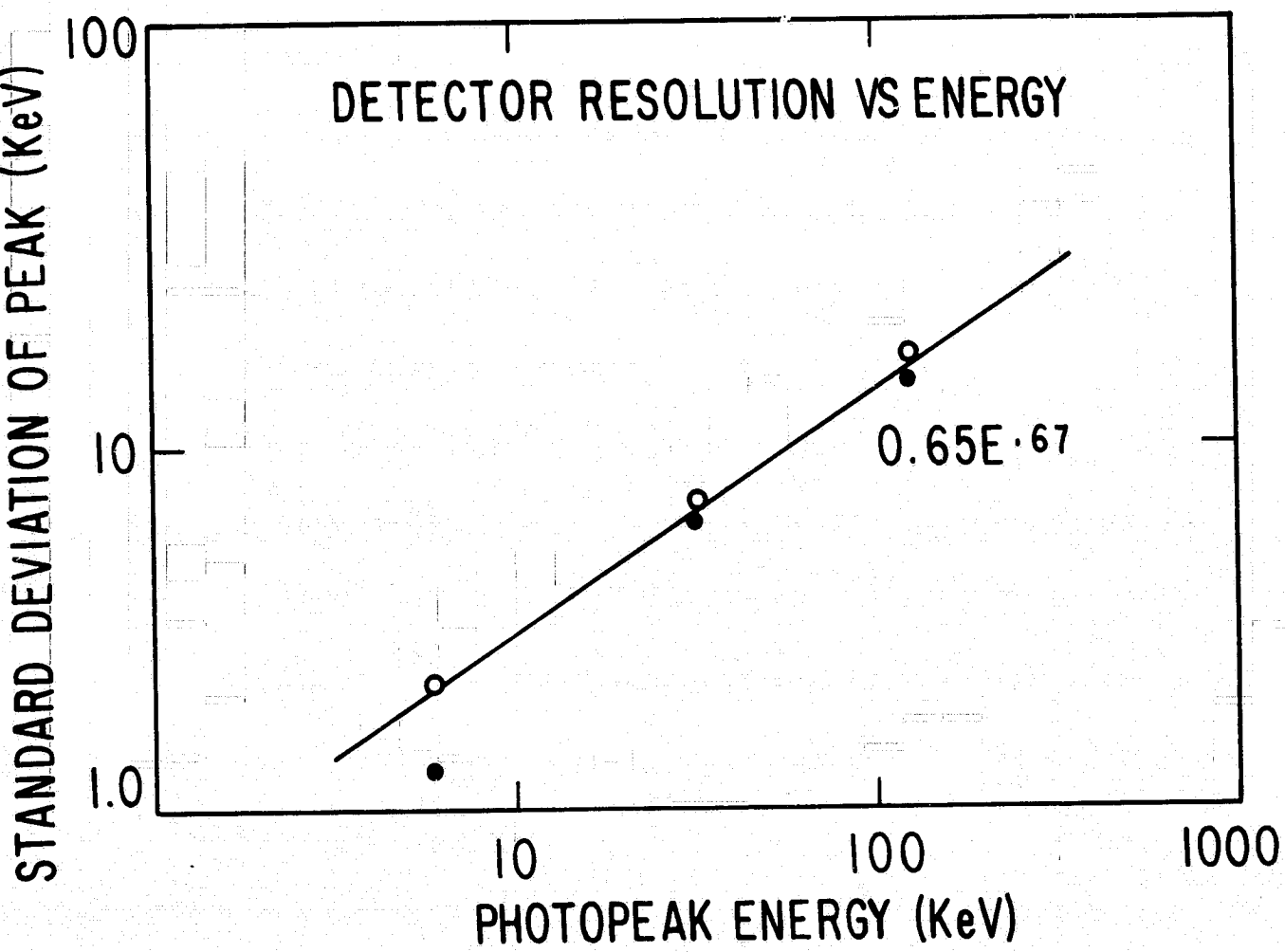

Fig. 6 BBRC measured normal shaped peaks for the 5.9 keV Fe^{55} X-ray, the 32 keV Ba^{133} X-ray, and the 123 keV Co^{57} X-ray. These measurements of the flight instrument occurred on June 29, 1966, (open circles) and June 30, 1966, (solid circles).

Figure 7 shows the probability

$$P_k(E_o) = \int_{E_{kl}}^{E_{ku}} P(E, E_o)\, dE \qquad (12)$$

that a photon of energy E_o entering the detector results in a count in channel k which has energy limits E_{kl} to E_{ku}. Figure 8 compares the total interaction probability to the total <u>detection</u> probability, as a function of incident X-ray energy. Table 2 gives the ratios

$$\frac{R_k(n)}{J} = \int_o^\infty P_k(E_o)\, E_o^{-n}\, dE_o,$$

with R_k the expected count rate in channel k caused by the number spectrum $\frac{dN}{dE}(E) = JE^{-n}$ photons $(\text{keV sec})^{-1}$, for several values of n. The numerical integrations used a 1 percent accuracy criterion in the calculation of R_k.

B. The OSO-III Satellite

Figure 9 shows the OSO-III satellite. It consists of a nine-compartment, 22-inch radius wheel from which three 24-inch arms extend, and a 22-inch radius sail structure ("Experimenter's Manual S-57 Orbiting Solar Observatory," BBRC TM 63-1). The UCSD X-ray telescope occupies half of a wheel compartment. The wheel section spins at about 30 RPM, to provide a stable platform for the sail. During the sunlit portion of the orbit, "orbit day," a motor drives the sail against the wheel so that the sail locks on the solar direction. Ground commanded firing of gas from the extended arms or energizing

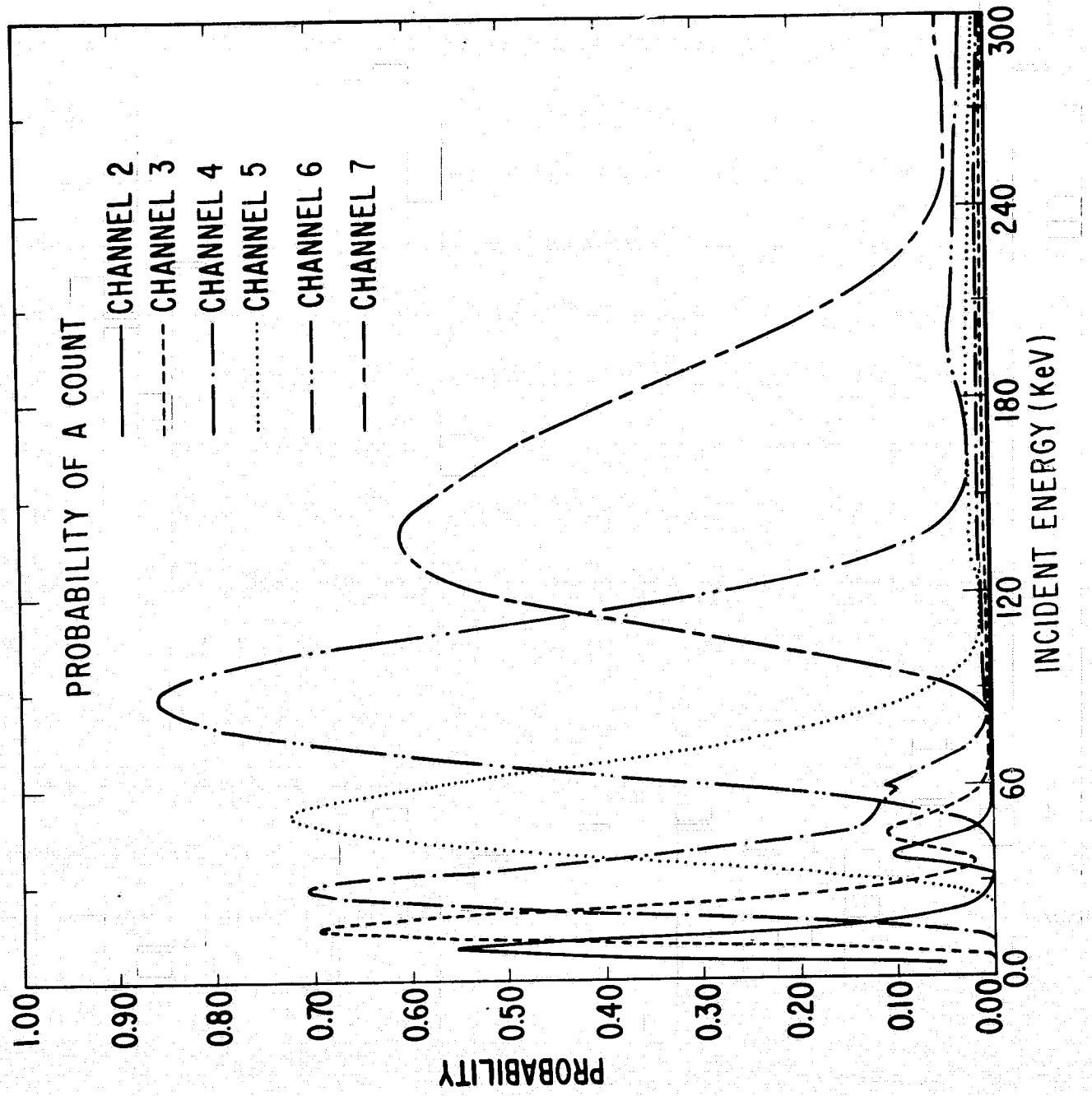

Fig. 7 Probability of actually recording a count in a given channel, as a function of incident photon energy.

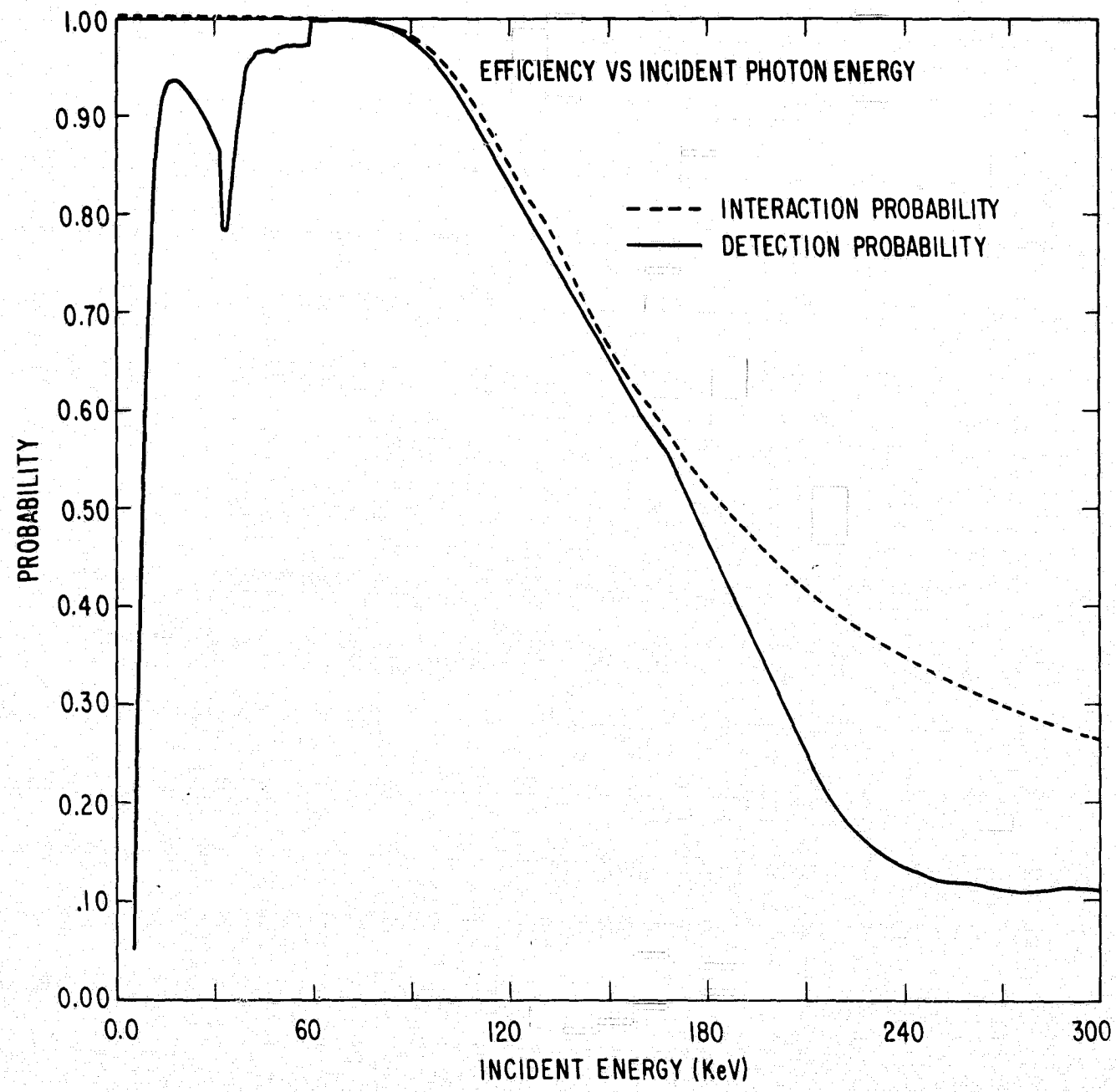

Fig. 8 The dashed line gives the probability for the occurrence of any interaction in the detector. The solid line gives the probability per incident photon that the analyzer will receive a charge pulse corresponding to an equivalent energy between 7.7 and 210 keV.

Table 2

Response to Power Law Spectra

Channel Number	Ratio of Count Rate to J if $\frac{dN}{dE} = JE^{-n}$				
	n = 1.0	n = 1.5	n = 2.0	n = 2.5	n = 3.0
2	.456	.141	.0455	.0151	5.16×10^{-3}
3	.570	.138	.0347	8.98×10^{-3}	2.39×10^{-3}
4	.521	.0952	.0180	3.50×10^{-3}	0.693×10^{-3}
5	.495	.0685	9.72×10^{-3}	1.41×10^{-3}	0.208×10^{-3}
6	.518	.0554	6.03×10^{-3}	0.668×10^{-3}	7.49×10^{-5}
7	.353	.0298	2.53×10^{-3}	0.214×10^{-3}	1.85×10^{-5}

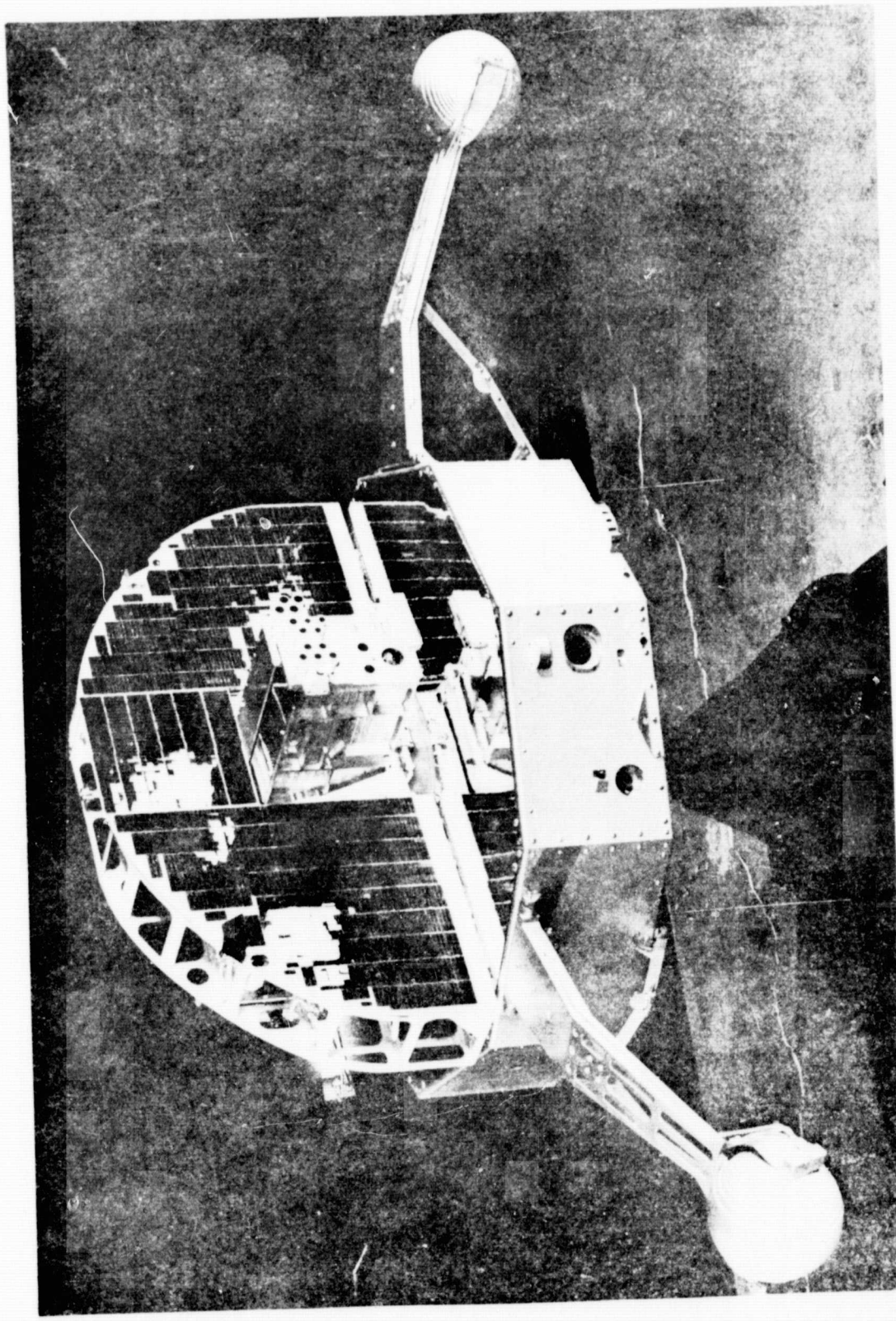

Fig. 9 Photograph of an OSO satellite. The wheel drum and arms revolve constantly; the semicircular "sail" remains pointed at the sun during orbit day. The UCSD X-ray telescope occupies half of a wheel compartment.

of a magnetic torque coil keeps the wheel plane within 3° of the sun. Thus as the earth moves about the sun, the spin axis position changes an average of 1° per day, and in six months the great circle cut by the rotating wheel sweeps out almost the entire sky. The telescope misses about 10° around the celestial poles since the spin axis oscillated between -15° and -35° declination, instead of precessing along a great circle.

A Thor-Delta rocket launched OSO-III on March 8, 1967, into a nearly circular orbit at 550 km altitude and 33° inclination. Thus, it has an orbital period of 95.6 minutes. One of two on-board tape recorders stored all telemetry for 90 minutes, and read out the PCM to FM in five minutes upon command from a NASA Minitrack station at Ft. Meyers, Florida, or on the west coast of South America. In practice, this gave us about 90 percent total data retrieval from launch until the second tape recorder failed on June 28, 1968.

OSO-III has a 400-bits-per-second rate; the 0.64-second main frame contains 32 eight-bit words. The UCSD experiment fills one word each main frame. Three other main frame words contain subcommutated information of interest. The "wheel analogue subcommutator" contains a measurement of the spacecraft line voltage, the high voltage supply to the NaI photomultiplier tube, a rough (1 percent accuracy) spin rate, and various spacecraft temperatures. The "sail analogue subcommutator" contains a pitch angle measurement. These analogue subcommutators have a 48 main frame (30.72 seconds) period. The "digital sub-multiplexed" (DSM) word contains data needed for the aspect solution, and has a 40 main frame (25.6 seconds) period. Appendix A

contains a description of the orbit and aspect calculations.

OSO-III performance far exceeded the lifetime design of six months. Failure of the second tape recorder on June 28, 1968, ended complete data retrieval after almost 16 months. Real time data after that date indicate that the satellite systems and UCSD experiment still functioned properly. Spacecraft temperatures remained stable between 15° and 17°C; the spacecraft line voltage and the detector phototube high voltage remained stable within the $\frac{1}{2}$ percent digital readout error. The spacecraft magnetometer and sun sensor systems usually gave sufficiently good data to calculate the aspect with 1° to 3° confidence.

C. Data Reduction

1. Telemetered Data

Table 3 shows the UCSD subcommutation scheme. The experiment has two basic modes: the "sun count" and the "sector direction" measurements. During orbit day a photocell generates an enable pulse 22° before the telescope axis points at the sun. A clock pulse ends the enable gate between .225 and .262 seconds later, or about 30° past the sun. During that interval counts accumulate in one of the eight energy channels. Readout occurs every three main frames, 1.92 seconds, and fills two main frame words. The third word contains a sector direction reading in one of the six differential energy channels. Only one energy channel can ever receive counts at any given time; the sun energy subcommutator advances every 1.92 seconds, and the sector energy every 122.88 seconds. The fact that 1.92 seconds exceeds the spin period,

Table 3

X-ray Telescope Data Subcommutation

Data Unit	Period (sec)	Number of Spacecraft Main Frames	Data Contents
Main frame word	0.64	1	1 synch bit, 1 energy identifier bit, 6 data bits
Sun energy channel	1.92	3	Accumulated sun counts in one energy channel; one sector direction count
UCSD synch pattern	3.84	6	(Minimum unit of usable data)
Sun energy frame	15.36	24	1 complete 8-channel sun gate spectrum
Sector energy channel	122.88	192	8 complete sun gate spectra; 60 sector direction counts in one energy channel; total number of counts arriving in that energy regardless of direction; one anticoincidence shield rate
Complete experiment cycle	737.28	1152	One complete 6-channel direction count accumulation; 3 upper and 3 lower level anticoincidence rates

of about 1.6 seconds, complicates the analysis since the telescope may pass the sun (or any point on the scan circle) either once or twice, and even if only once the large half angle can result in any fractional exposure between 1.0 and 2.0 (cm^2 sec). One bit in each of six successive words forms a synch pattern, and one bit in each of three successive words alternately identifies the sun or the sector energy channel. The logic which detects orbit night enables the sun gate continuously (between readouts) so that it accumulates counts from the entire scan circle.

Every two minutes the upper or lower level anticoincidence discriminator rate and the total counts received during the previous 180 main frames (115.2 seconds) preempt four sector direction words in the telemetry. The sector direction measurements provide the data for studying the spatial distribution of X-rays. We thus have a telemetry capacity for 42,000 X-ray counts per day; low count rates in the upper channels reduce this to about 30,000 received, and considering only counts from the sky with the satellite outside trapped radiation areas results in about 7600 total counts per day in all the differential channels.

The Goddard Space Flight Center provides final data tapes whose files each contain all the UCSD telemetry words in one satellite pass, together with the analogue and DSM words of interest. The first data reduction computer program reads in these words, decodes sun and sector counts into decimal numbers, groups them into two-minute sector energy channels, calculates the time of telemetry words, and calculates relevant orbit and aspect data for the pass.

Even without a parity bit, loss of synch pattern or sun or sector identifications which do not agree with the expected commutator sequence indicate areas of poor data. Such areas often consist of several consecutive passes of the satellite over one particular tracking station, or occur with high frequency in a data tape made by GSFC during one particular analogue to digital decommutation run. Other areas of data have synch errors at a rate of less than one bit error in 10,000 for several consecutive days.

Figures 10 and 11 show some of the orbit and aspect data available after the first data reduction step. In geographic coordinates, the subsatellite point traces out an approximate sine wave of 33° latitude amplitude, which precesses about 25° westward in longitude each orbit. Figure 10 shows corresponding traces in B-L space. Pass 277 illustrates a typical, complete orbit. About eight successive orbits every day carry OSO-III into the South Atlantic anomaly region of trapped radiation. Pass 282 shows such inner radiation belt penetration, which may last up to 10 minutes. Figure 11 shows scan circles traced by the wheel plane on the celestial sphere. The shaded area around the 12 May scan represents the detector half response; note its width compared to the separation of discrete X-ray sources. The scan changes a negligible amount in one day, and approximately repeats after six months. At this stage of analysis I divide the scan circle into 60 bins or "sectors" for convenience; later I consider the fact that the information provided by the sampling scheme varies from 42 to 49 sectors.

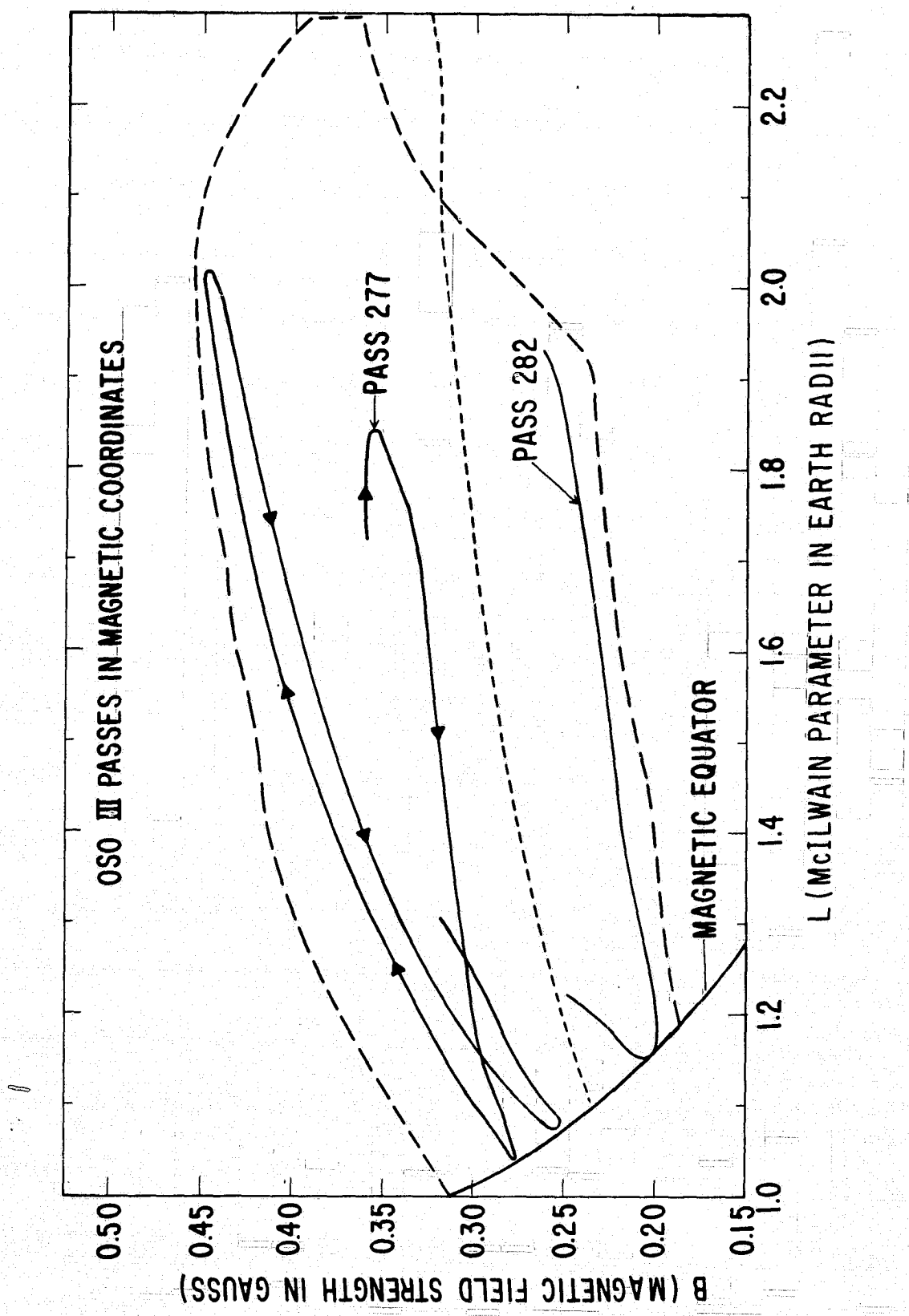

Fig. 10 The heavy dashed line contains the region of B-L space swept out by OSO-III. The light dashed line represents the upper boundary to the "trapped electron" region of NASA map AE2 [Vette, et al. (1966)].

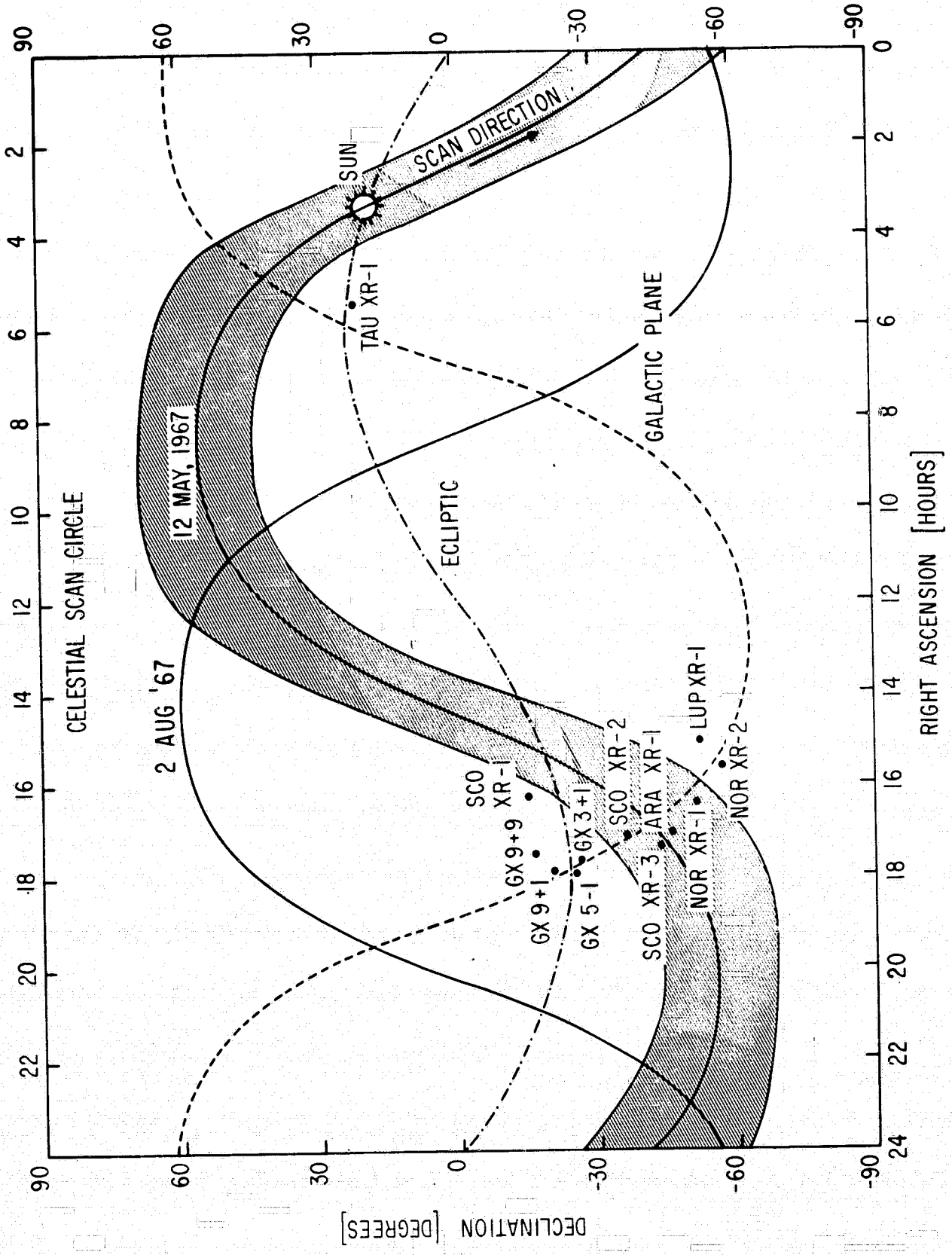

Fig. 11 The scan circle precesses approximately 1° per day in right ascension. All the discrete sources shown near the galactic center contribute to the count rate for the May scan. The earth blocks about half the scan circle at any time.

Figures 12, 14, and 15 show physical quantities derived from the first stage of analysis. Figure 12 shows shield ULD and LLD rates versus time, along with the L parameter calculated for the satellite position at the same time. The shield rate curves generally follow the L curve, reflecting the latitude variation of cosmic rays. Least squares fits of shield rates to AL^x give $x = 1.95 \pm .08$ for the ULD and $x = .8 \pm .2$ for the LLD. The coefficients A, and the exponent for the lower level rate, decrease gradually over one year, as shown in Figure 13, indicating a gain deterioration. This loss of shield effectiveness causes a corresponding increase in the NaI background rate. Cosmic ray vertical cutoff rigidities depend on $15.96\ L^{-2}$ [Smart and Shea (1967)]. Use of the Freier and Waddington (1968) integral proton spectrum $J_p(>R) = 4500R^{-1.3}$ for rigidity R>3 GV, predicts a rate $22L^{2.9}$ counts per second for the ULD. The remainder of the shield count rate must result from locally produced and from earth albedo gamma rays.

The heavy line at the bottom of the graphs indicates passage through the South Atlantic trapped particle anomaly (defined as a rectangle $-90^\circ \leq$ east longitude $\leq +50^\circ$, latitude $< 0^\circ$ for convenience in plotting). Figure 12 shows saturation counting rates due to trapped particles, and the decay with 25-minute half life of I^{128} [Peterson (1965)]. Typical activation corresponds to .4 disintegrations per (gm. sec), with values up to 2.0 obtained on some passes.

Figures 14 and 15 show rates derived from the total counts received during a 115.2 second energy channel. Variations in these rates reflect the many sources of the counts in our detector, as labeled in the figure. Note the day-night modulation in channel 2 due

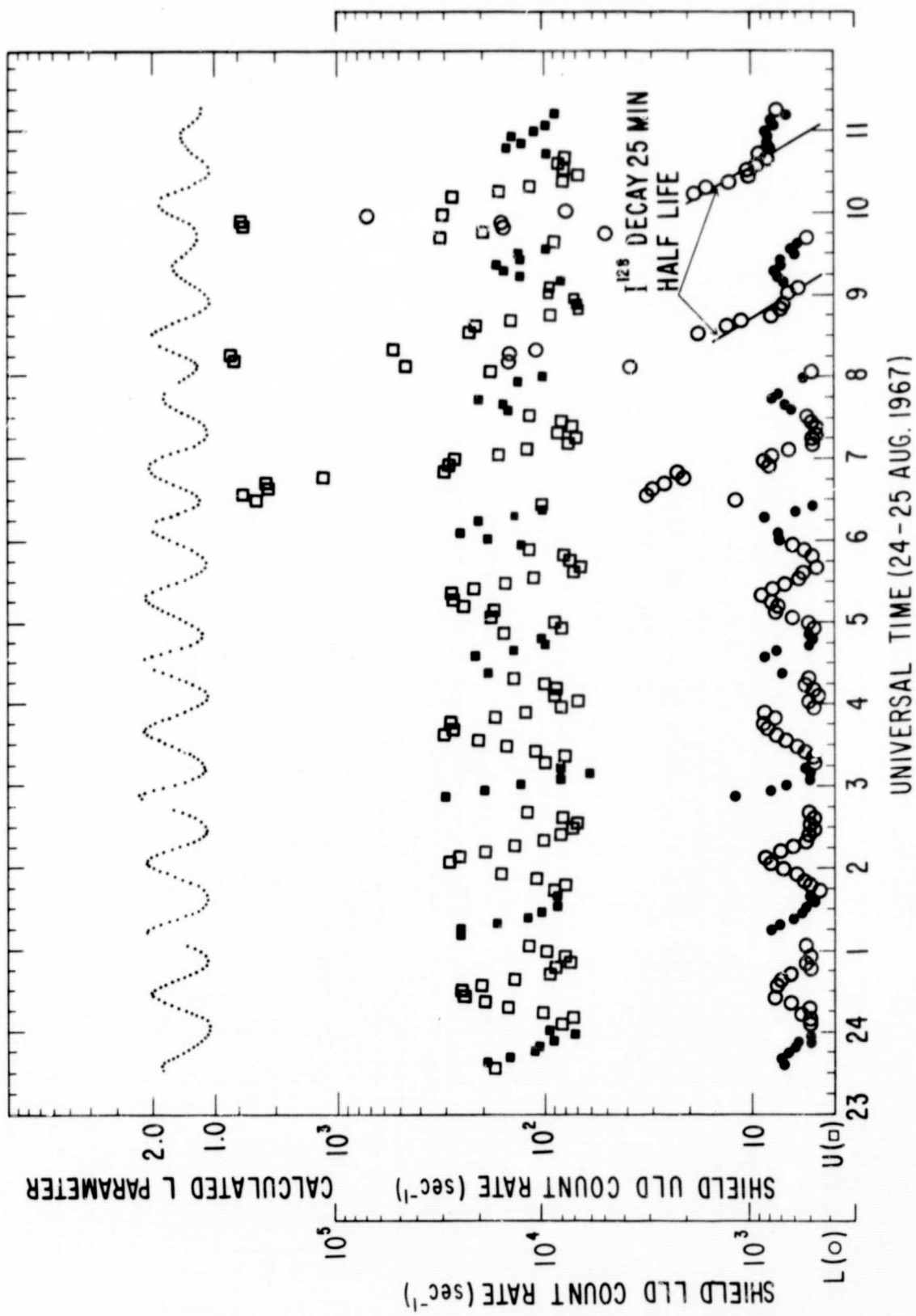

Fig. 12 The shield rates generally follow the L value. Saturation occurs upon penetrating the South Atlantic radiation belt around 7, 8:30, and 10 UT; followed by the decay of the induced radioactivity in iodine.

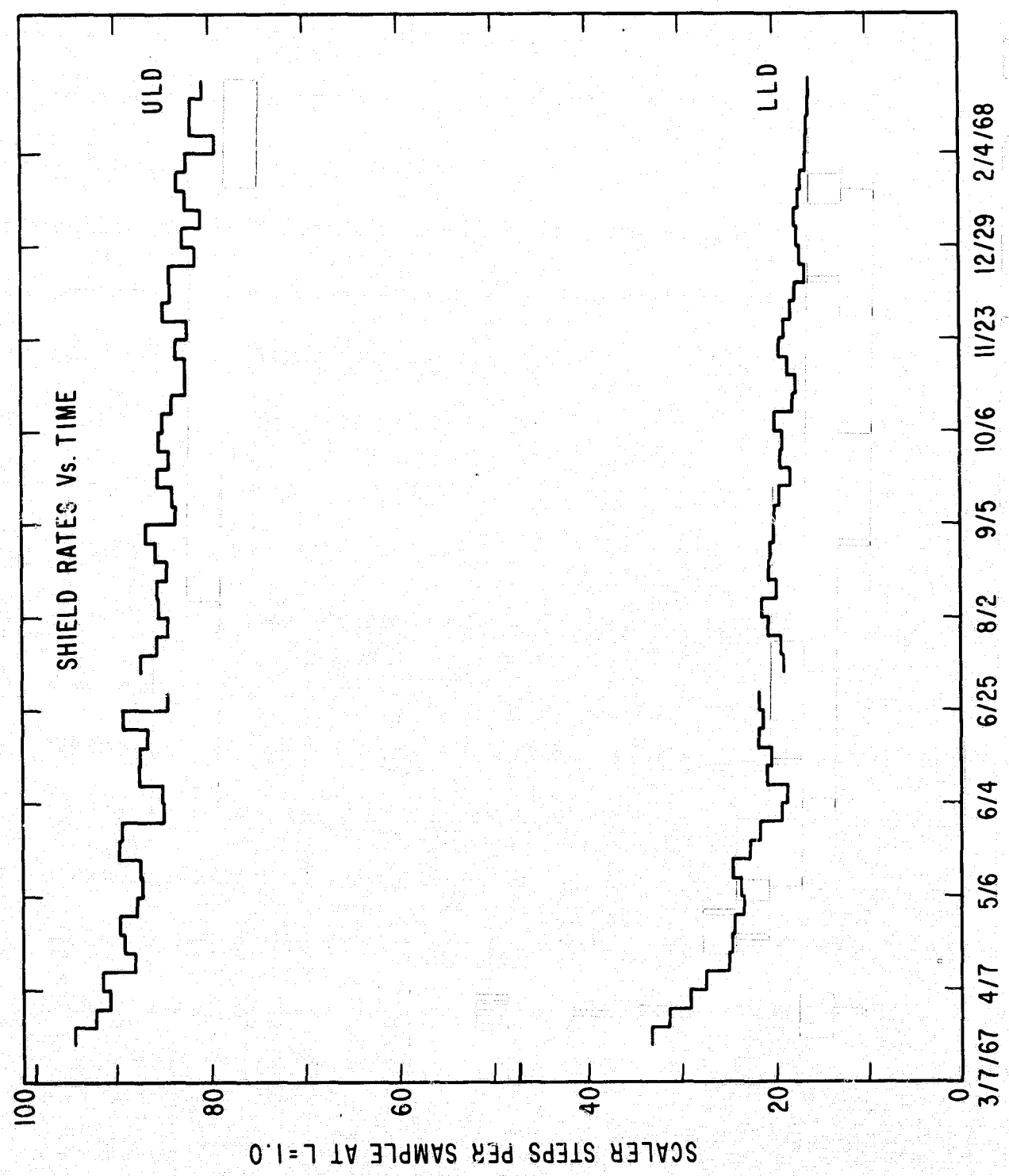

Fig. 13 Least squares fit shield rate at L=1.0. One LLD step equals 25 counts per second, and one ULD step equals 0.78 counts per second.

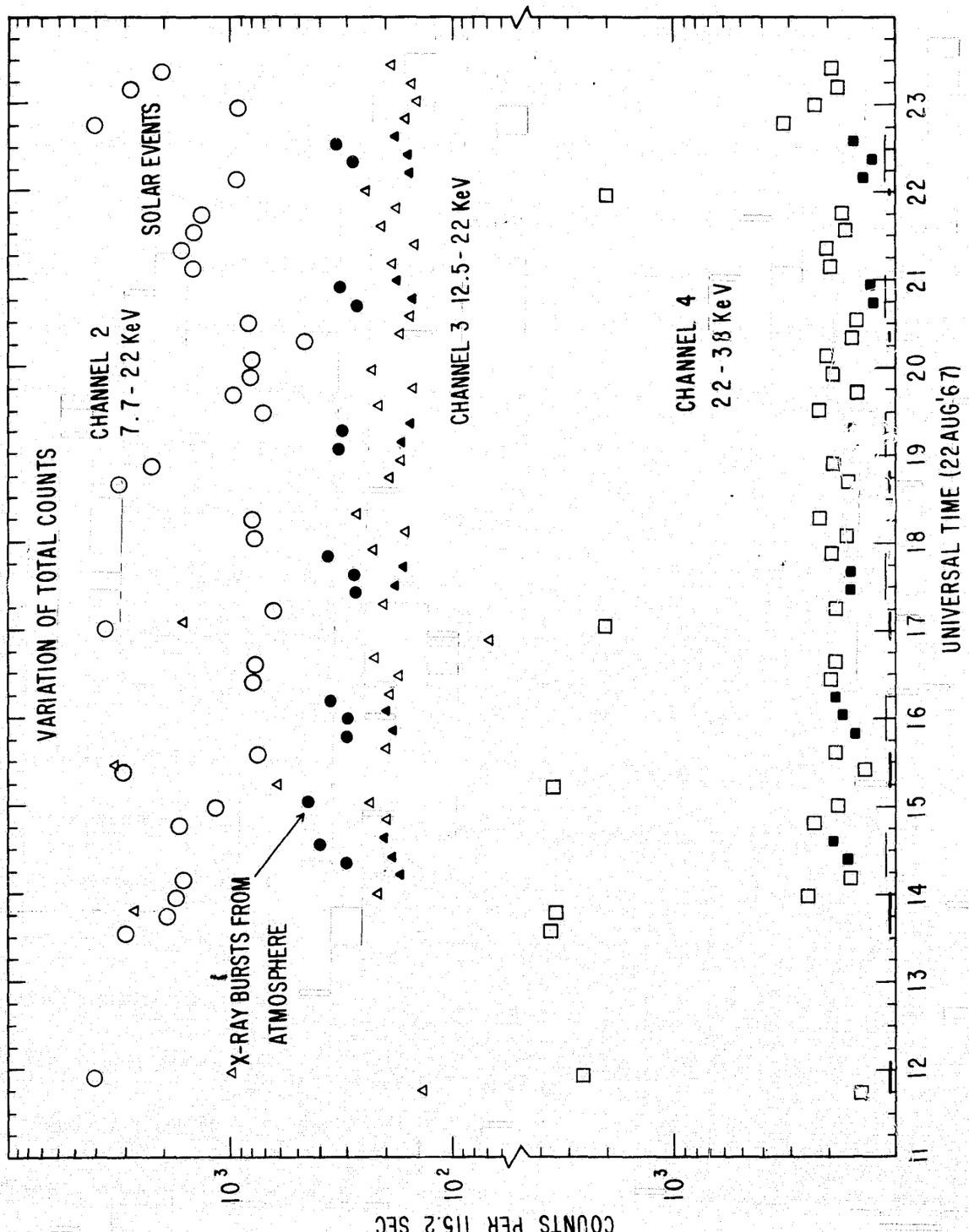

Fig. 14 Total counts arriving in 115 seconds from all directions, for the three lowest energy channels. Solid symbols represent night data, open symbols represent day data. Most of the fluctuations exceed the statistics, with some of the causes labeled.

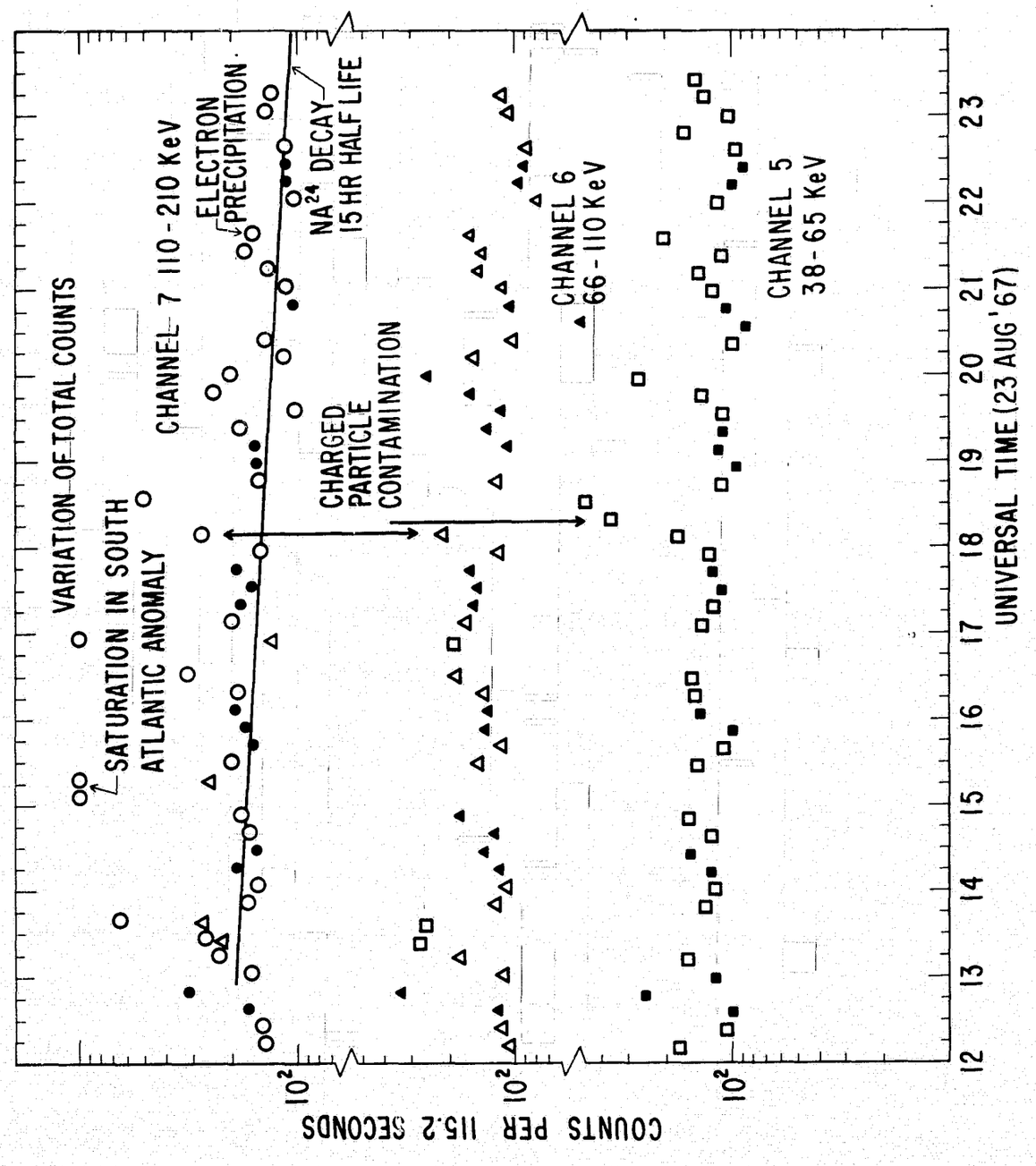

Fig. 15 Total counts for the highest three channels, as in Figure 14. I use the directional count rates vs. angle to magnetic field line to identify charged particle events.

to solar X-rays, sporadic events due to electron precipitation at the satellite or in the atmosphere, and saturation when in the South Atlantic trapped radiation. The total count rates afford the greatest statistical sensitivity for detection of such anomalous events, although one usually needs directional intensities or other evidence to reveal the nature of each event.

The sun position corresponds to sector 3.7 (Appendix B). Because of the variability of solar X-rays, further analysis does not use channel 2 sky counts from sectors 1 to 9 or sector 60. Each higher energy channel n uses counts in these sectors only if the sun gate gave no statistically significant flux in energy channel n-1. I consider this a very safe criterion because we observe that solar X-ray events have thermal type spectra [Hudson, et al. (1969b)], much steeper than the diffuse component. When a sun event exceeds about 3000 counts $(cm^2\ sec)^{-1}$ above 7.7 keV, saturation and pile-up effects may begin to disturb the amplifier levels. The analysis program rejects the data from such times.

2. True Count Rate

The second stage of data analysis assigns an arrival sector for every count, and calculates the live time for the sectors. The 122.88 second "sector energy channel" during which up to 60 counts arrive in a fixed energy channel forms the basic unit for analysis. Live sampling starts at a defined telemetry word relative to the UCSD synch pattern. The aspect solution connects this time to a point on the celestial sphere (Appendix A). A scaler then counts the number of 37.5 millisecond intervals until the arrival of a count, whereupon the

sector direction mode becomes dead until telemetering of the scaler reading. The logic telemeters a zero if no count arrives during the entire sample period, which alternately lasts 1.9 and 1.26 seconds. The scaler number gives the arrival time, then knowing the spin rate gives a wheel angle for the arrival direction of the count. A 37.5 ms clock advances the scaler, but the sun or magnetometer pulse resets it to 1 each revolution. No integral multiple of .0375 second equals the spin period, so a scaler reading of 1 represents an imprecise exposure time between 0 and 37.5 ms. This causes a 37.5 ms slip uncertainty in the position of all sector readings.

Knowing the approximate average true rate during one sector energy channel from the total counts, I derive the normalized probability density functions for the exact arrival direction of the X-ray given the scaler reading (Appendix B). I then smear the count among the (three or four possible) sectors in proportion to the density function integrated over the sector. The computer reduction program randomly samples the distribution function to assign an arrival time to the nearest 2.5 ms within the 37.5 ms scaler step for the purpose of assigning live time to the sector bins. The program corrects for ULD shield dead time by a factor $(1 - .0002\ A\ L^2)^{-1}$, where A equals the least squares fit count rate of the ULD at L = 1, and L equals the average value during the two-minute energy channel.

I classify each sector bin as "sky", "earth", or "horizon" during each two-minute sector energy channel. "Sky" (or "earth") means that the X-ray telescope pointed at least 20° outside (or inside) the actual edge of the earth for this entire sampling time. "Horizon"

sectors thus contain an irregular mixture of counts from the sky, the earth below, and the layer of atmosphere which forms the actual horizon between them.

Figure 16 shows true count rates obtained in the lowest energy channel. Counts between 288° and 90° accumulated during times with the earth in the position shown, thus only during orbit night. In other directions accumulation of counts occurred when exposed to the sky. The areas marked by A indicate sky count rates used in studying the diffuse component. The area B contains earth albedo X-rays. The area around 300° shows the transition from the diffuse to the terrestrial X-rays at one horizon. At the other horizon, around 66°, precipitating particles caused an auroral type X-ray event on 19 April, 1967, which produced a peak count rate over 100 sec^{-1}, and which thus raised the average count rate for this four-day stretch of data. The discrete source SCO XR-3 appeared near the scan plane at 150°; the resulting peak in the count rate also contains counts from SCO XR-1.

3. Background Corrections

To decide what fraction of the true count rate represents cosmic X-rays one can only try to imagine every possible background source and estimate its magnitude. The telescope's 0.15 ster aperture divides the sky into about 100 patches, so 365 days of data would give a 1.5 percent counting statistics limitation for each patch in each energy channel. This percentage becomes the target for determining background. I care above all about determining any anisotropies in the background as accurately as possible. I consider the following possible sources of background: terrestrial X-rays, cosmic ray effects,

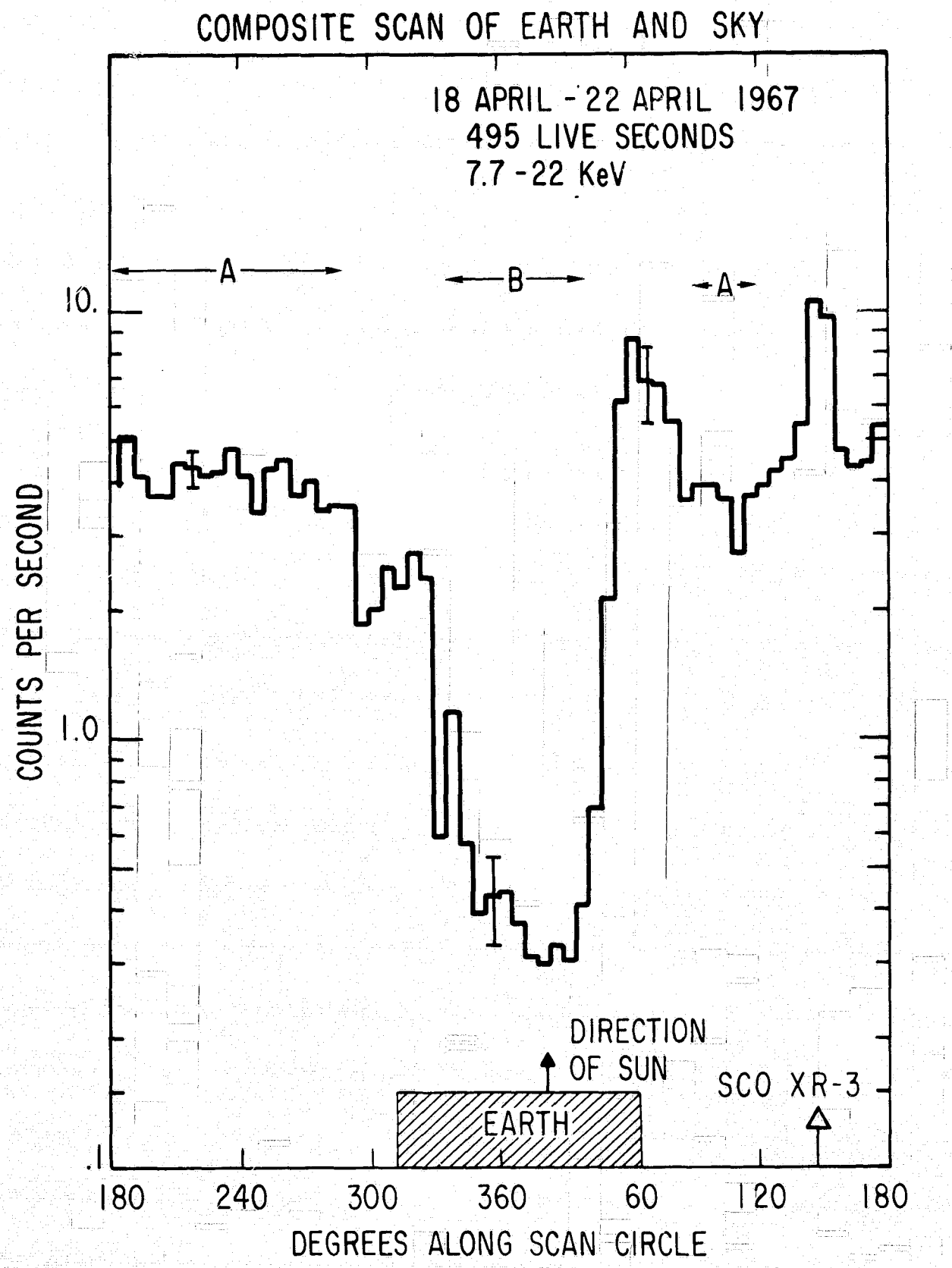

Fig. 16 Count rates along a fixed scan circle, corrected for dead time, but with no background corrections. The data accumulated when the earth blocked the sun, as shown. The programs select only areas such as marked A as free from earth and discrete sources, for diffuse component analysis.

induced radioactivity, phototube noise, and magnetospheric particle effects.

Charged particles precipitating in the earth's atmosphere cause X-ray events which can produce count rates in our telescope 100 to 1000 times the diffuse component count rates [Schwartz, et al. (1968b)]. The analysis program rejects sector energy channels with a horizon count rate greater than 10 times the sky count rate, and redefines "sky" to 40° away from the solid earth for the purpose of diffuse component analysis. The 40° ensures that even with the 37.5 millisecond sector slip, the atmosphere falls completely outside the telescope response pattern (less than 1 percent response).

Cosmic ray protons striking an OSO satellite produce secondary gamma rays similar in spectrum and intensity between .1 and 5 Mev to the secondary gamma rays they produce in the atmosphere [Peterson (1968)]. Photons of several hundred keV have reasonable (of the order of a few percent) chances of penetrating the shield, Compton scattering in the NaI with a total energy loss between 7.7 and 210 keV, and then escaping the shield without depositing enough energy to trigger the shield anticoincidence. Such a "Compton plateau" background component should have a very flat differential number spectrum.

A balloon-borne experiment verified this spectral shape and measured its intensity at 12.6 gm/cm^2 in the atmosphere. Jacobson and Peterson (in preparation) performed that experiment on the OSO-III prototype detector by blocking the aperture with a 4" x 2" NaI crystal placed in active anticoincidence along with the regular CsI active shield. Table 4 lists the measured count rates in the actual OSO-III

Table 4

Cosmic Ray Induced Background

Channel	Measured Rate at 12.6gm/cm^2 (counts per second) [Peterson and Jacobson (in preparation)]	Predicted Rate on OSO-III at L = 1	Upper Limit from OSO-III Measurements	Correction Coefficient Used (Counts per second at L = 1)
2		0.005	0.10	0.003
3	0.036	0.011	0.15	0.009
4	0.06	0.018	0.10	0.015
5	0.10	0.029	0.12	0.023
6	0.18	0.053	0.13	0.043
7	0.40	0.12	0.15	0.095

channels, (assuming a flat extrapolation of the background spectrum below the 15 keV lower energy threshold of the balloon flight). To predict a background in orbit at L = 1 I divide by 2, the ratio of atmospheric gamma rays at 12.6 gm/cm^2 [Peterson and Schwartz (in preparation)] to the lower level shield rate at L = 1 soon after launch, and assuming the same production dependence on L as observed in the lower level shield rate, divide by 1.7, the approximate L value of the balloon measurements.

All cosmic ray effects must increase with the L value. Figure 17 shows channel 7 sun gate rates plotted against the mean L value of the sample period. (No solar X-rays appeared in the lower channels at these times.) From the Ranger III measurements [Metzger, et al. (1964)] diffuse gamma rays do not contribute more than 0.1 counts per second. Radioactivity and trapped particles contribute strongly and sporadically to these rates, and allow the absence of any L dependence. From examination of many such channel 7 graphs I conclude that 0.2 counts per second limits the excess at L = 2.3 over that at L = 1. Similar plots for the other energy channels result in the upper limit column of Table 4.

I estimate a correction from least squares fits of the total counts rate (after making the radioactivity correction described below) to

$$A_k L + B_k,$$

for each channel k (Figure 18). This usually gave an unacceptable fit (A or B negative, or much larger than previous diffuse X-ray measurements); I used each acceptable value as a normalization of the spectrum

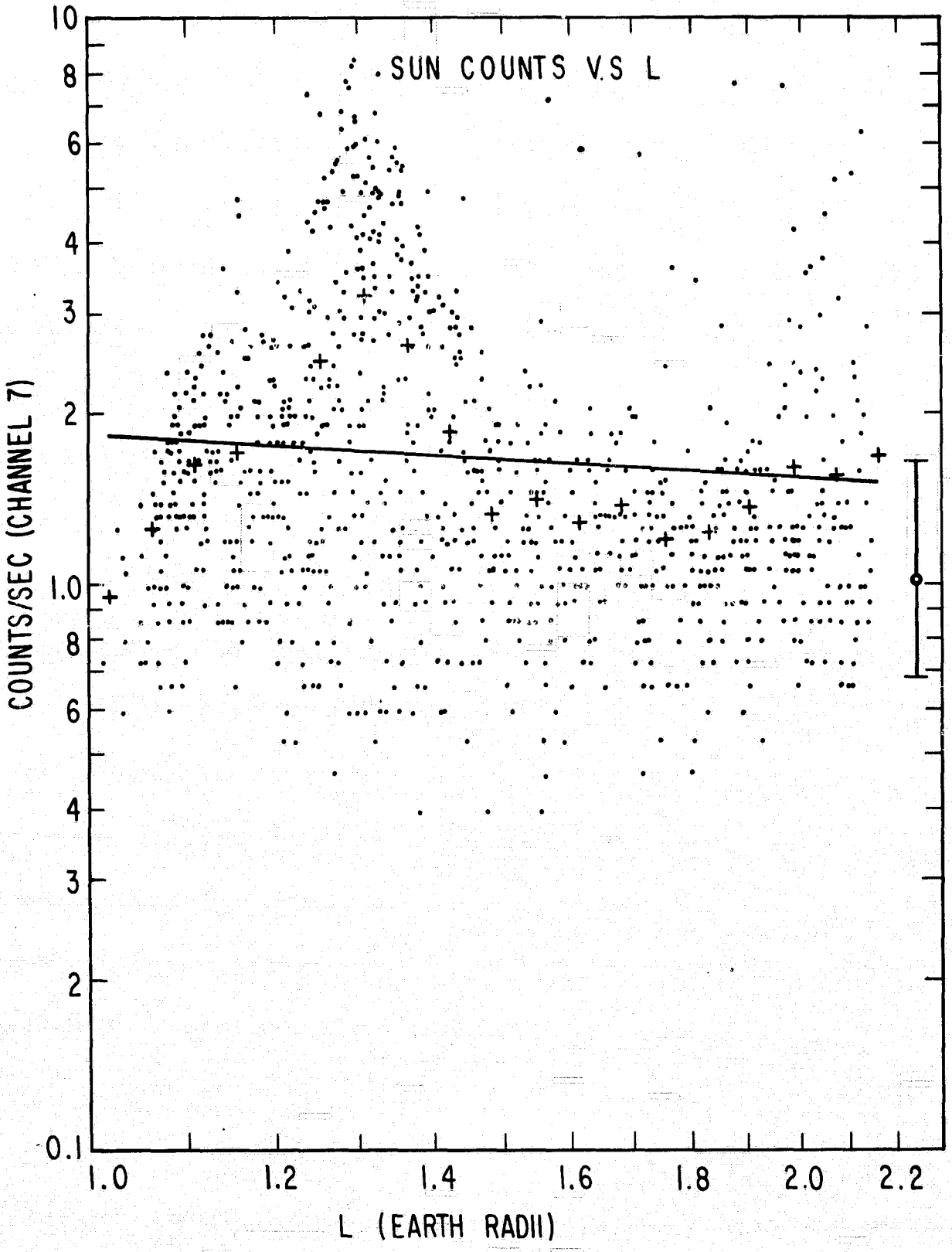

Fig. 17 Dots represent channel 7 sun gate rates at an L value averaged over two minutes. Plus signs represent the average rate in the given range of L, the straight line results from a least squares fit. No count rate increase with L value appears. Particle contamination causes the bulge around L=1.3.

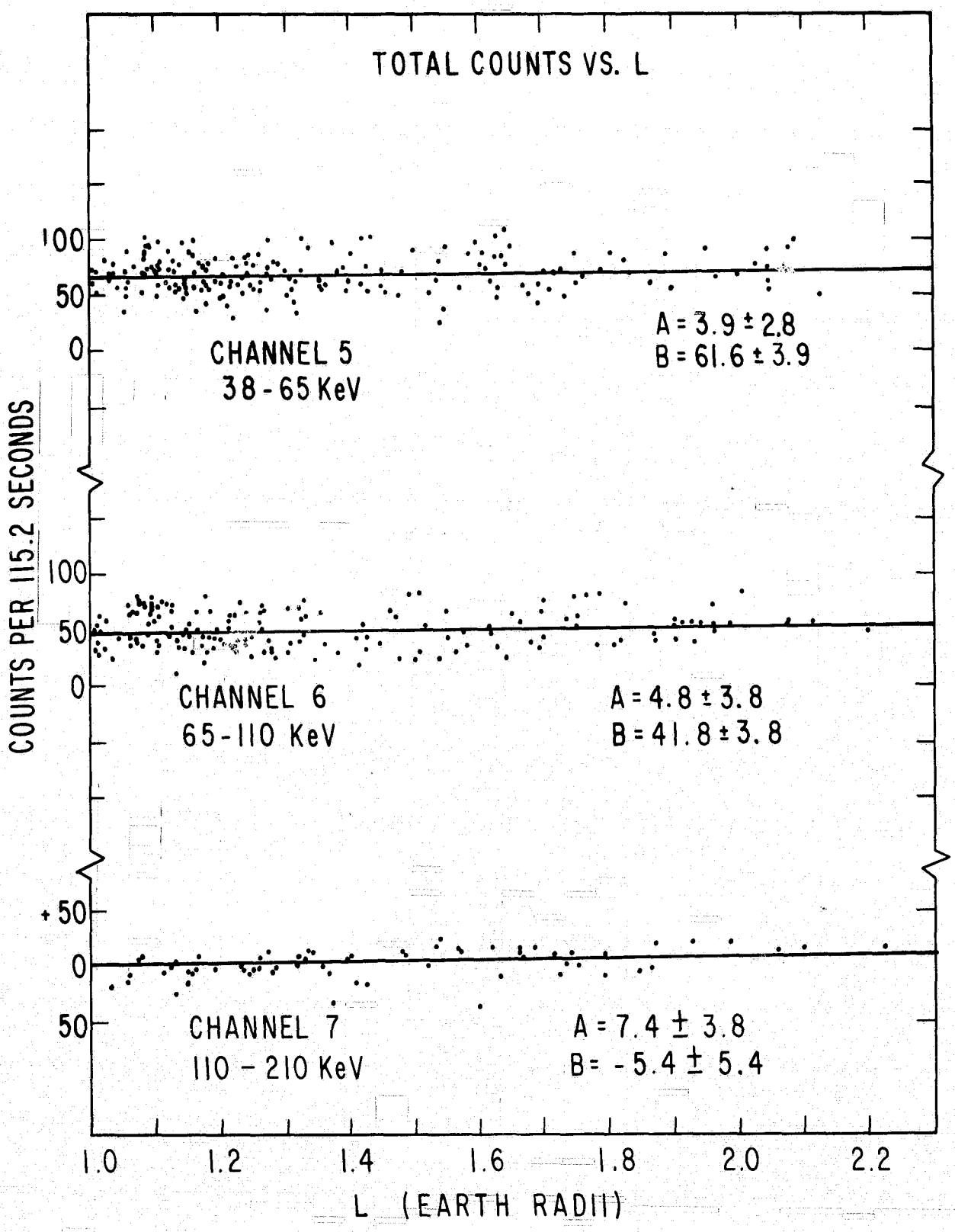

Fig. 18 Least squares fit of total count rates to L value, after radioactivity correction. The fit here gives marginal significance to A, (the coefficient of L), while allowing B to agree with the rate expected from previous diffuse X-ray measurements.

measured in the atmosphere, to derive the correction coefficients of Table 4. I place a ±50 percent error on these coefficients, since the data does not statistically eliminate $A_k = 0$.

In the South Atlantic trapped particle anomaly, proton fluxes of the order of $10^3(cm^2 sec)^{-1}$ may generate neutrons by nuclear interactions in the satellite. The sodium or iodine of the detector can capture these neutrons to form Na^{24} or I^{128}, which β^- decay with 15-hour and 25.6-minute half lives. Each disintegration appears identical to an X-ray event, since most electrons will lose all their energy before escaping the NaI crystal. Table 5 gives the ratios to channel 7 count rate predicted for each channel from the calculated β-decay electron spectra with endpoint kinetic energies 2.12 Mev (I^{128}) and 1.39 Mev (Na^{24}) [Blatt and Weisskopf (1952)]. Plots of channel 8 sun gate rates against time elapsed since in the radiation belts give the upper limits to I^{128} contamination shown in Table 5. To reduce the I^{128} limit a factor of 2, to eliminate possible fluorescence effects, and to account for some uncertainty in defining the location of trapped protons, the analysis program does not accept data for 30 minutes after the satellite leaves the radiation belt.

Because periods of time in which the satellite orbit misses and periods during which it penetrates the South Atlantic anomaly both compare with the 15-hour half life of Na^{24}, and since the 10-minute maximum spent in the belts each 96-minute orbit does not allow the activation to become saturated, the Na^{24} concentration should take many half lives to build up to a maximum, and then oscillate between that value and about half that maximum value. From the channel 8 sun gate,

Table 5

Radioactivity Corrections

Channel Energy (keV)	Electron β-Decay Spectrum. Predicted Count Rate Ratio to Channel 7 I^{128}	Na^{24}	Upper limit to I^{128} Contamination [sec^{-1}]	Average Measured Na^{24} Contamination Coefficient [counts per sec, at maximum activation]
7.7-12.5	0.036	0.023		0.0 ± .07
12.5-22	0.073	0.049		0.16 ± .03
22-38	0.126	0.093	0.005	0.55 ± .02
38-65	0.224	0.182	0.01	0.43 ± .01
65-113	0.43	0.39	0.02	0.65 ± .02
113-210	1.0	1.0	0.05	1.04 ± .03
> 210	19.7	10.9	0.5	

the same limit would apply to Na^{24} as well as I^{128} activation. Yet a definite, large 15-hour decay appears in plots such as Figure 15. If the reaction Al^{27} $(n,\alpha)Na^{24}$ takes place throughout the satellite then the 2.75 and 1.37 Mev gamma rays from the daughter Mg^{24} could produce background counts by the same mechanism as cosmic ray induced gamma rays. The increase in count rate during the first month of satellite operation (Figure 26), while the shield LLD degraded rapidly, supports this mechanism. Because of this I eliminate the first two weeks in orbit from diffuse component analysis.

Figure 19 shows a least squares fit of the total counts to

$$B_k + A_k \exp\left[-\frac{\ln 2}{15}(t-t_B)\right] \qquad (14)$$

with $t-t_B$ the time in hours since in the anomaly. I determine A_k for each 5 to 8-day accumulation of data on one magnetic tape. Here, about one-third of the data gives unacceptable fits. I average the coefficients from acceptable fits in each energy channel to report the correction of Table 5. The error reported equals the standard deviation of the mean, estimated from the scatter of the individual A_k.

Hicks, et al. (1965) reported a phototube noise count rate of 0.05 per second in the lowest channel, at a temperature of 22°C, (but not on the flight instrument). A measurement of the flight telescope in a lead hut several months before launch gave a total count rate 0.14 sec^{-1} in channel 2. Because tube noise has a very steep equivalent energy spectrum, with e-folding energy about 1 keV, noise will contribute negligibly to any higher channel, but will contribute to channel 2

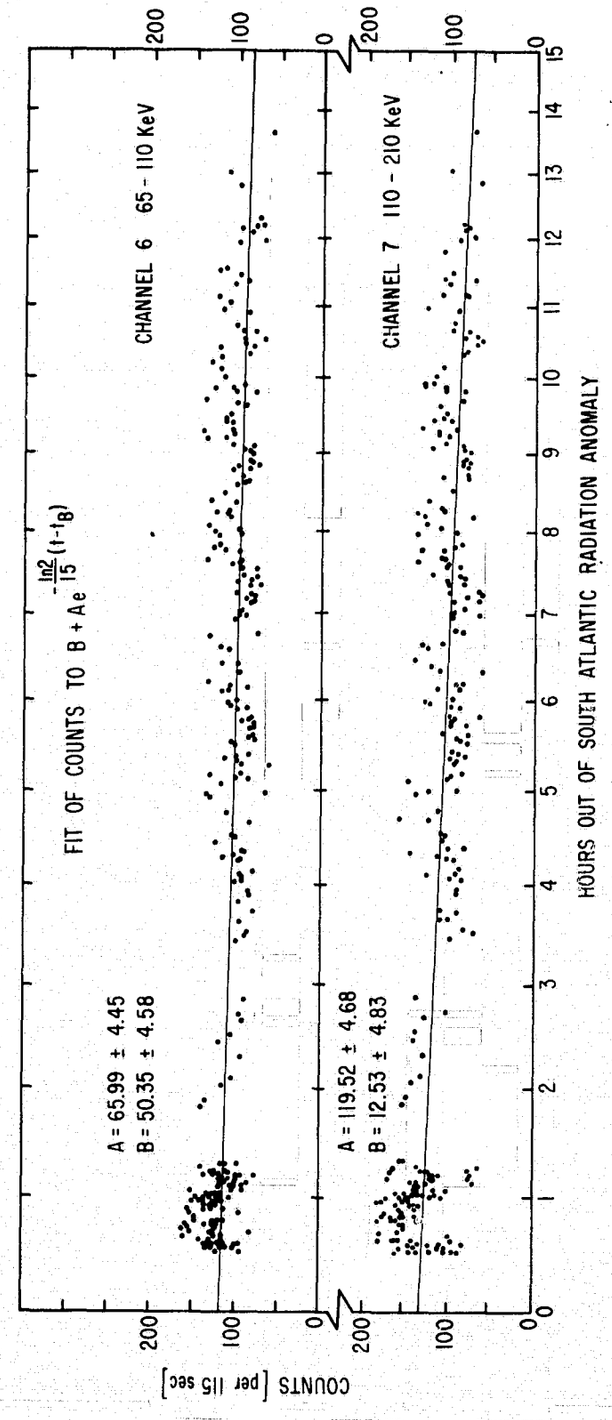

Fig. 19 Least squares fit of total counts to a constant plus a 15 hour half life decay component, to determine coefficients A used in correcting for background due to radioactivity.

with a sensitive dependence on the precise lower energy threshold. I obtain an upper limit to the tube noise from the channel 2 count rates when the earth fills the telescope aperture. This count rate varies greatly in time, presumably due to sporadic production by trapped particles precipitating into the atmosphere. However, a fairly well defined minimum rate of .10 ± .05 counts per second exists; I take .07 ± .035 as the PM tube noise contribution. Because of the independence of the PM noise counts and the telescope direction, this must contribute a completely isotropic background.

Charged particles associated with the geomagnetic environment provide by far the most damaging source of background. An intensity of only 10^{-4} electrons $(cm^2 \text{ sec keV ster})^{-1}$ between 300 and 400 keV would contribute about 1 percent of the apparent X-ray counts. Such an intensity falls far below the sensitivity of measurements made by any experiments studying the trapped particle environment. Although our experiment cannot directly distinguish charged particles from X-rays, channels 2, 3, and 4 definitely count diffuse X-rays because sometimes the sky rates, away from the sun or known discrete sources, exceed the earth rates measured at the same time by factors of about 20, 8, and 3 respectively, even though the telescope views parts of the earth and sky at the same angle relative to the magnetic field.

We observe the particle contamination to vary in time throughout the region of B-L space covered by the satellite. Figure 20 shows channel 5 count rates, measured by the total counts monitor during a two-minute interval, on a B-L map. Below the solid line the 12-bit total counts scaler always overflows (rate > 25 sec^{-1}), and penetration

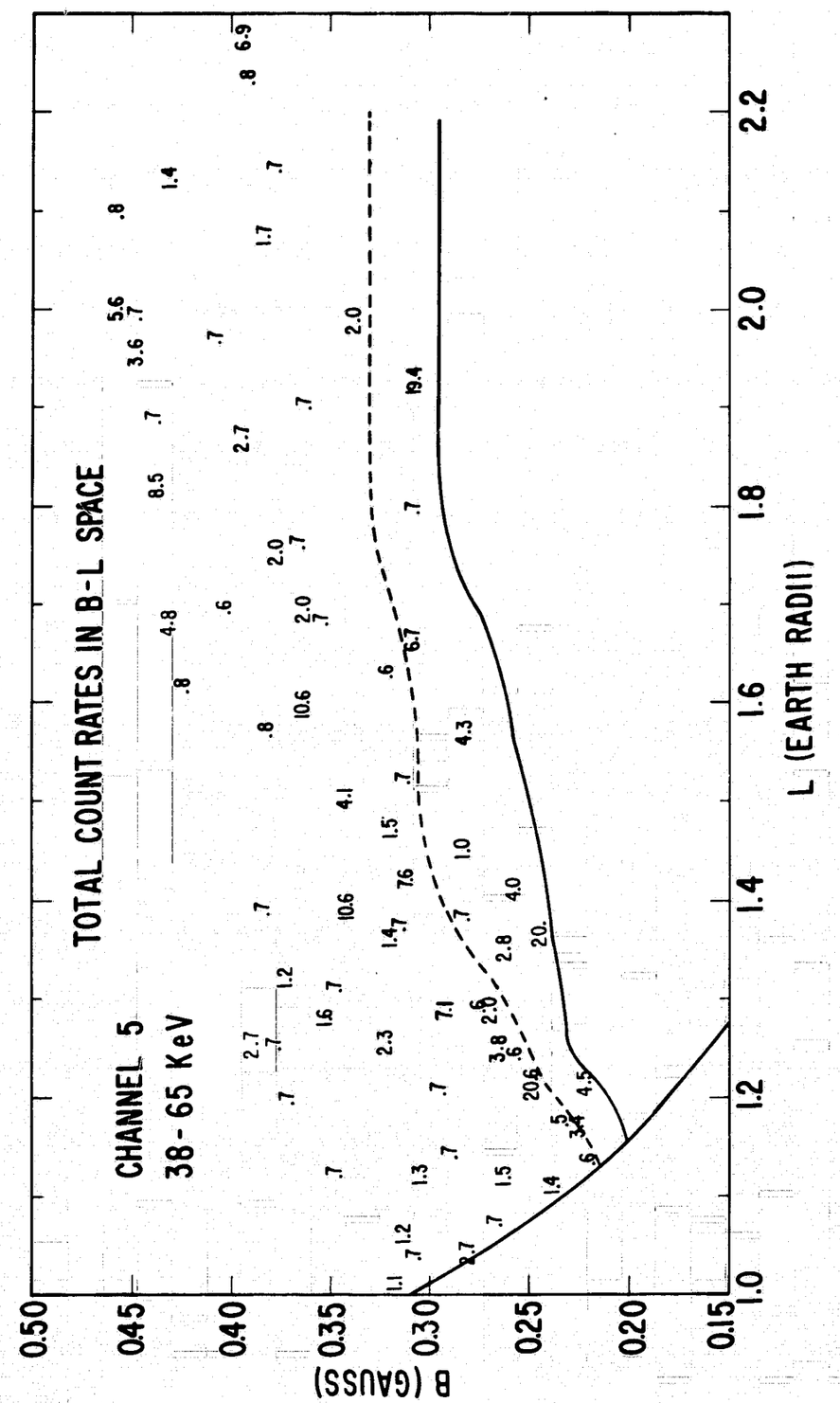

Fig. 20 The decimal point represents the average B-L position of the given count rate. The points have about 10 percent standard deviation. A stable minimum rate of 0.7 per second exists independent of B-L position. Charged particle contamination also occurs at all B-L points covered by the satellite.

of that line serves as the definition of "in South Atlantic anomaly" for making the radioactivity correction in equation (14). Above the dashed line a stable minimum count rate prevails. The analysis program only used data from the B-L region above this dashed line. I have deliberately selected certain contamination events to illustrate their dynamic range, so Figure 20 overemphasizes the true relative frequency of large events.

Figure 21 plots some two-minute directional count rates versus angle to the magnetic field line. Although the angular count rate distribution often has peaks perpendicular to the field, enhanced count rates sometimes appear in the loss cone. Many other experimenters have reported widespread electron precipitation [Freden (1969) gives other references], so I assume that electrons cause most of these particle effects. The dependence of these count rates on magnetic field direction establishes this contamination as charged particles rather than some kind of time varying X-ray activity.

Figure 22 shows differential count rate spectra of large precipitation events obtained from the sun gate readouts at night. These spectra agree qualitatively with the predictions obtained by calculating the ionization energy loss in 92 mg/cm^2 of beryllium (but without taking account of straggling) of steep incident spectra of electrons. The count rate decreases in each lower energy channel. Figure 23 shows the channel 2 to channel 8 count rate ratios for many large events versus the channel 8 rate. The channel 8 sun gate rate has poor statistical accuracy because it receives only two seconds exposure for day or 16 seconds for night during a two-minute sector

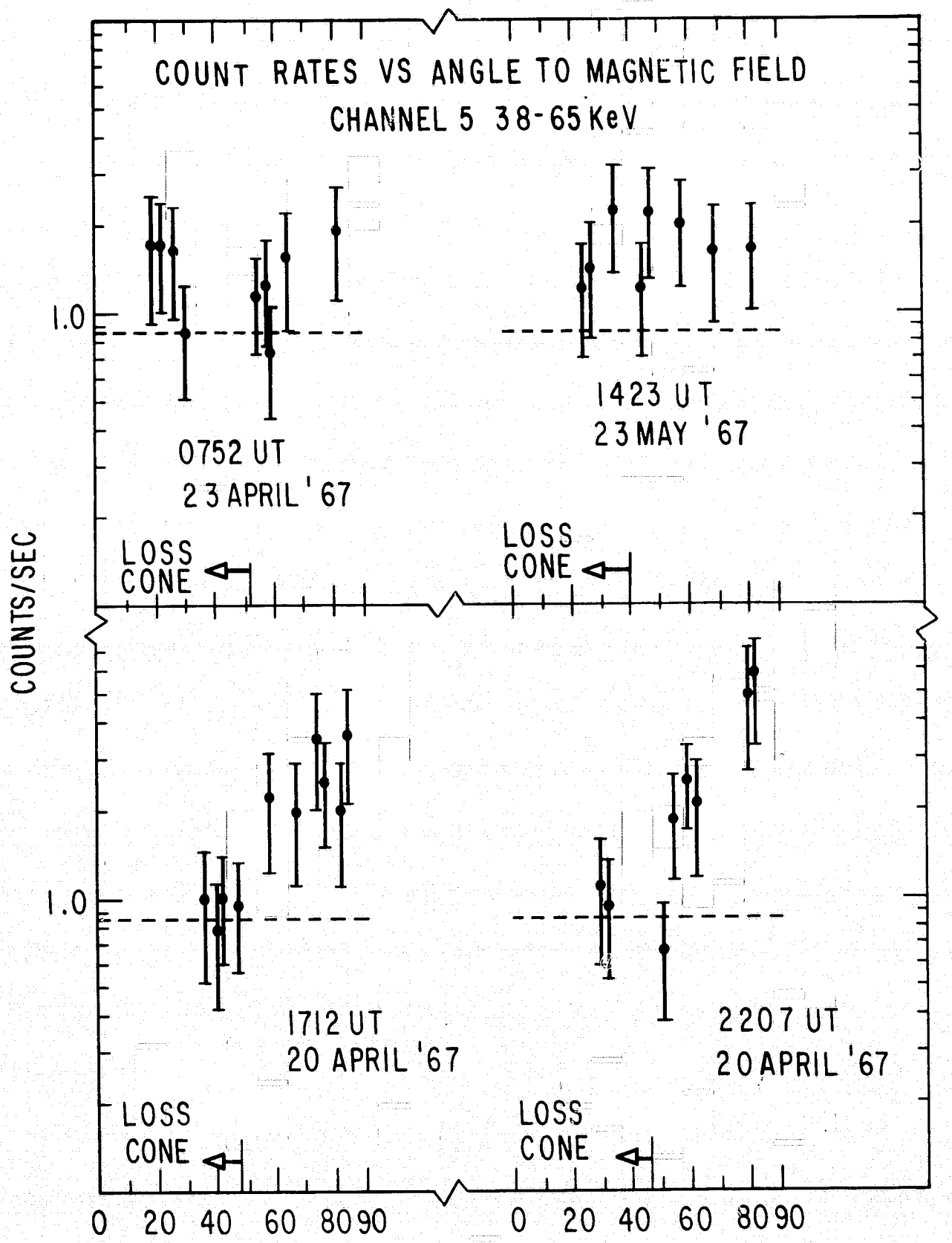

Fig. 21 Pitch angle distributions during four fairly small contamination events. Dashed line represents the average count rate due to diffuse X-rays and radioactivity. The excess in the bottom events might represent stably trapped particles; the top events show particles which will precipitate into the atmosphere.

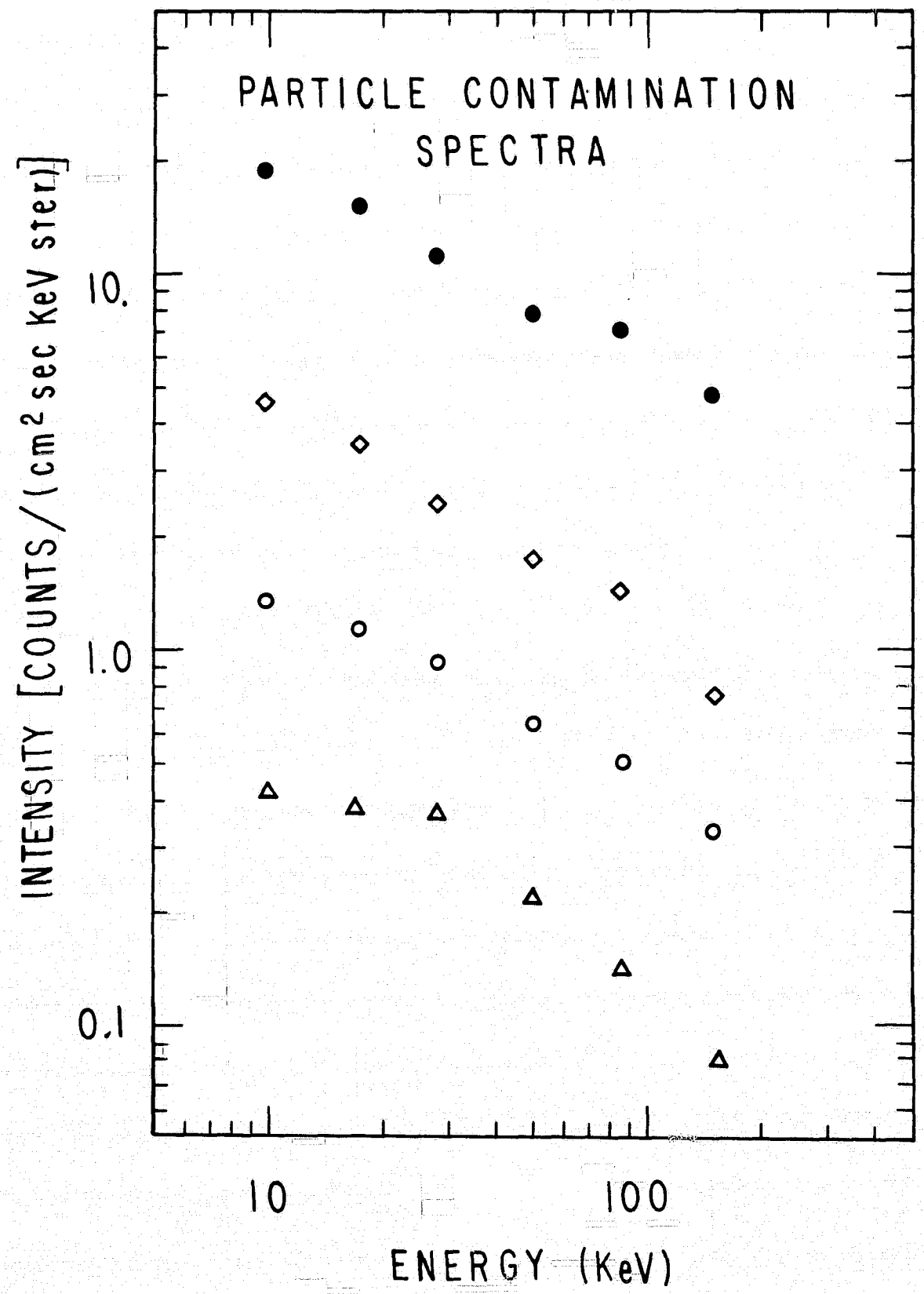

Fig. 22 The equivalent spectra of four very large electron contamination events. I assume that this spectral shape also applies during much smaller contamination events.

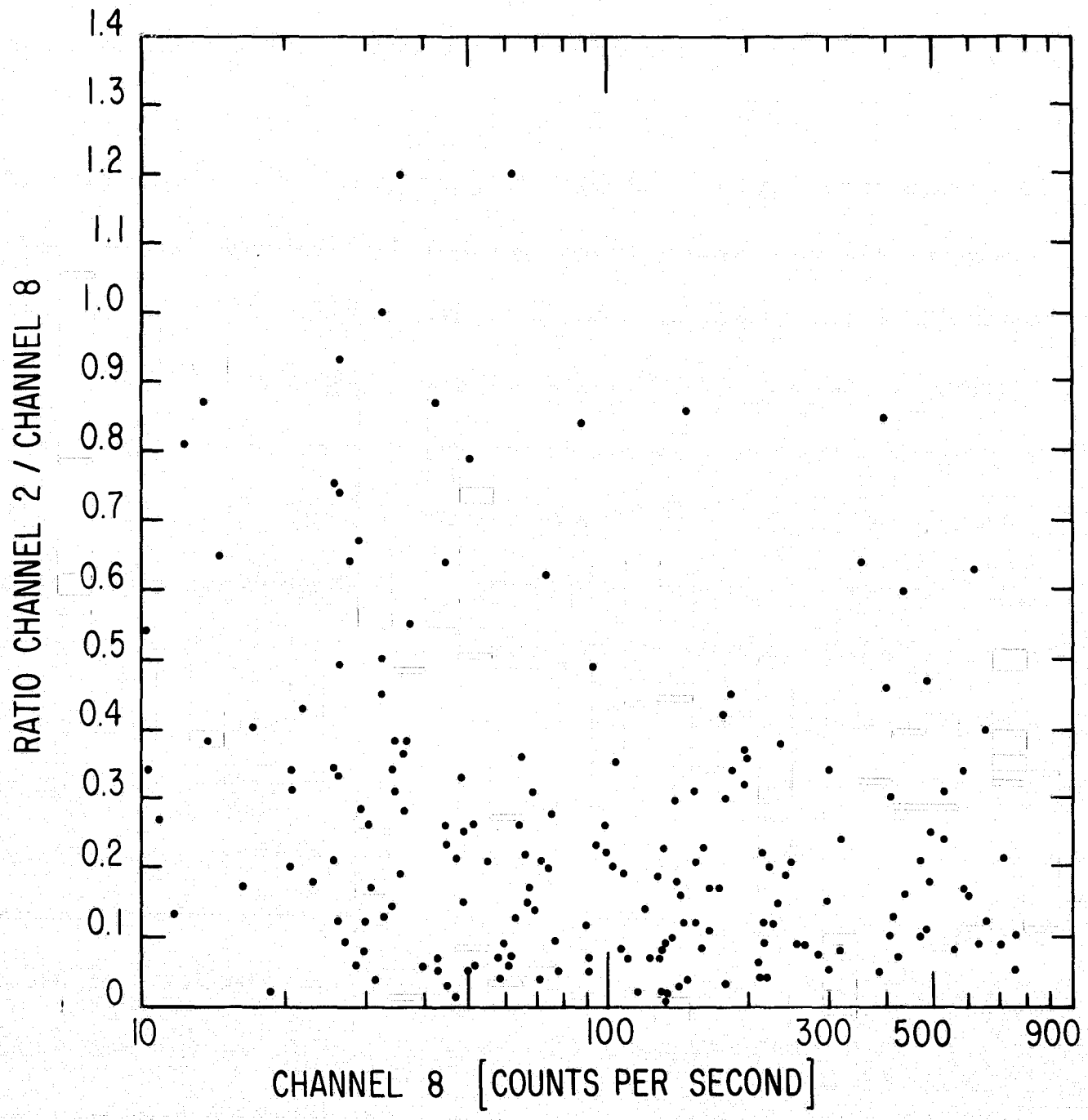

Fig. 23 Channel 2 to channel 8 sun gate rate ratio for large contamination events. Channel 2 usually counts at no more than 20 percent of the channel 8 rate during such events.

energy channel. It has a minimum count rate of 1.5 ± .5 per second. As an empirical criterion to attempt to limit particle contamination, the analysis program only accepts a sector energy channel with a channel 8 count rate less than 3.0 per second during orbit day, and less than 2.0 per second during orbit night.

In Figure 24 I plot frequency of occurrence of a two-minute total counts rate against the rate, for about one month of data. I try to fit such plots by normal distributions with the standard deviation expected for the two-minute counting interval. In all cases at least the lower portion appears as statistical fluctuations about a fixed mean, with various contaminations resulting in too many high count rate occurrences. As another criterion to limit charged particle contamination, the analysis program rejects data for which the total count rate exceeds by two standard deviations the mean of a normal distribution as determined by plots similar to Figure 24.

Because the diffuse count rate contributes least to channel 7, no more than 10 percent of the total channel 7 counts, this channel serves to check to what extent any background can show up as an artificial angular structure. The most important sources of background vary in time, and therefore vary in apparent celestial position since less than half the scan circle receives full sky exposure at any time. Charged particle contamination lasts at most 10 minutes, although it may repeat near a given location during several successive orbits. Thus it could lead to an apparent anomalous emission at certain discrete points of the sky. I expect differences in radioactivity contamination to vary much more continuously over the sky. In discussing

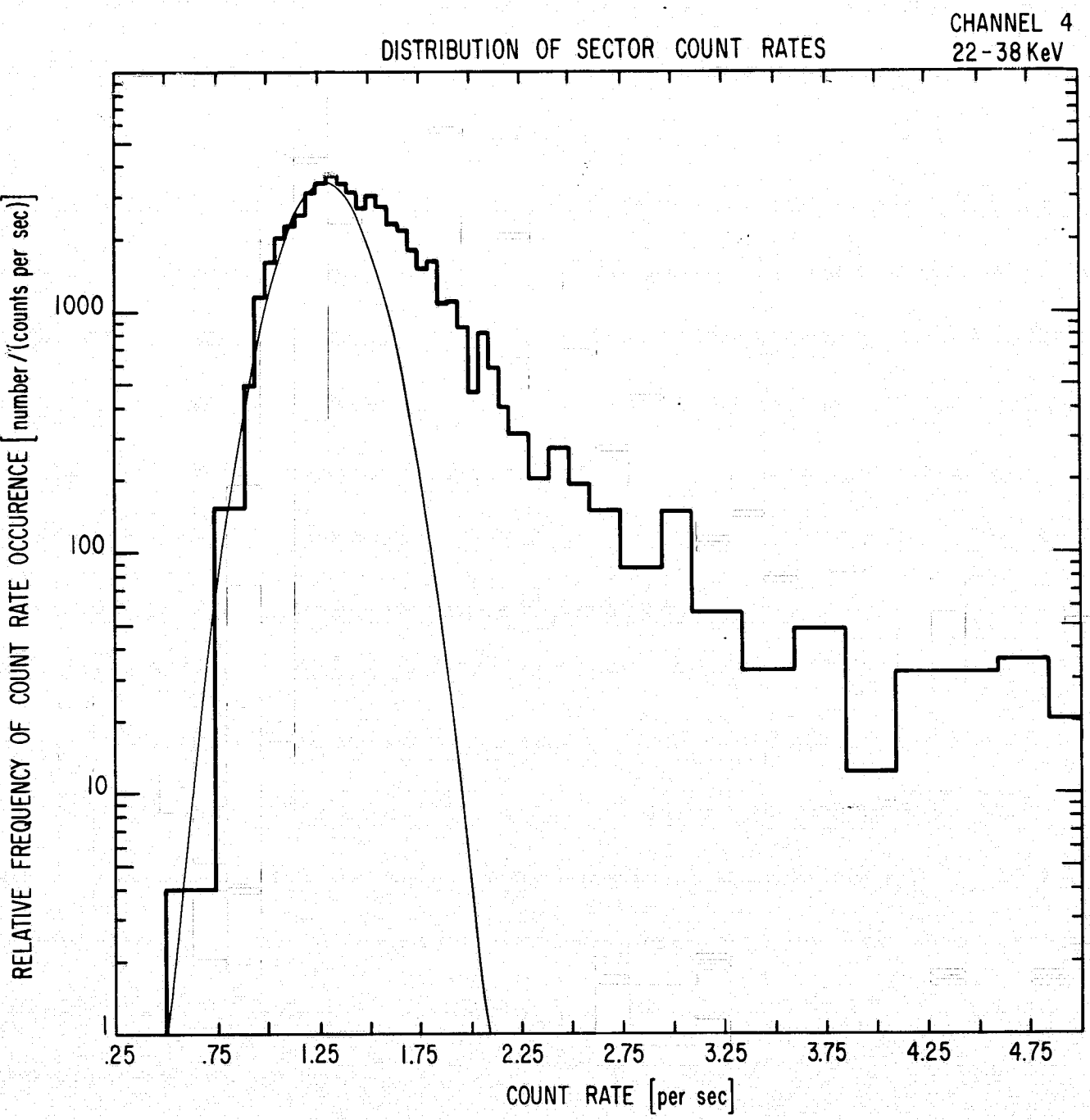

Fig. 24 Relative number of occurrences of the two minute average count rate deduced from the direction mode, in a given range of count rate. The solid line has the correct normal shape for the standard deviation expected for a two minute sample; I adjust the peak for best agreement.

results, I accept any measured isotropy because of the unlikelihood of anisotropic background just balancing a true cosmic anisotropy. However, any measured anisotropy in the cosmic X-rays requires further investigation.

The data reduction, as described so far, has averaged the number of cosmic X-ray counts corrected for background and the corrected live time in each 6° scan sector over a four- to eight-day period. A single magnetic tape contains these along with the time averaged positions of the scan sectors. Actually, the programs generate and store several complete sets of counts and exposure times selected with somewhat different background criteria, in order to study any effect of these selection criteria on the diffuse X-ray distribution. The program stores separately data obtained during satellite daylight and eclipse, to compare for consistency.

4. Verification of Operation

All evidence indicates that the UCSD X-ray telescope functioned properly during the first two years in orbit. On a large time scale the synchronization, energy subcommutation, and interruption for anti-coincidence rates patterns have continued unbroken. A very strong assurance comes from the ability to interpret the solar X-ray data [Hudson, et al. (1969b)], as well as the general consistency of the cosmic X-ray data studied here.

One error has appeared in the instrument logic. For the directional mode the nominal channel 2 always accepts freely counts from both channel 2 and channel 3. This shows up during moderate sun or charged particle events which produce enhanced sun gate count rates

only in channels 2 and 3. At such times the channel 2 total counts rate equals the sum of the channel 2 and channel 3 sun gate rates. The number of counts during these events suffices statistically to eliminate other possible explanations for the disagreement between the channel 2 sun gate and channel 2 total counts rate. I can attribute this to the failure of a single diode in the sector energy selection matrix, which must have occurred before our first sun event, 12 minutes after turning on the experiment in orbit. To report spectra I generally subtract the channel 3 rate first and use the nominal energy channels. However, for studying the angular distribution I treat channel 2 as a 7.7 to 22 keV band.

BBRC calibrated the energy thresholds prior to launch by measuring the ratio of channel 6 to channel 7 count rates produced by a Co^{57} source, which has a line at 123 keV. This ratio, compared with the same spectrum measured in the NaI crystal by a multichannel analyzer, established the channel 6 and 7 energies. The previously measured amplifier gain ratios then determined the energies of the other edges. Two firm limits bracket the possible absolute gain change. The upper limit of 0.2 counts per second for channel 2 when looking at the earth, prohibits a gain increase lowering the channel 2 threshold to 6 keV, above which energy the prelaunch measurements of phototube noise pulses would predict a rate of at least 1.0 counts per second. Figure 25 shows the atmospheric X-ray spectra measured on OSO-III and measured at 3 gm/cm^2 with the prototype OSO telescope mounted at 90° to the zenith [Jacobson and Peterson (in preparation)]. The atmospheric spectrum turns over below about 30 keV because of photoelectric absorption by

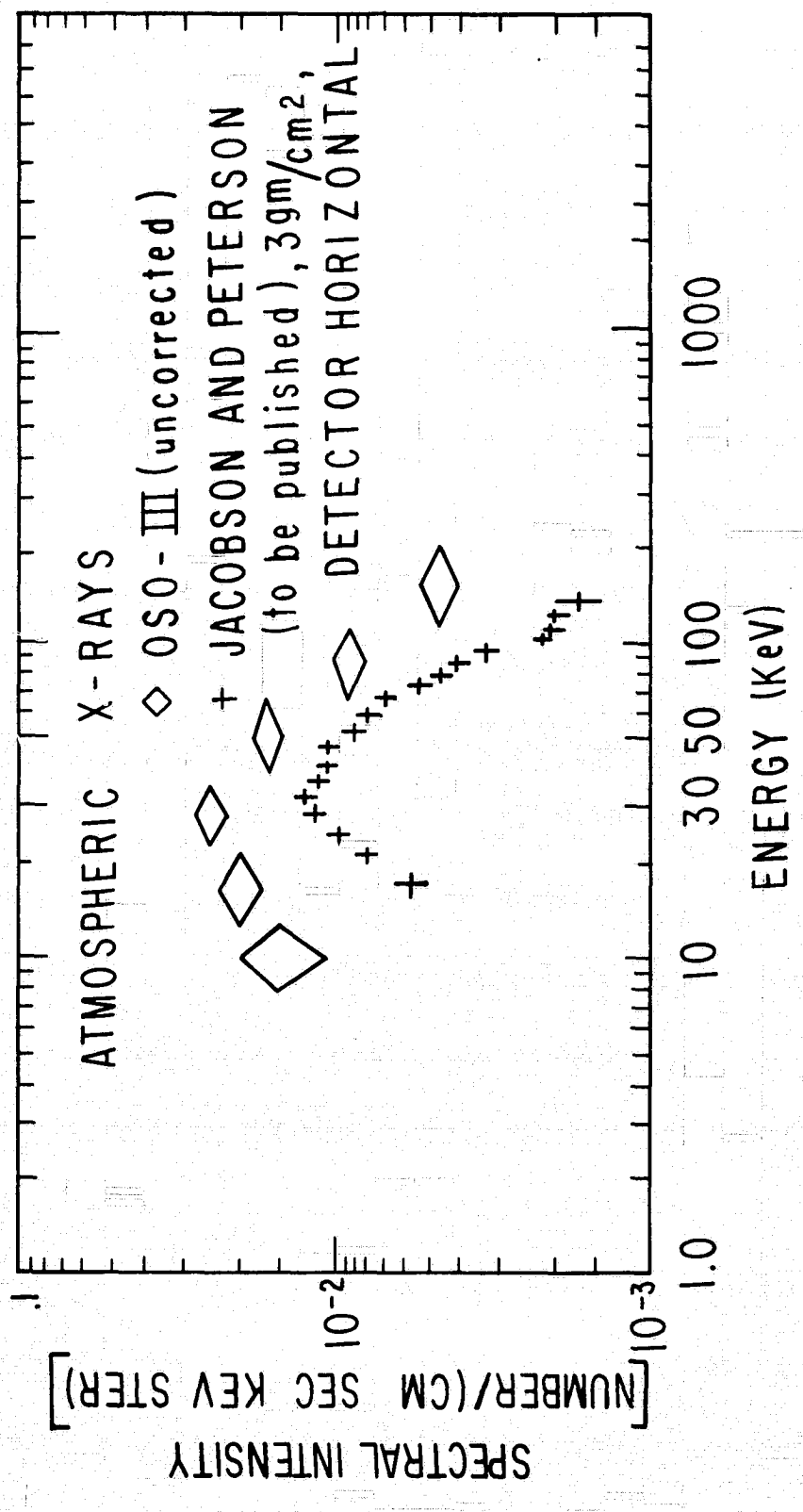

Fig. 25 Comparison of the position of the peak measured in the atmosphere, with the OSO-III albedo spectrum, establishes the true calibration as within 20 percent of the pre-launch value.

nitrogen and oxygen. The nominal 22 keV channel 3 upper edge cannot exceed 29 keV or the measured channel 3 intensity would have exceeded the measured channel 4 intensity. (This OSO-III earth spectrum does not contain the background corrections discussed above.)

As shown in Figures 26 and 27, the relative gain over one year remains more accurately stable. Figure 26 shows four- to eight-day average sky intensities away from the galactic plane (but susceptible to SCO XR-1 in May and June), corrected for live time but with no background corrections. The minimum trend remains stable, with many areas of apparent contamination. This figure shows the buildup of radioactivity in the first weeks of orbit. Day and night rates can differ because of different exposures to the celestial sphere, and because the geographic location of particle contamination can systematically occur either in the sunlit or the eclipse portion of orbit. The abscissa in these plots actually represents the reduced magnetic tape number; thus the real time has some slight distortions.

Figure 27 shows the same quantities, but with the background corrections described above. Evidently, channel 6 has too much radioactivity correction prior to mid-May. The error corresponds to 0.05 per second in channel 6, and therefore less in the lower channels according to the last column of Table 5. Even in this plot individual points stand several standard deviations above the general averages. These could reflect true diffuse angular variations, but I first compare the parts of the given scan that overlap with other scans. If the areas of sky in common show the same significant difference, I

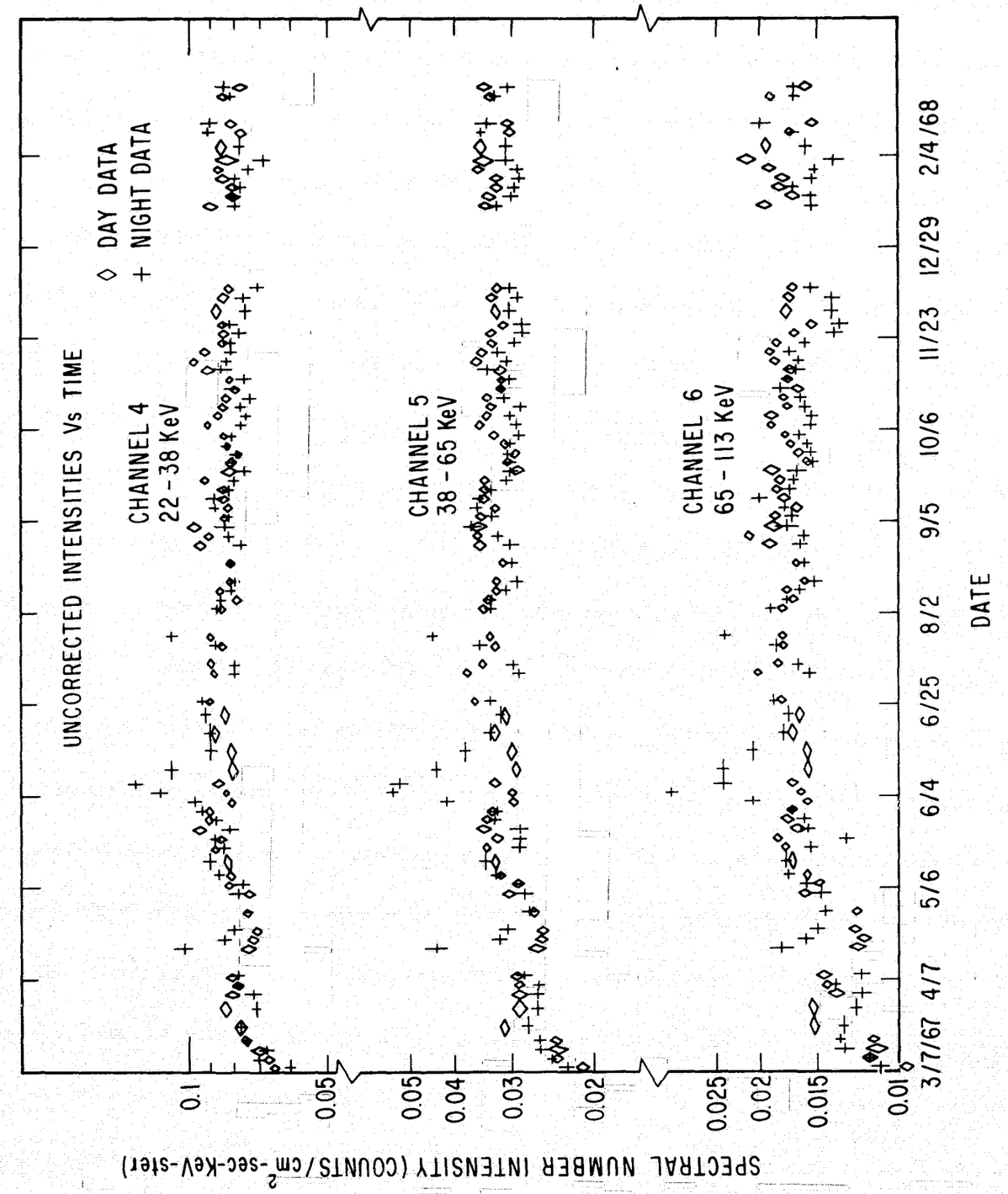

Fig. 26 Uncorrected diffuse count rates vs. time, (actually plotted for each analysis tape, which on the average contains six days of data).

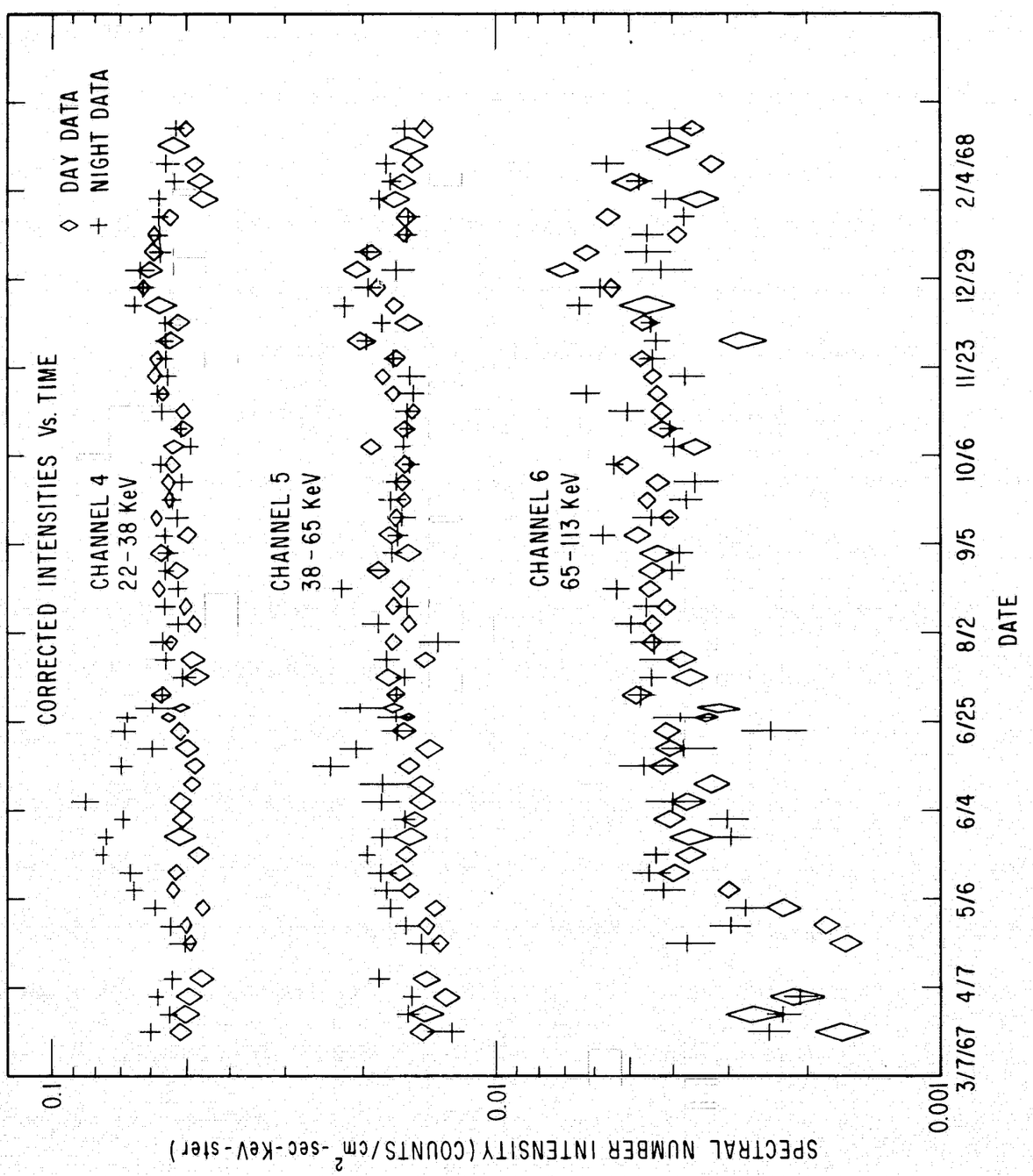

Fig. 27 Same as Figure 26, except the rates contain background corrections, and have selection criteria designed to minimize charged particle contamination.

assume it due to background contamination and discard the entire several days of higher rates.

III. RESULTS

The procedures described in Chapter II result in the acceptance of about 25 percent of the data for cosmic X-ray analysis. A magnetic tape now contains counts and live times at celestial points which represent an average over solid angle of 6° along a scan circle and the precession of this circle during four to eight days. (The scan circle precesses an average of 1° per day.) To prepare the contour maps of Figures 28 to 33, a computer program sorts these counts into bins of 6° in galactic latitude, and approximately 6° in galactic longitude, with the exact longitude width chosen so that an integer number of bins spans 360° at the midpoint latitude. From the rates in each bin, I drew the contour lines freehand by linear interpolation between adjacent bins. This gives contour positions to about 2° accuracy; greater precision than the data justify. I chose the lowest level contour about ten percent above the mean rate at high galactic latitude, and other levels somewhat irregularly to display the data. As the count rate decreases from channel 2 to channel 6, this lowest level corresponds roughly to from 2.5 to 1 standard deviations of the count rate in a single bin. (This explains the more extended contour lines in channel 6.) The discrete galactic sources provide the main features of these maps. The lowest level contours outside the galactic plane do not correspond well in the different energy ranges.

Channel 7 (Figure 33) does not contain any background corrections, to illustrate what anisotropies background may display. The majority of the sky does not appear affected. The highest channel 7

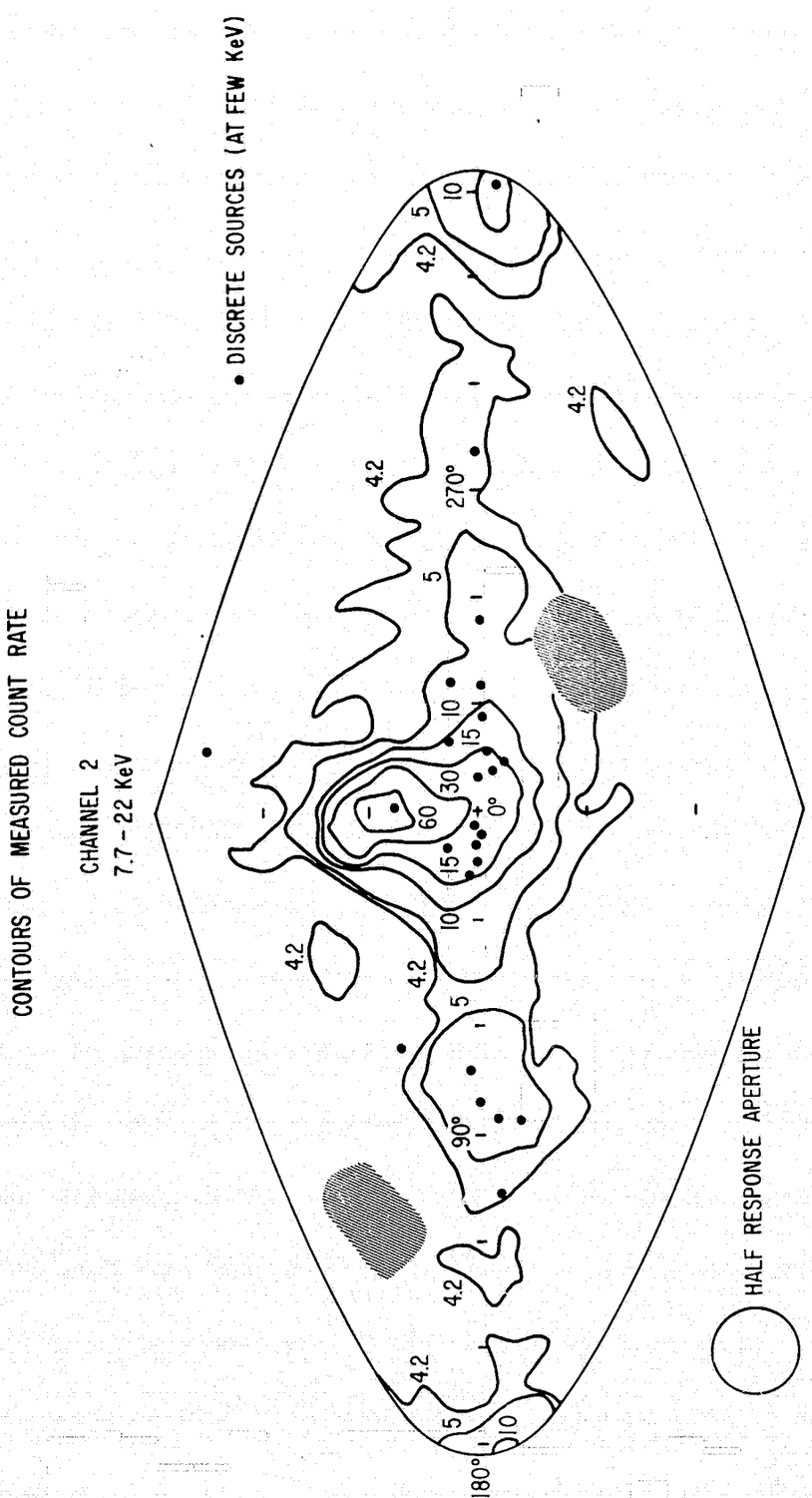

Fig. 28 Contours of constant measured count rate, plotted in galactic coordinates. The detector did not scan the shaded areas around the celestial poles. The half-response aperture has approximately the same size throughout the map. See Table 1 for conversion of counts per second to flux or intensity. Average count rate at the poles equals 3.8 per second.

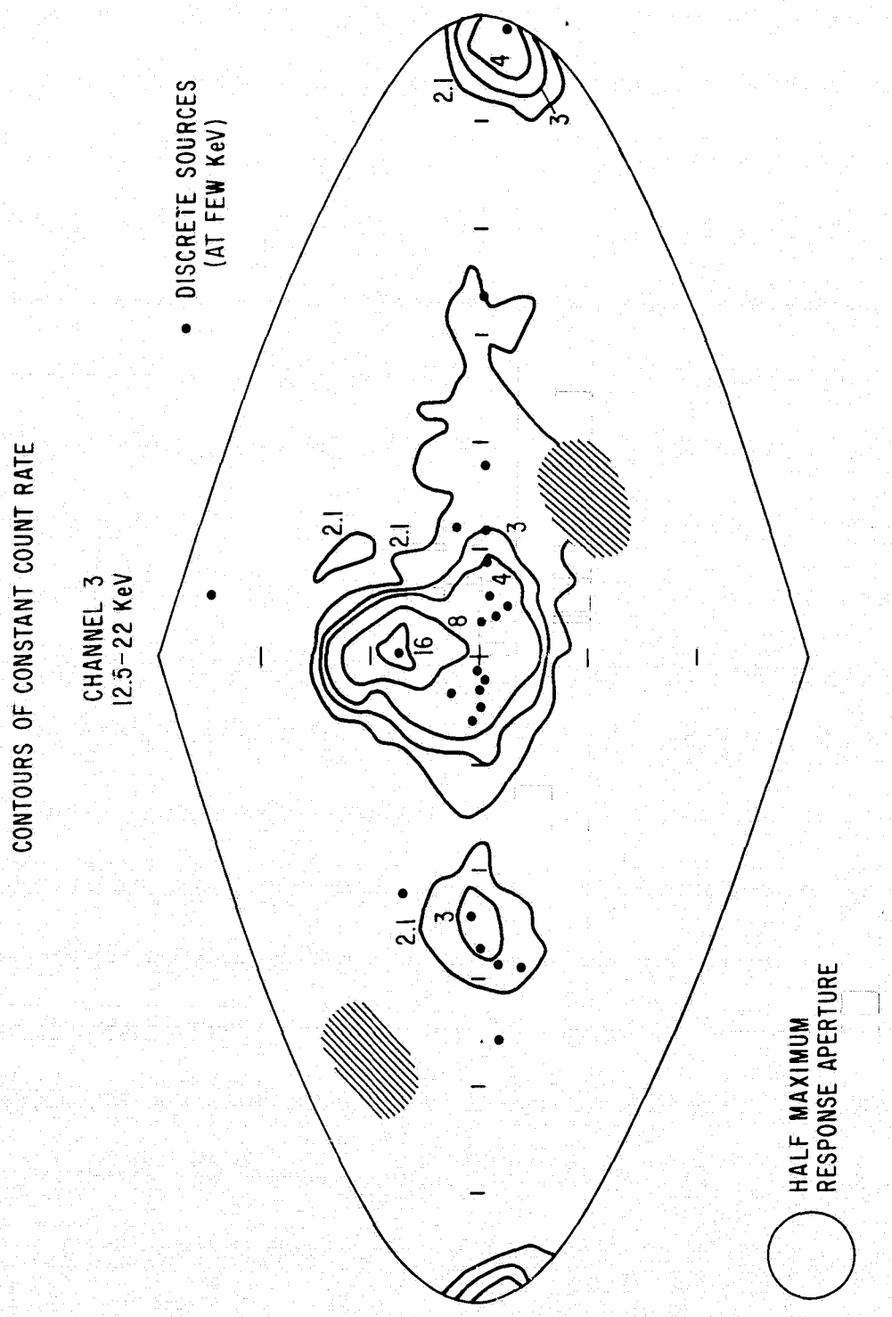

Fig. 29 Same as Figure 28, for energy channel 3, corrected for background. Average rate at the galactic poles equals 1.76 counts per second. Friedman, et al. (1967), and Chodil, et al. (1967), reported the discrete source positions shown on these maps.

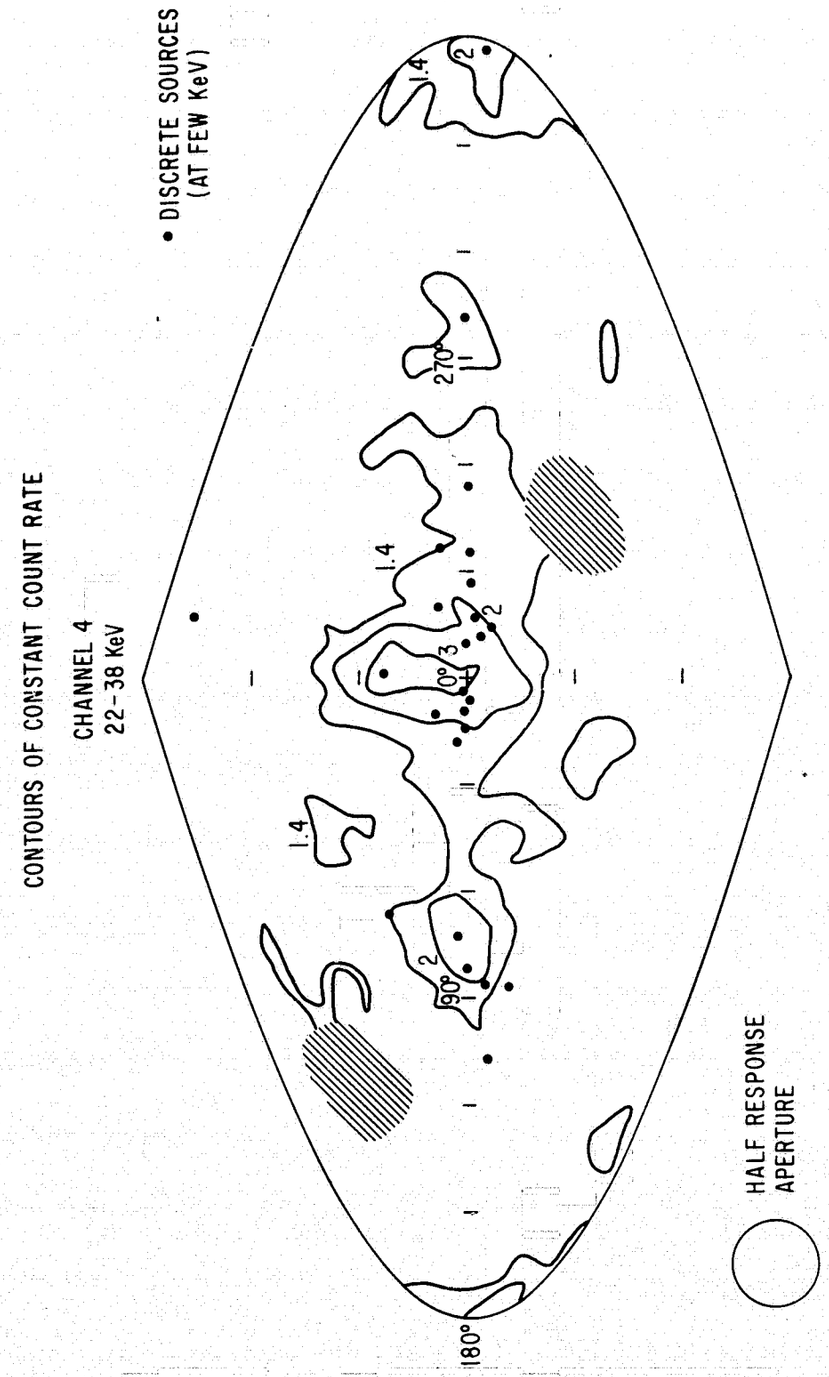

Fig. 30 Same as Figure 28, for energy channel 4. Average rate at the galactic poles equals 1.19 counts per second.

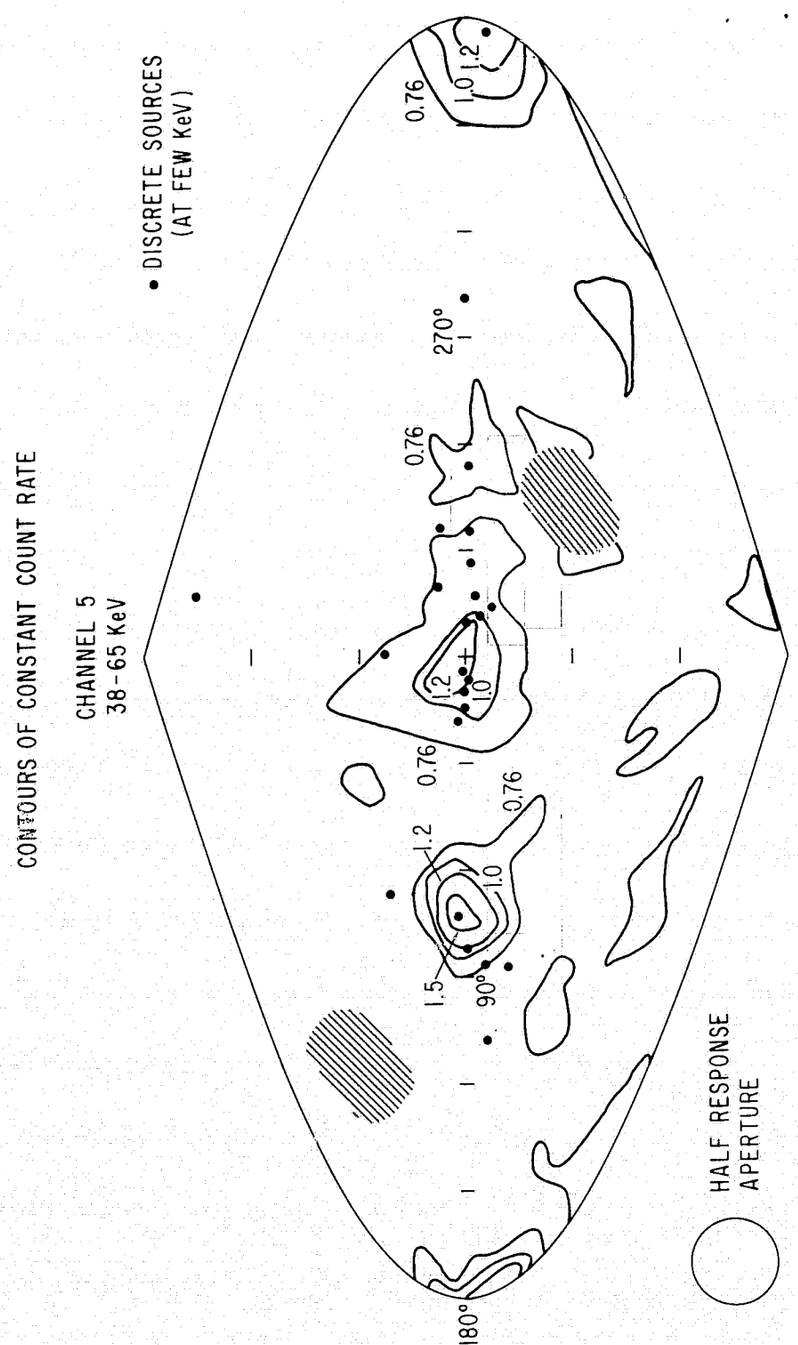

Fig. 31 Same as Figure 28, for energy channel 5. Average rate at the galactic poles equals 0.645 counts per second.

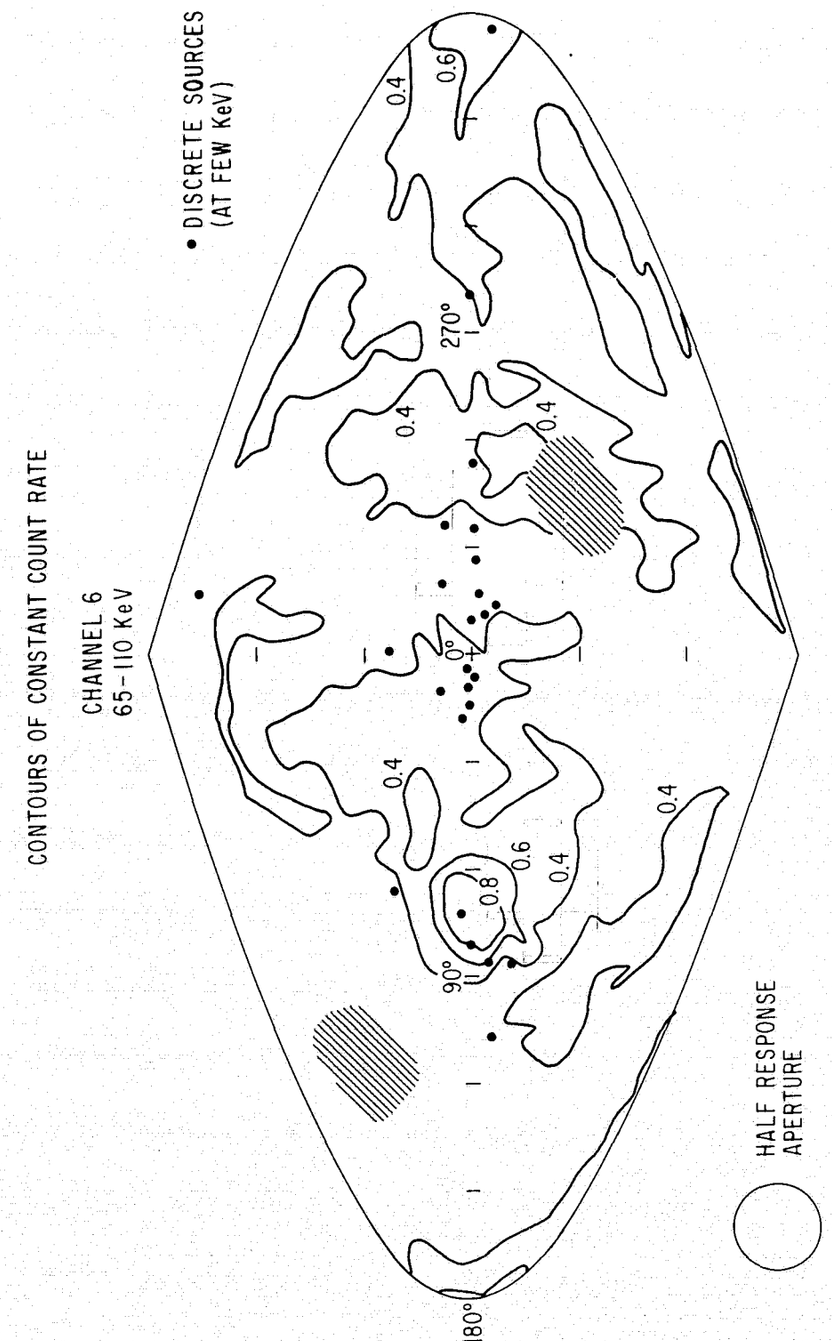

Fig. 32 Same as Figure 28, for energy channel 6. Average rate at the galactic poles equals 0.319 counts per second.

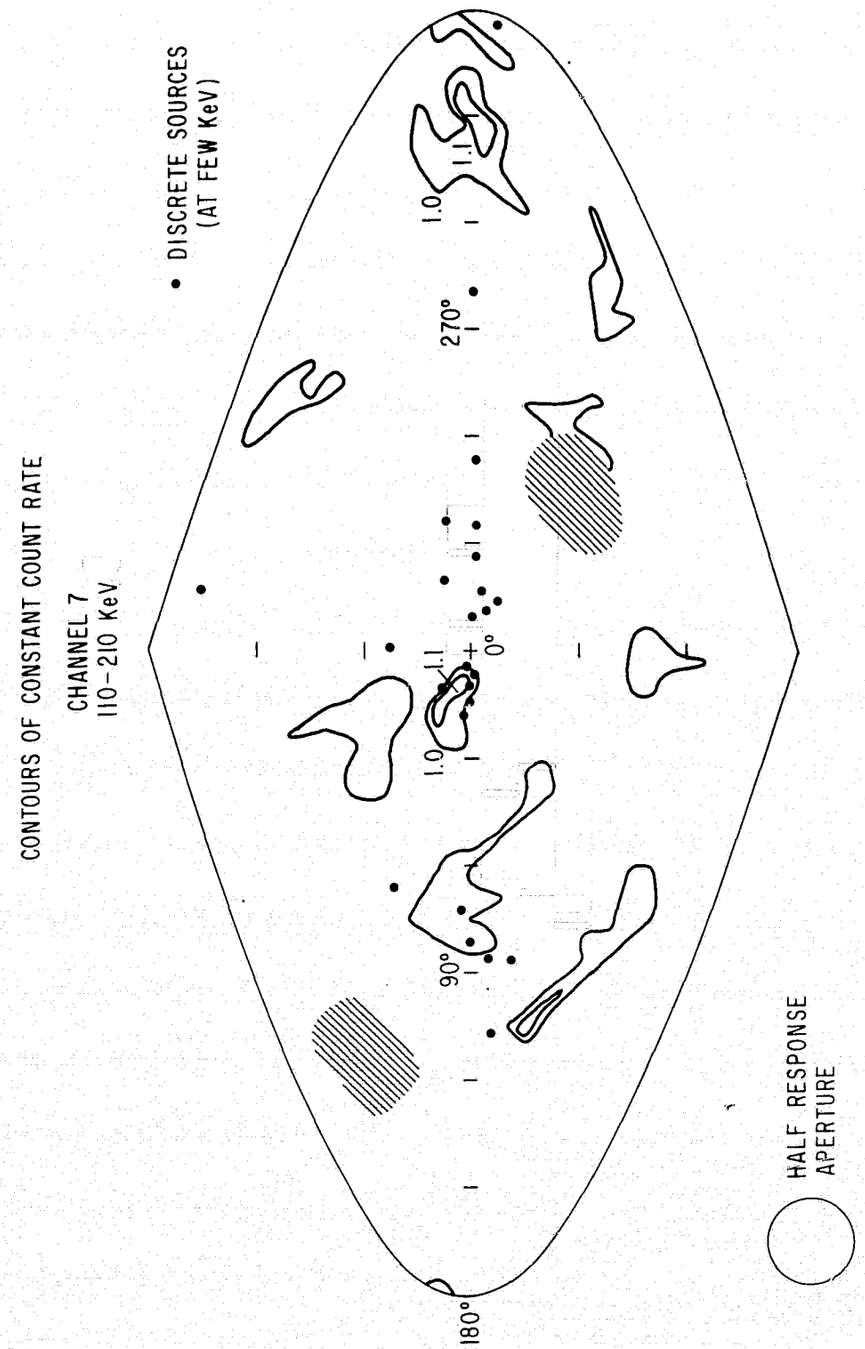

Fig. 33 Similar to Figure 28, for energy channel 7, but with no background corrections. The contours primarily represent statistical and background fluctuations. Average count rate at the galactic poles equals 0.852 counts per second.

contour corresponds to 0.35 excess count per second, which from Figure 22 would correspond to about 0.07 count per second contamination in channel 2. Such a two percent effect begins to exceed statistical errors, but still allows a serious analysis of the angular distribution.

I emphasize that these maps present measured average count rates with the X-ray telescope pointed in a given average position. Not only the telescope response of 23° full width at half maximum, but also the telemetry sampling scheme, which can smear a discrete source 72° along the scan circle, severely distort the contours. Clearly, to study the diffuse component, I must first carefully eliminate the effects of discrete sources.

But I only wish to eliminate galactic sources, since the diffuse component may well result from the integrated effect of extragalactic discrete objects. I consider the list of discrete sources reported by the NRL group [Friedmann, et al. (1967)], plus Vela XR-1 and CEN XR-2 [Chodil, et al. (1967)]. For the 23° FWHM telescope the source positions need have no greater than 3° accuracy. For this list a computer program compiles count rates when the average telescope position, according to calculation, pointed within 7° of the reported source position, corresponding to the 80 percent telescope response circle. Subtracting the count rate obtained at galactic latitudes more than 60° outside the plane, gives an upper limit to a source strength. In general this upper limit exceeds other measurements of the source because of contamination by nearby sources. However, for the isolated source TAU XR-1, Figure 34 shows that the OSO-III spectrum

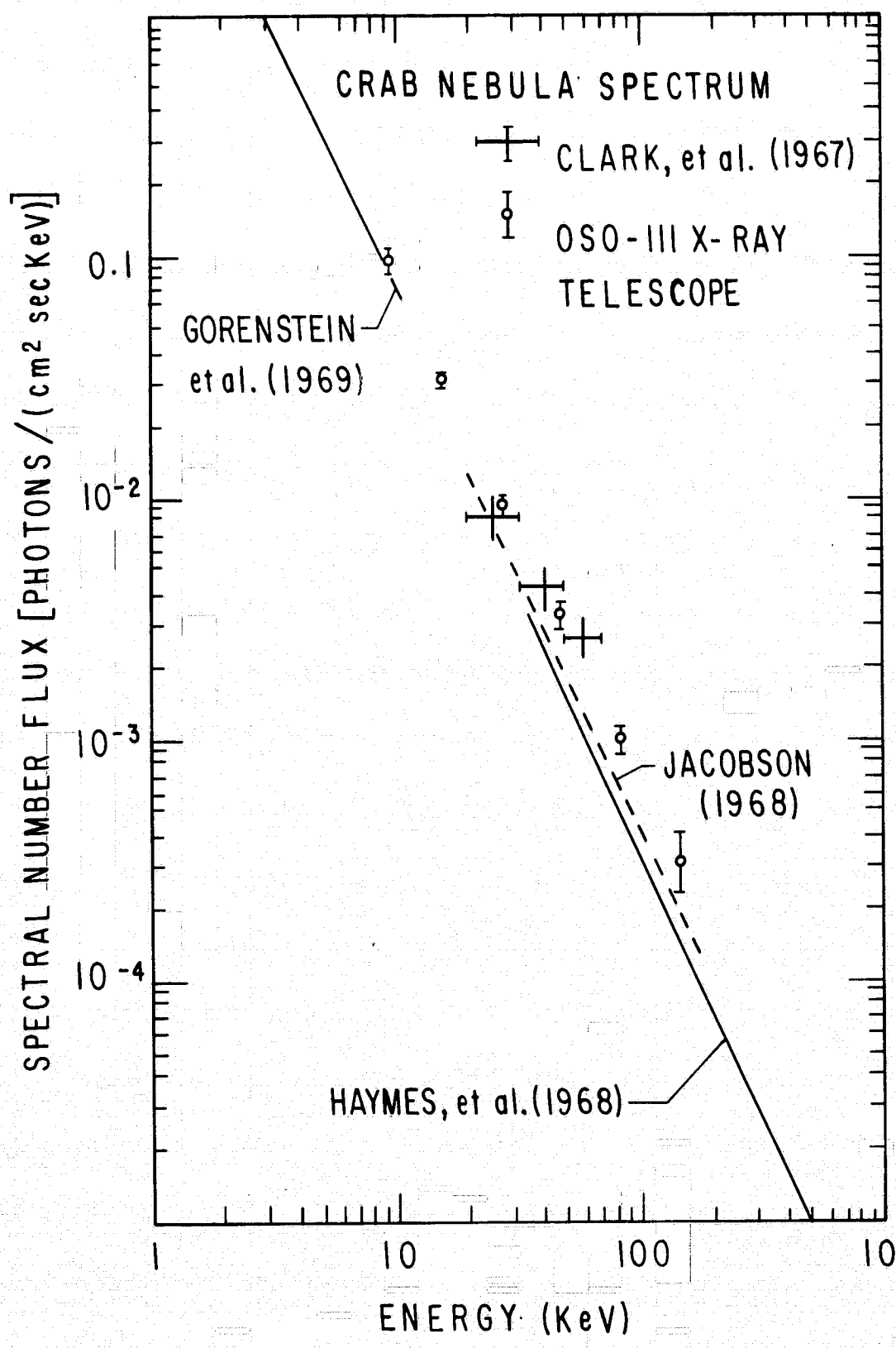

Fig. 34 Comparison of the deduced spectrum of the Crab Nebula with other recent results gives confidence in the OSO-III X-ray telescope calibrations, and data analysis. The reported errors in the "best fit" lines of Jacobson (1968) and Haymes, et al. (1968), could bring these lines within the OSO-III error bars.

gives results in excellent agreement with previous measurements. This gives added confidence in the aspect calculation, and in the detector geometry factors. Considering the telescope angular response, and the smearing inherent in the sector sampling scheme (Appendix B), the analysis program eliminates all sectors to which a discrete galactic source emitting at the determined upper limit rate could possible contribute as much as 1 percent of the total count rate. Most further discussion refers to X-rays after this discrete source elimination. However, I do also examine the data with a less conservative discrete source elimination, letting the telemetry jitter extend only one 6^{o} bin past the 1 percent telescope response for all sources except SCO XR-1, TAU XR-1, and CYG XR-1. This weaker source rejection gives at most a few percent increase in count rates. In some places measured rates decrease with the additional photon statistics.

A. The Spectrum of the Diffuse Component

Although the OSO-III telemetry only provides six, fairly wide channels of spectral information, these points have greater statistical accuracy than any previous measurement, and cover an energy range which no single experiment has spanned. An analysis program lumps all counts taken within 30^{o} of the galactic poles to calculate the differential spectrum. To construct Figure 35, I merely divide the count rate by the telescope factor and the channel energy width, and plot the point at the midpoint energy. This figure shows three stages in the derivation of the spectrum: the raw count rates, the rates corrected for background, and the corrected rates taken only when the

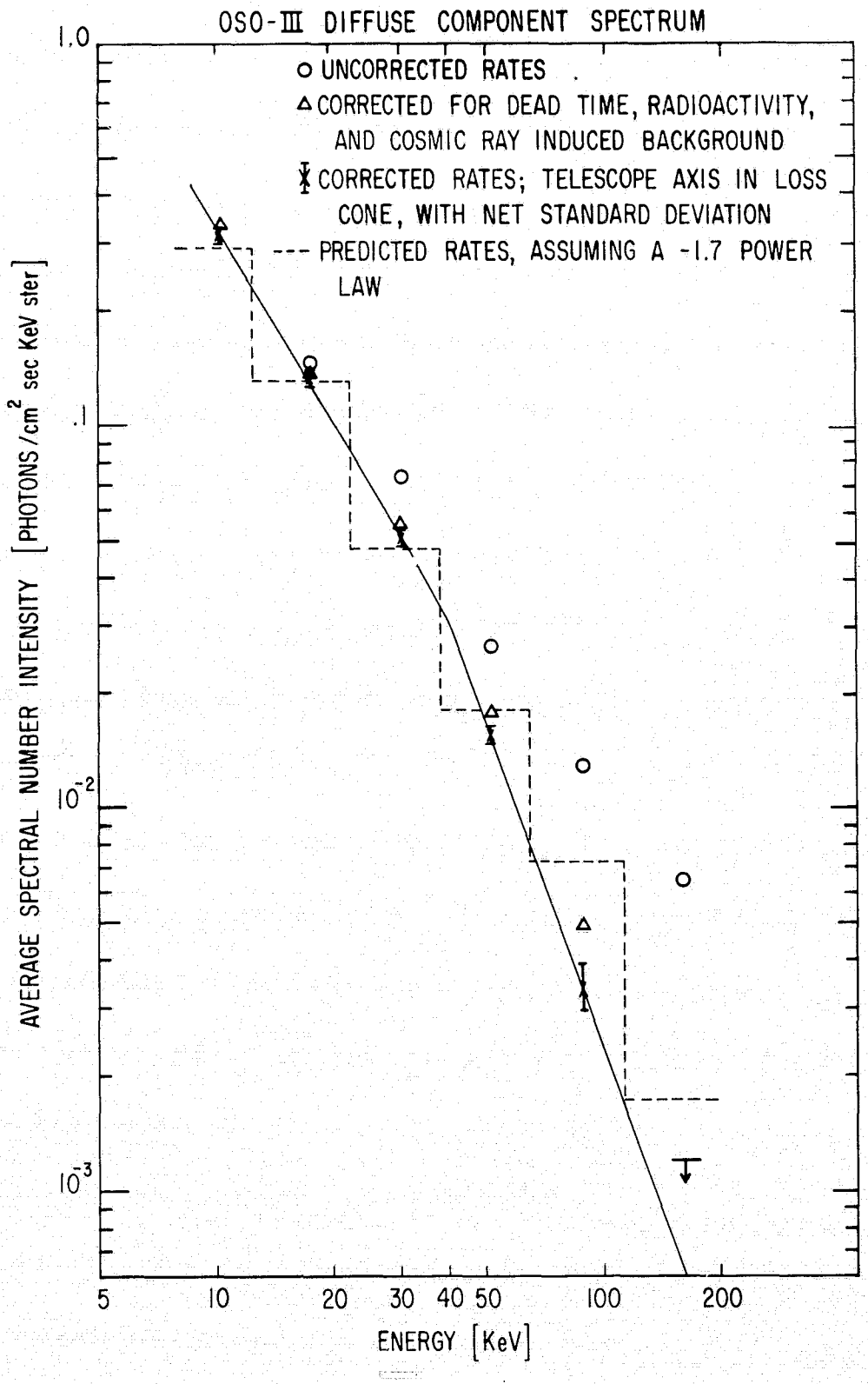

Fig. 35 Average spectral intensities measured on OSO-III, uncorrected for detector response. Error bars shown include estimates of errors in background corrections. No significant channel 7 count rate remains after background subtraction. The solid line represents the spectrum as a power law with a single discontinuity in the index.

telescope pointed within a local magnetic field line loss cone. More stringent criteria for selection of data do not produce any lower count rates. Channel 7 does not contain a significant flux after correcting for background; the upper limit corresponds to 99 percent confidence based on the standard deviation calculated as the square root of the sum of the variance due to the original total counts plus the estimated variance for the (approximately equal) calculated number of background counts. The error bars on the intensities include the uncertainty in background corrections. In the highest four channels the varying charged particle contamination becomes increasingly important. I estimate charged particle contamination by noting the difference in count rates compiled outside and inside the loss cone defined by the earth's magnetic field. The difference represents an upper limit to the average stable trapped electron intensity. I assume that the average stable precipitating electrons do not exceed the trapped intensity, to derive lower limits to the true diffuse X-ray intensity. Table 6 shows the number of counts used in constructing this spectrum, and the estimates of errors. The histogram in Figure 35 gives the predicted count rates due to a power law spectrum with number index 1.7. Such a flat index obviously cannot fit all the channels, but note that this steep an index already exceeds the best fit of channels 3 and 4. Thus a power law with a single index cannot represent the spectrum.

Figure 36 shows recent measurements of the diffuse component, which have suggested the presence of a "break." Rocket-borne experiments have usually led to a suggested break above their measured

Table 6

Diffuse Component Spectrum

Channel	2	3	4	5	6	7
Energy (keV)	7.7-12.5	12.5-22	22-38	38-65	65-113	113-210
All Data:						
Uncorrected Rate	2.001	1.845	1.589	.972	.841	.852
Corrected Counts	15594	26750	23790	16140	9234	-128
Rate (sec^{-1})	2.156	1.758	1.194	.645	.319	
Data in Loss Cone Only:						
Corrected Counts	6802	11190	9414	5803	2656	-1040
Rate (sec^{-1})	2.04	1.68	1.11	.569	.222	
Upper Limit to Contamination (sec^{-1})	.05	.08	.09	.076	.096	
Standard Deviations:						
From Raw Counts (sec^{-1})	.030	.016	.013	.009	.007	.008
From Radioactivity Correction (sec^{-1})	.013	.020	.015	.010	.014	.019
From Cosmic Ray Background Correction (sec^{-1})	.002	.006	.009	.014	.027	.062

Midpoint Energy (keV)	10.1	17.2	30.0	51.5	89.0	162
Net Average Intensity [Photons/(cm^2 sec keV ster)]	.315	.131	.0514	.0156	3.43×10^{-3}	$< 1.2 \times 10^{-3}$
Standard Deviation	.007	.002	.0010	.0005	$.48 \times 10^{-3}$	5.1×10^{-4}

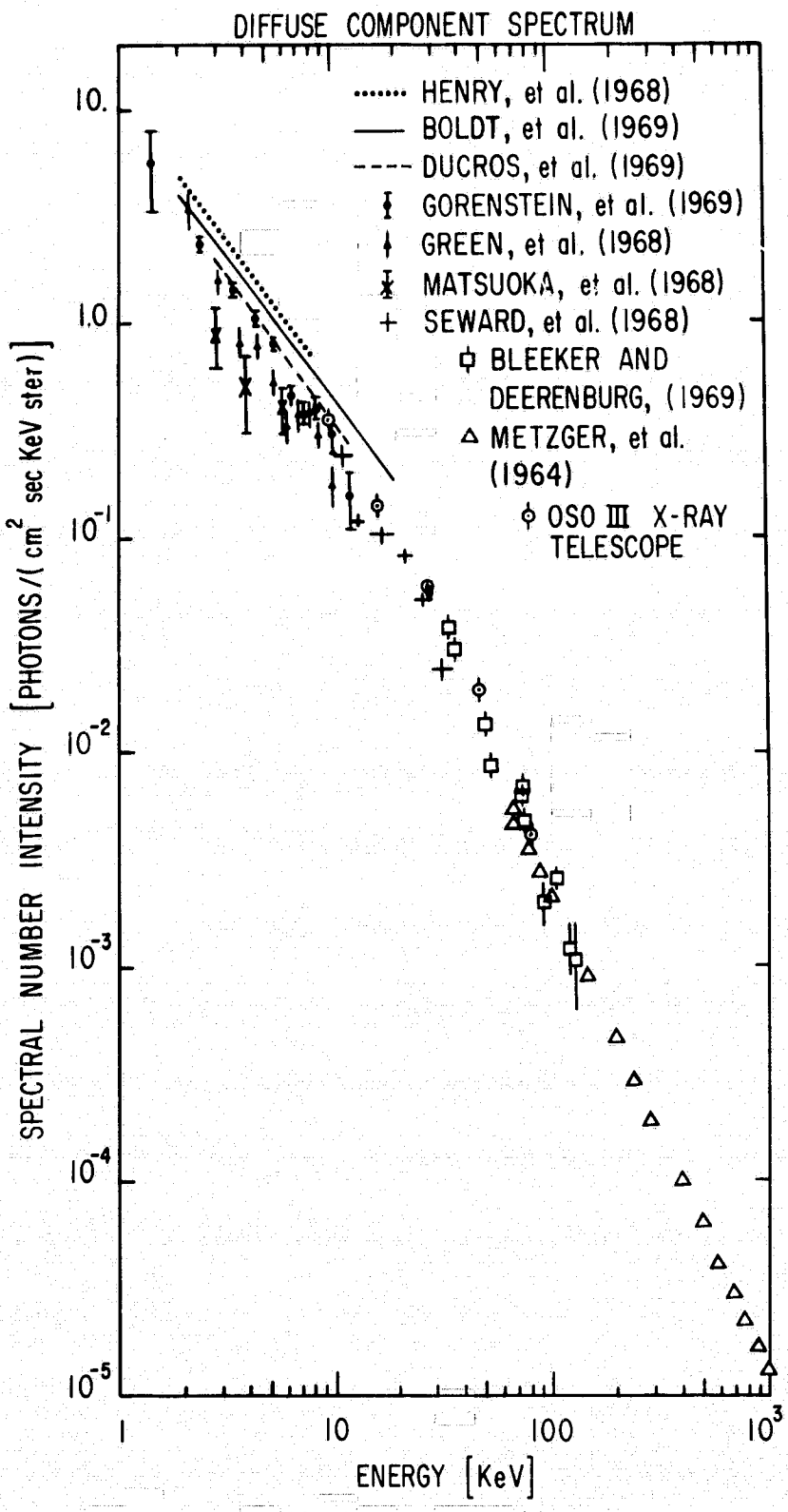

Fig. 36 Present results compared with other recent diffuse X-ray intensities between 1 and 1000 keV. (I have omitted a few points because of overcrowding.) The OSO-III points agree well with other measurements, but contradict some previously inferred spectral representations.

energy range, and balloon-borne experiments to a break below their measured energy range. If a single power law spectrum of electrons produces the X-rays, then a discontinuity in the X-ray spectral index implies a change in the electron power law index of twice the X-ray index change. On the other hand, the break may merely arise as a numerical artifact of the luminosity function of discrete sources.

I try to estimate the parameters K, m_1, E_B, and m_2 in the differential number spectrum

$$\frac{dN}{dE} = \begin{cases} KE^{-m_1} & E \leq E_B \\ KE_B^{m_2-m_1}E^{-m_2} & E \geq E_B \end{cases} \qquad (15)$$

(The straight lines drawn by hand in Figure 35 give K = 15.8, m_1 = 1.69, E_B = 42 keV, and m_2 = 3.09, but these do not contain any detector response corrections.)

If one wants a connection between the measured data and various physical parameters of the X-ray source, one needs some test of the data as a function of the parameter values as to how likely they represent the true values. The "chi-square" test provides a widely used criterion [Gorenstein, et al. (1968); Jacobson (1968)]. This test asks the probability of measuring a value of

$$\chi^2 = \Sigma \left(\frac{r_i - p_i}{\sigma_i}\right)^2$$

as large or larger than that arising from the experimental data r_i, for the predicted true rates p_i, which have variances σ_i^2. Calculation of the probability density function of χ^2 depends on the assumption that

each r_i has an independent normal distribution with mean p_i and variance σ_i^2 [Guest (1961)]. In the applications, r_i usually represents a sum of many counts or other independent data, so that the central limit theorem does predict a normal distribution. Not knowing σ_i exactly, thus provides the most serious obstacle for application of this test. Probability theory gives the variance due to a Poisson distribution of counts, but one can only estimate the contributions from systematic errors.

Because of the unknown error in the calculated response coefficients, I use the χ^2 test only to eliminate inconsistent values of the parameters rather than to select a "best" fit. I assume a 1 percent error in the calculated energy response, and reject sets $\{ m_1, m_2, E_B, K \}$ for which the measured χ^2 has less than a 2 percent probability of occurrence. The χ^2 test uses the north and south pole data in each energy channel independently, and thus has 6 degrees of freedom. I conclude that $32 \leq E_B \leq 44$, $0.6 \leq m_2 - m_1 \leq 1.5$, and $1.55 \leq m_1 \leq 1.75$. (Of course, E_B, m_1, and m_2 cannot vary independently within these ranges.) The normalization of the OSO-III points in Figure 36 uses parameter values giving a χ^2 in the middle of acceptable χ^2 values: $E_B = 36$ keV, $m_1 = 1.7$, $m_2 = 2.6$, and $K = 16.7$ photons $(\text{keV})^{.7}$ $(\text{cm}^2 \text{ sec ster})^{-1}$.

In the Felten and Morrison (1966) theory, equation (6), this X-ray spectrum would imply an electron spectrum of index $m = 2.4$, changing sharply at 3.4 GeV to an index $m = 4.2$ The normalization constant of equation (3), $K = 2.9 \times 10^{-15}$, and $K = 2.3 \times 10^{-11}$ electrons/$(\text{cm}^3 \text{ keV})$ below and above 3.4 GeV, respectively. The slope

4.2 exceeds the values derived from cosmic ray electron and from radio observations. I do not consider this serious because of the possible "overcorrection" of channel 6 (Figure 27), and because the X-ray energy range 7.7 to 110 keV corresponds roughly to an electron range of only 1.5 to 5.9 GeV. If the electron spectrum did continue up to 8000 GeV with slope 4.2, then equation (5) would require a magnetic field $H > 2 \times 10^{-3}$ gauss before the synchrotron mechanism could produce half the 10 keV X-rays.

The OSO-III measured intensities do agree well with most 1-100 keV results; however, several experimenters have fit their data from 1 to 10 keV to a spectral shape flatter than allowed by the OSO-III data. The satellite data analysis has revealed the presence of sporadic 10 keV albedo X-rays and of widespread electron precipitation, which contradict assumptions used in deriving true detector background for many earlier rocket-borne experiments. The ASE experiment which discriminated against charged particles [Gorenstein, et al. (1969)] gave a spectral index 1.7 ± 0.2 between 1 and 13 keV. Extrapolations of equation (15) fall below other measurements, predicting about 75 percent of the Wisconsin measurement at 0.25 keV [Bunner, et al. (1969)], and only 10 percent of the OSO-III 100 Mev measurement [Clark, et al. (1968)].

The accuracy of the present data justifies a more detailed calculation of the diffuse spectrum, especially to obtain a better understanding of the transition to the intensities measured outside the 10-100 keV range. Brecher and Morrison (1969) have performed such a calculation, assuming that the electron spectra of radio sources have

an intrinsic break, corresponding to observed breaks in the radio spectra. These authors conclude that such electron spectra will diffuse into intergalactic space at a sufficiently rapid rate to explain the measured X-ray intensity. Their calculated spectrum, based only on radio observations, agrees very well with the 5 OSO-III data points, and curves above the power law of equation (15) at low and high energies. Note that if the X-ray luminosity of normal galaxies does provide about 10 percent of the diffuse intensity, then the measurement or calculation of this component of the total spectrum becomes important for interpreting measurements having the accuracy obtained in this experiment.

For the purpose of this thesis, the spectral study establishes that, even considering the minimum of all previous measurements to give the diffuse X-ray intensity, most of the OSO-III counts in the five lowest channels do represent cosmic X-rays, and the study of at least the relative angular distribution can proceed with confidence. Also of importance, the channel 7 total count rate must contain at least 90 percent background, and thus the channel 7 map shows the limit to which background can cause apparent anisotropies.

B. Galactic Component of Diffuse X-rays

I search for a possible diffuse galactic component. Clark, et al. (1968) have reported a line source in the galactic plane above 100 Mev, and Cooke, et al. (1969) have reported a galactic plane component in the 2-16 keV range. In Figure 37 I plot the lowest three channels, sorted into bins 6° wide in galactic latitude. Because of the discrete source removal procedure, latitudes within 15° of the

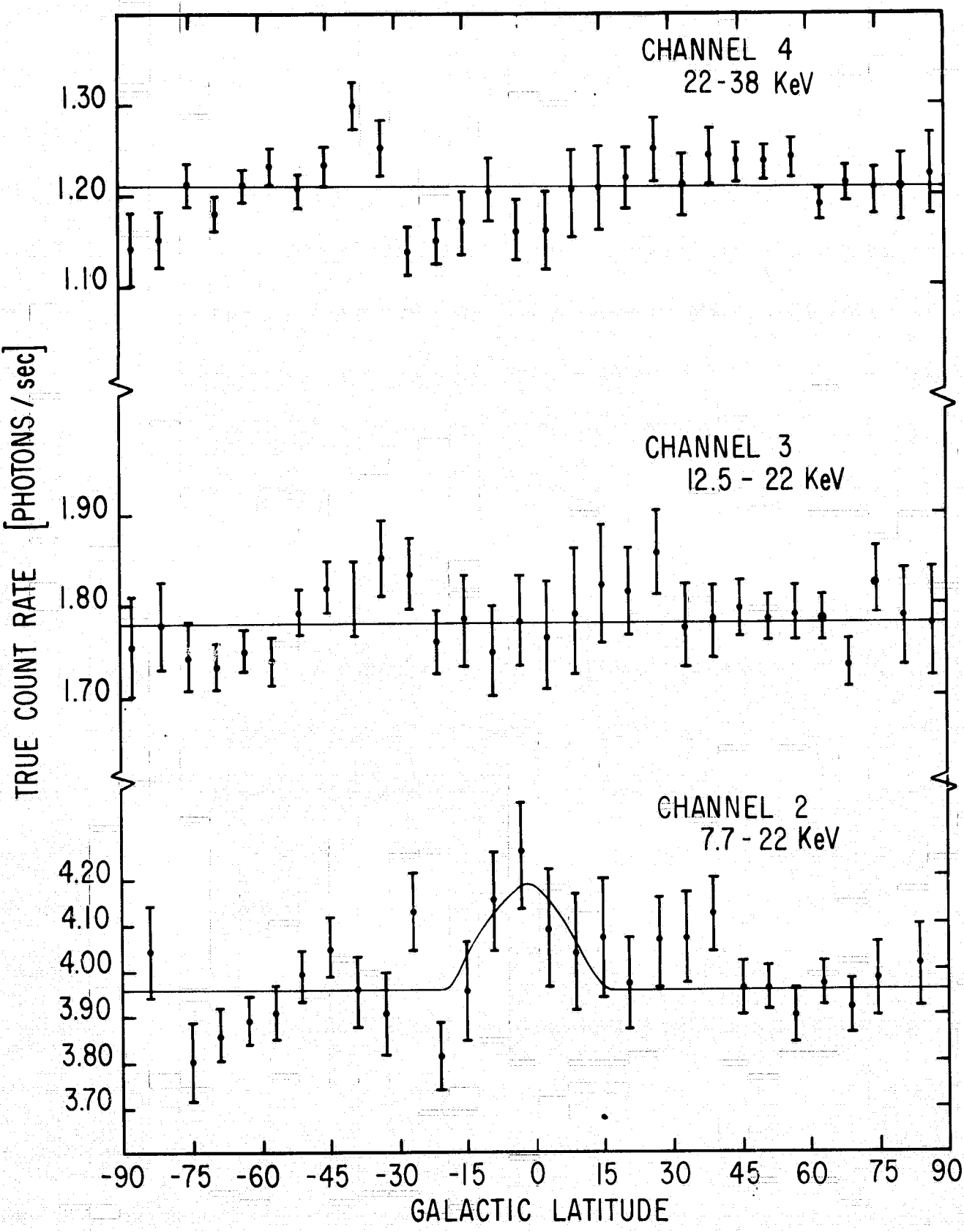

Fig. 37 Count rates sorted into 6°-wide galactic latitude bins. Points in channels 3 and 4 agree with the mean over the entire sky (solid line). The solid line for channel 2 equals the mean at the galactic poles plus a line source in the galactic plane.

galactic equator only contain galactic longitudes $\ell^{II} = 130^{\circ}$ to 160°, and $\ell^{II} = 220^{\circ}$ to 240°, with higher latitudes including a gradually wider longitude range.

Only channel 2 shows an excess associated with the galactic plane. The excess channel 2 count rate within $\pm 12^{\circ}$ of the plane equals 0.22 ± .06 counts per second. In the lowest four channels the areas around $\ell^{II} = 150^{\circ}$ and around $\ell^{II} = 230^{\circ}$ agree statistically; apparently about .08 counts/sec contamination increases the channel 6 and 7 count rates around 230° longitude. The expected associated channel 2 contamination would not exceed .016 counts/sec. I base the channel 6 limit only on the higher count rate data around 230°.

Figure 38 shows the OSO-III galactic plane limits (interpreted as a line source), together with the MIT (at $\ell^{II} = 240^{\circ}$) and Leicester points normalized to a -2 power law spectrum. The solid line represents the slope drawn by Cooke, et al. (1969). I also plot the upper limit points determined from the ERS-18 satellite measurement [Vette, et al. (1969)] by assuming that the entire excess of the ERS-18 count rate over the rate predicted by a power law extrapolation of the Ranger III [Metzger, et al. (1964)] .07 to 1 Mev data results from a uniform line source. A power law extrapolation of the 100 Mev data must have an index flatter than 1.7 to avoid conflict with the 10-100 keV limits. On the other hand, the flat spectrum measured at a few keV must break steeply at 10 keV. The ERS-18 data would represent an excess emission if galactic in origin.

As far as the OSO-III data can directly determine, the galactic component may merely represent a single discrete source in each region,

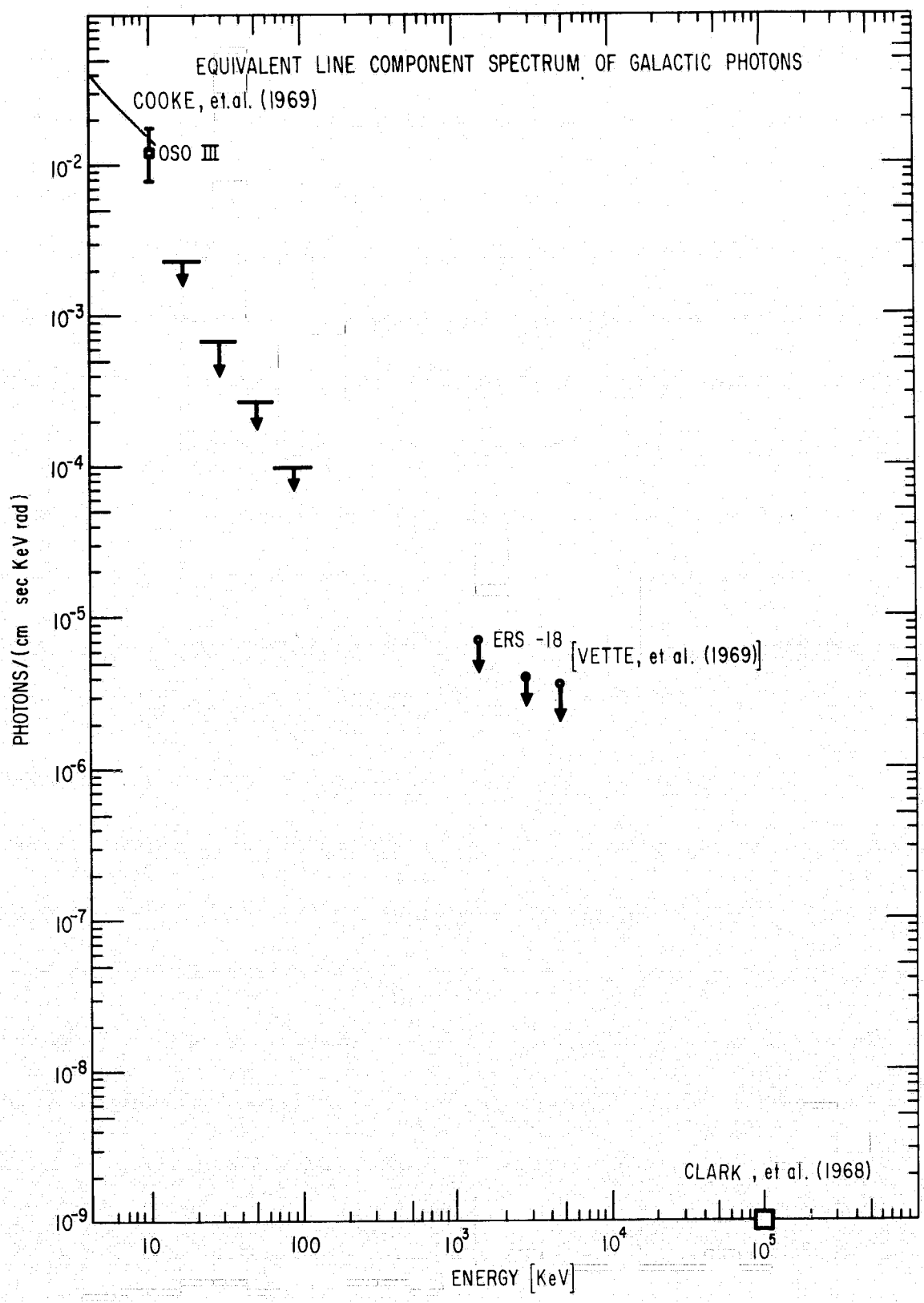

Fig. 38 Recent measurements and upper limits for galactic plane photons, interpreted as a continuous line source. Except for ERS-18, the measurements apply to galactic longitudes near 240°.

or several sources near the region each of which could contribute part of the count rate through the edges of the aperture. A 2π source of the measured channel 2 strength would imply a galactic luminosity at 10 keV of $J_{10} = 2 \times 10^{44}$ photons $(\text{keV sec})^{-1}$ assuming a crude mean distance 7 kpc to the emitting regions. This would contribute negligibly to a galactic luminosity of the order of the 3×10^{46} $(\text{keV sec})^{-1}$ extrapolated from the estimates of Gould and Burbidge (1963), Hayakawa, et al. (1966), and Friedman, et al. (1967), based on known discrete sources. We observe a peak emission about 5×10^{30} photons/(sec keV) at 10 keV from the sun, so all stars radiating constantly at the solar rate cannot explain the galactic sources. I now eliminate channel 2 data within 12° of the galactic plane from further analysis.

I search for a possible galactic halo component by a least squares fit of the form

$$C\,(\ell^{II},\ b^{II}) = A + B\,\frac{R(\ell^{II},\ b^{II})}{R(180^{\circ},\ 0^{\circ})} \qquad (16)$$

to determine values of A and B from the measured count rates C in a direction ℓ^{II}, b^{II} that looks through a distance R of the assumed galactic halo. I consider only spherical halos concentric with the galaxy, and do not find a significant value for B. The upper limits of Table 7 report twice the standard deviation of B, calculated by the least squares fit [Guest (1961)], divided by the previously determined average count rate at the galactic poles.

Table 7

Limits on Galactic Halo Emission

Halo Radius [kpc]	Upper Limit Percent Halo Emission in Galactic Anticenter Direction		
	Channel 2	Channel 3	Channel 4
12	0.3	0.3	0.4
16	0.8	0.8	0.9
20	1.3	1.4	1.5
24	1.8	2.0	2.1
28	2.4	2.5	2.7
32	2.9	3.2	3.3
36	3.5	3.8	4.0
40	4.0	4.4	4.6
44	4.5	5.0	5.2

C. The Angular Distribution of the Extragalactic Diffuse Component

I find no further angular variations. In Figure 39 I present a celestial coordinate map of the measured count rate in the 22-38 keV channel. I drew the contours from the rates in $6^{\circ} \times 6^{\circ}$ bins, as in Figures 28 to 33. The solid lines represent the number of standard deviations from the mean of all the data, and the dashed contours represent 10 percent measured variation from this mean. (These two kinds of contour do not coincide because of the different exposure times to various parts of the sky.) Galactic sources or lack of exposure exclude the regions outside the dotted lines. The telescope aperture retains approximately the constant size shown, throughout the map. No evident structure stands out from the statistical fluctuations. Photon statistics alone enter the standard deviation used here, thus I cannot consider even the two standard deviation contours as a real feature. Channel 4 provides the best map since discrete source contamination would affect the lower channels more, and electron contamination the higher channels. Considering this contamination, no features stand out in any of the energy channels.

1. Discrete Structure

I consider three possible physical causes of inhomogeneity in the diffuse X-ray data: statistical fluctuations in the angular density of discrete sources, considered as the source of the diffuse component; individual discrete sources, characterized by an excess emission with an arbitrary (but decreasing with energy) spectrum; and large scale inhomogeneities in the metagalaxy [Sachs and Wolfe (1967);

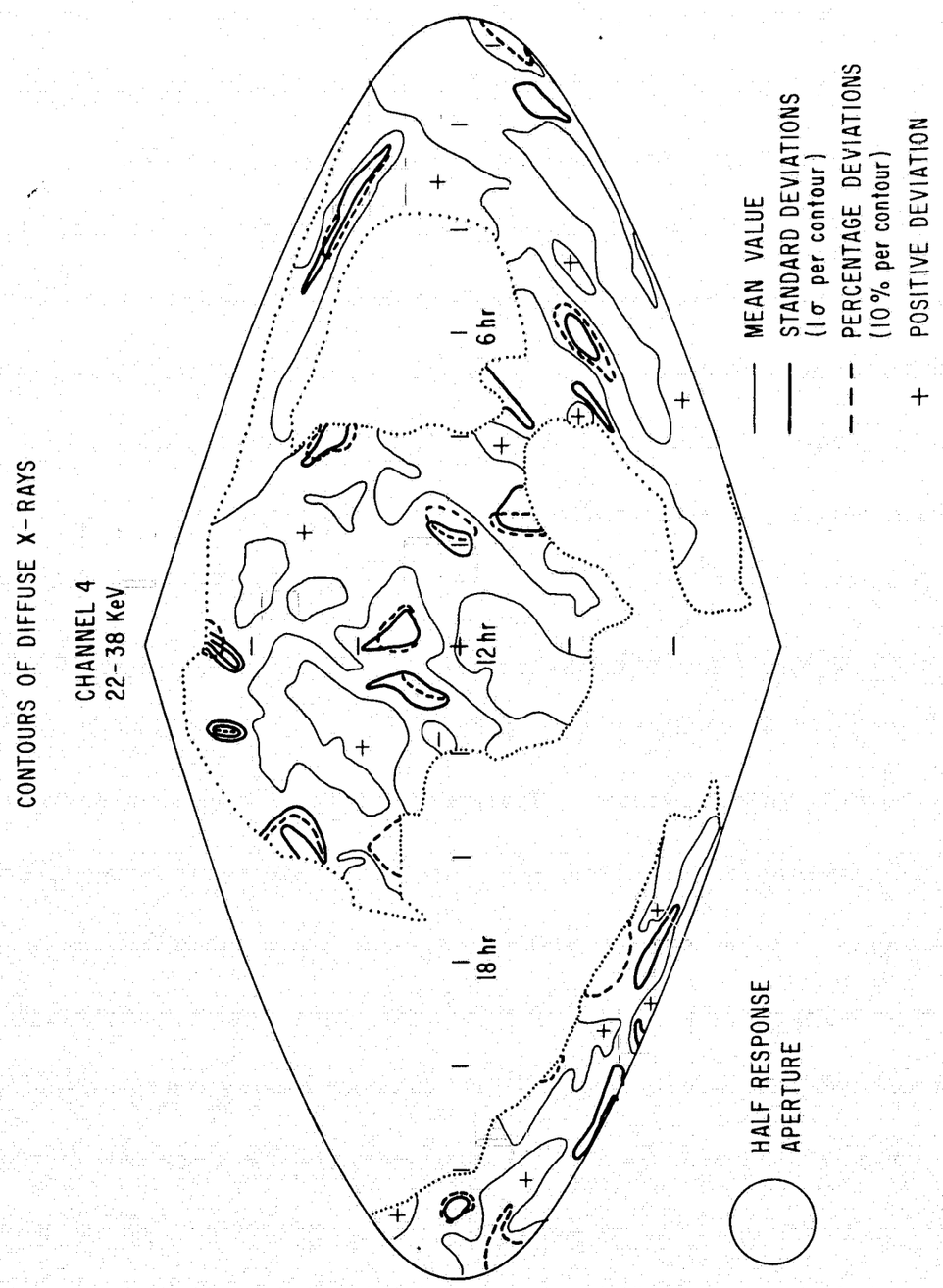

Fig. 39 The light solid lines represent contours of the mean count rate, 1.19 per second, in celestial coordinates. Plus signs mark areas of count rates greater than the mean (a heavy plus also marks the 12 hours, 0° declination point). Areas outside the dotted lines did not receive exposure free of galactic contamination.

Wolfe (1969)], characterized by either enhanced or decreased emission with about the same spectrum as the general diffuse component. To examine the diffuse component for lumpiness I sort the rates into exclusive square bins approximately 12° once, and then 20°, on a side. The exact size and shape of the bins differ by a few degrees because the discrete sources block out the sky in an irregular manner, and of course because squares cannot exactly map a spherical surface. One cannot treat the 12° bins as independent. I treat the 20° bins as independent because they have about the same area as the half maximum response circle. For further examination I require a bin to have at least 100 counts.

For the 12° bins I find the rate in 66 percent of the 186 channel 2 bins within one standard deviation (1σ, based on photon counting statistics only) of the overall mean, and 97 percent of the rates within 2σ. None exceed 2.6 deviations from the mean. For the 20° bins 55 percent of the 67 channel 2 bins fall within 1σ of the mean, 90 percent within 2σ, and none exceed 3 deviations. I assume that the deviations in channels 6 and 7 as large as 4σ or 5σ arise from particle contamination, and thus total events from channels 2 through 5 only in Figure 40. The X-ray statistical counting fluctuations can explain the distribution of rates.

Consider a model in which discrete sources with a Poisson distribution of average density N per steradian produce the observed diffuse intensity. The observed variance of count rates in the 400 square degree (.12 steradian) resolution elements provides a lower limit to N. The lowest N results from assuming all the discrete

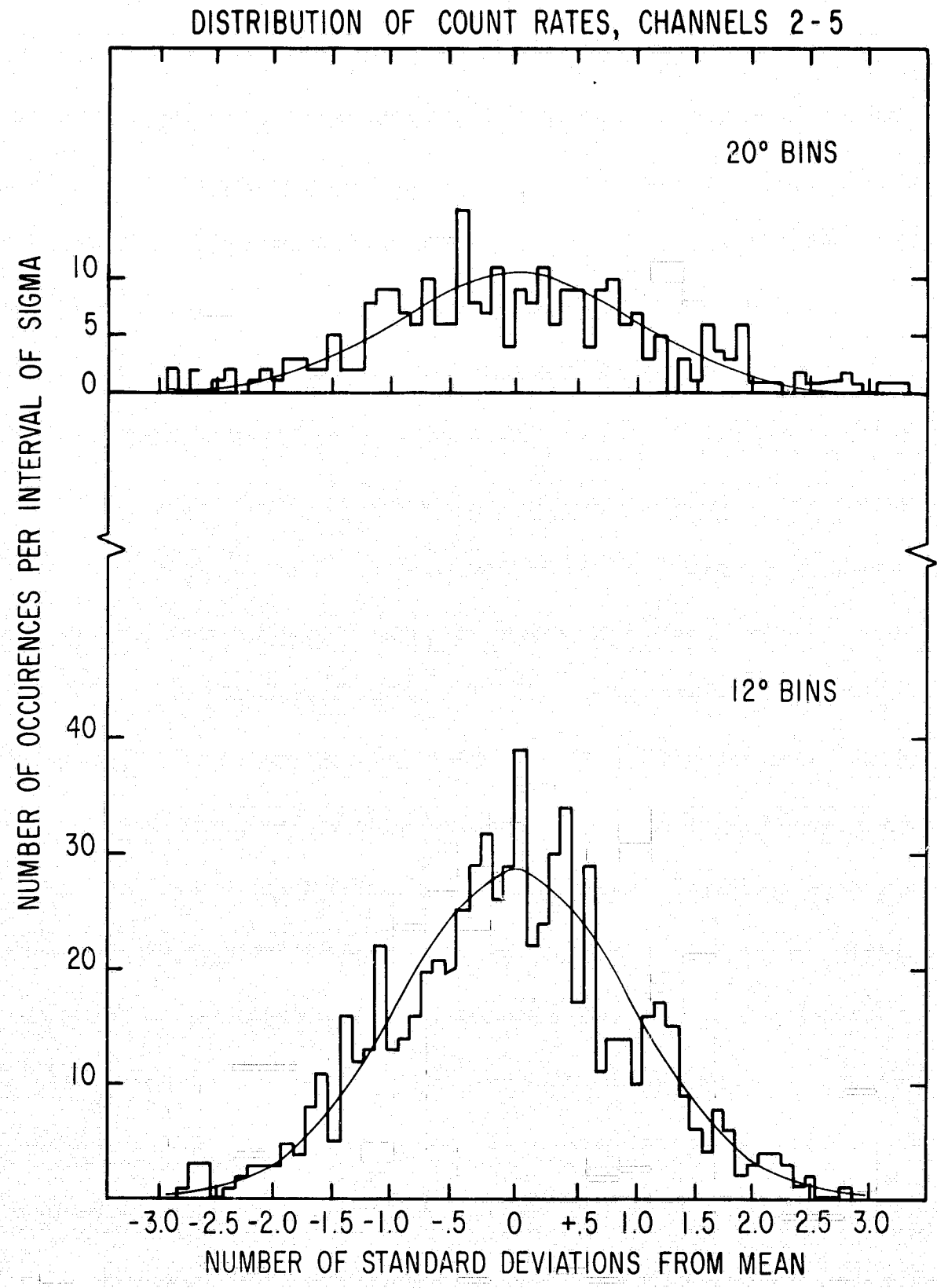

Fig. 40 The histograms show the number of occurrences of a standard deviation in a given 0.1σ interval. The smooth curves give the predicted numbers, considering only counting statistics to cause deviation from the mean.

sources have the same emissivity, ϵ_x photons per second, and same spectrum. Let λ equal the number of discrete sources in a single bin. For a fixed λ, the actual count rate observed in the bin will have a Poisson distribution with mean and variance $j_x \lambda$, where $j_x = \epsilon_x t$, and t = exposure time in the bin. Folding that distribution over the distribution of λ (mean and variance .12N) gives the estimates

$$n = j_x(.12N),\ S^2 = j_x(.12N)\ (j_x + 1) \qquad (17)$$

for the number and variance of counts observed in an arbitrary bin. The mean rate r_k in a given energy channel k gives the estimate $.12N\epsilon_x = r_k$. In equation (17) the term $j_x^2(.12N) = (r_k\ t)^2/(.12N)$ gives the variance due to the lumpiness of the discrete sources. Calculating the variance in each bin by adding a 3 percent spatial fluctuation results in a dispersion of the bin count rates narrower than predicted. Thus, $(.03) \geq 1/\sqrt{.12N}$, or $N > 9000$ per steradian.

The probability that the highest of M identical, independent measurements exceeds a value y, $P_M(y) = M\ p_y(1 - p_y)^{M-1}$, where p_y equals the probability that a single measurement exceeds y. The rate measurement differs somewhat from bin to bin because of different exposure time. I restrict attention to bins with greater than 400 counts to reduce this effect. I set $P_M(y) \leq F$ = degree of confidence, (there exists no more than a 100F percent a priori chance of measuring a value higher (or lower) than actually observed), and find the corresponding maximum p_y from binominal tables [Weintraub (1963)]. This maximum p_y implies a minimum number of standard deviations τ

$$p_y = \frac{1}{\sqrt{2\pi}} \int_\tau^\infty e^{-x^2} dx\ ,$$

by which the measured bin rate r must exceed the mean rate. The variance of rate equals S^2/t^2, therefore from equation (17)

$$\tau \leq \frac{|(r - r_k)|t}{j_x(.12N)(j_x + 1)}, \text{ or } N \geq \frac{r_k}{.12\left[\frac{(r - r_k)^2}{r_k \tau^2} - \frac{1}{t}\right]}.$$

To 99 percent confidence I find N > 5900 from the minimum rate in channel 4, and to 90 percent confidence N > 10,600 from the maximum channel 2 bin.

The bins do not really provide good data for discovering individual discrete sources, because the stringent requirements to minimize particle contamination only result in from 10^3 to 3×10^4 (cm^2 sec) exposure in a bin. Considering the fact that the background count rate increases with channel number, and that all known X-ray sources have a number spectrum which decreases at least as fast as the reciprocal of the energy, I only look for a positive excess in channel 2. I find none as great as three standard deviations, and set 95 percent confidence limits of from 2×10^{-2} photons/(cm^2 sec keV) at 10 keV for a source at $\ell^{II} = 234^\circ$, $b^{II} = 12^\circ$, down to 3×10^{-3} photons/(cm^2 sec keV) for a source at $\ell^{II} = 146^\circ$, $b^{II} = 60^\circ$. Of course, these limits do not apply to the blank areas in Figure 39.

I accumulate counts with the telescope axis within 7° of the Andromeda Nebula (M31), the HI maximum of each Magellanic Cloud [Bok (1967)], and M87. Comparing these rates with the rate at the galactic pole opposite to the given source does not give a significant flux, considering a possible low level particle contamination as well as the

photon counting statistics. Hudson, et al. (1969c) and Peterson (1969) have reported better upper limits on M87 than obtained here. Table 8 compares the upper limit (taking the larger of three standard deviations of the excess count rate, or two standard deviations plus a measured excess) fluxes and emissivities of M31 and the Magellanic Clouds with the emission required by equation (8) for normal galaxies to provide the measured diffuse intensity. Andromeda, with four times the galactic mass, falls just short of the required emissivity. The Magellanic Clouds emit at no more than one percent of the needed rate; however, they have only about one-tenth the mass of our galaxy, which in turn emits only at one-tenth the required average rate. Mark, et al. (1969) have made such conclusions from the finite few keV flux they measured from the Large Magellanic Cloud.

I search for a large scale inhomogeneity which might arise from spatial variation, either positive or negative, in the parameters ρ_o, T_o, $\bar{K}$ or R entering equation (7). As formulated in equation (6), the spectral shape would not change. A program averaged the percentage deviations from the mean of all data in three lowest energy channels, weighted inversely with the variance. Adding or subtracting two standard deviations from this 3-channel average gives an upper limit anomaly 18 percent above the mean for a 20° x 20° bin centered at $\ell^{II} = 64^\circ$, $b^{II} = 40^\circ$, and 20 percent below the mean at $\ell^{II} = 64^\circ$, $b^{II} = -40^\circ$. Statistics in about half the bins suffice to give an upper limit as low as plus or minus 4 percent deviations.

If one asks about larger anomalies, the errors become smaller. For example, the measured difference in channel 3 count rates compiled

Table 8

Limits on Extragalactic Sources

Energy	Emission Required to Explain Diffuse Component [photons/(sec keV)]	Upper Limit Flux (photons/cm^2 sec keV)			Maximum Emissivity (photons/sec keV)		
		M31	LMC	SMC	M31	LMC	SMC
7.7-12.5	3×10^{47}	.011	.013	.009	4.5×10^{47}	4×10^{45}	3×10^{45}
12.5-22	1.5×10^{47}	.0026	.0022	.0025	10^{47}	7×10^{44}	8×10^{44}
22-38	6×10^{46}	.0014	.0013	.0013	6×10^{46}	4×10^{44}	4×10^{44}
38-65	2×10^{46}	.0006	.0006	.0005	2.4×10^{46}	2×10^{44}	1.5×10^{44}
65-113	4×10^{45}	.0003	.0002	.0002	10^{46}	5×10^{43}	5×10^{43}

within 30° of the north and the south galactic poles equals 1.7 ± 1.1 percent, and within 60° of each pole $.6 \pm .8$ percent. I have not examined very large, arbitrarily irregular regions.

Ignoring the existence of discrete sources, this experiment still provides anisotropy limits slightly better than previously measured, and with the advantage of covering the entire sky. For example, Figure 31 shows no 50 percent variations outside the Crab, Cygnus, and Galactic center regions, and no 10 percent excess variations over most of the sky.

2. Continuous Structure

Given any prediction $F(\Theta,\varphi)$ of an angular structure, a weighted least squares fit of the count rate

$$C(\Theta,\varphi) = A+B\ F(\Theta,\varphi) \qquad (18)$$

makes use of all the data to calculate A and B. The computational procedure gives an unbiased estimate of the variance and covariance of A and B [Guest (1961)]. Basically, I consider all the results consistent with isotropy; the data allows B = 0 for any function F. I thus want to set an upper limit on B. If the calculated A and B give the correct average rate over the whole sky, and if $2\sqrt{\text{varB}} \geq B$, I merely report $\frac{2\sqrt{\text{varB}}}{A}$ as the upper limit fractional variation (I normalize F to make it dimensionless). Otherwise, I try a χ^2 test and define an "allowed" value of B as the one percent possibility level. I group large numbers of counts together for such tests, so that the resulting 25 to 75 degrees of freedom do represent independent measurements. With B = 0, an χ^2 test occasionally reports less than one

percent probability of consistency between the measured data and isotropy for a single energy channel. I attribute this to charged particle, or perhaps discrete source, contamination and make no conclusion for the associated B value. In general, I consider the three lowest energy channels separately, and take the lowest B value from them.

DeVaucouleurs' (1953, 1958) model of the local supercluster pictures the galaxy on a 15 Mpc semimajor axis, 11 Mpc from the center of an oblate spheroid with semi-minor axis 3 Mpc. I let F equal the fraction of the minimum possible distance from the galaxy to the spheroid surface. I find a limit to B of 1.4, 1.5, and 2.0 percent in the three lowest channels. These channels each give a 95 percent confidence limit of 1.4 percent for a supergalactic plane component.

The least speculative source of variation would arise from the motion of the earth with a velocity $v = \beta c$ relative to a frame in which an observer would measure an exactly isotropic intensity I_o. If this intensity has a power law number spectrum

$$I_o(E) = KE^{-n} \text{ [photons/(cm}^2 \text{ sec keV ster)]}$$

then for $\beta \ll 1$, the observed differential number intensity

$$I(E) = KE^{-n} [1 + (2+n) \beta \cos \Theta] \qquad (19)$$

with Θ the angle between $\vec{v}$ and the direction of observing I(E) [Compton and Getting (1935); Gleeson and Axford (1968)]. An analysis program takes a grid of trial directions spaced about 12° apart. The least squares fit, or the direct average of B calculated by letting A equal the mean for the entire sky, gives limits of about one percent, or

since n = 1.7, a velocity of 800 km/sec. This limit applies to the resultant velocity in any direction, because of the large sky area covered by the telescope. A χ^2 fit of the cosθ amplitude to counts sorted in 30, 6°-wide bins gives a limit of about 600 km/sec to 90 percent confidence. The 3° microwave measurements have far greater relative accuracy, about .1 percent, but for the blackbody number spectrum n = -1 in equation (19), and also the radio experiments which only scan a declination circle cannot give the velocity component perpendicular to that plane.

Differential expansion of the universe along one axis would result in one plane of symmetry, and two perpendicular planes with a maximum amplitude 12-hour component. I fit the difference between count rate measured in any direction and the mean over the sky to A cos(2ω + B) for counts within 30° of the equator (ω = longitude) of an array of poles spaced 12° apart. I disregard directions in which the equator has gaps of 24° or more (due to areas blocked out by discrete sources). I find an upper limit amplitude of about 5 percent. (Use Figure 39 to see for which great circles this limit applies.) Again, although individual microwave measurements have given limits an order of magnitude more sensitive, the present results apply more widely on the celestial sphere. The X-ray results also have importance since a given physical anisotropy need not produce the same 12-hour amplitude in 10^{-3} ev photons as in the 10^4 ev photons.

Consider a crude model in which the distance R, in equation (7), lies on the surface of a spheroid, with semiaxes a, a, and b. I assume trial directions for b and compare the average within 30° of the poles

with the average within 30° of the equator. For most trial poles I find $.97 \leq \frac{b}{a} \leq 1.03$, which corresponds to an eccentricity $\epsilon \leq .02$.

D. Summary

The first satellite cosmic X-ray telescope, an instrument far surpassed by current balloon-borne experiments, has provided significant information on the diffuse component of cosmic X-rays. Results discussed in this thesis include:

1) accurate intensity measurements in five energy channels between 10 and 100 keV, establishing a spectral break;
2) upper limits to an extended galactic plane component, and a measurement at 10 keV if such a component proves real;
3) upper limits of about two percent to the fraction of the diffuse component emitted by a galactic halo, or from the local supercluster;
4) upper limits of about 800 km/sec for the resultant velocity of the earth in any direction relative to a frame in which the diffuse X-rays appear isotropic;
5) upper limits in some detail for possible inhomogenities in different parts of about half the sky;
6) with the assumption that the diffuse component arises as the integrated effect of discrete sources, a lower limit of 10^5 for the total number of such

sources;

7) an upper limit to the flux from M31 just at the level required for the emissivity of normal galaxies to explain the diffuse component;

8) an upper limit of five percent for the amplitude of a 12-hour component on some great circles, or of two percent eccentricity for a crude model with the Earth as the center of an ellipsoidal universe.

The mechanism of X-ray production does not enter the derivation of these results. The broad resolution of the detector also makes the results (except item 6) independent of whether the diffuse component arises from discrete sources, or continuously throughout intergalactic space.

The OSO-III satellite operation also provides the design requirements necessary to greatly improve a future OSO diffuse X-ray experiment. One must directly detect and reject charged particles, and reduce and directly monitor the gamma ray background due to induced radioactivity of Na^{24}. This thesis based most of its conclusions on 341,700 extragalactic X-ray counts. Yet during the one year of data used, some 1.5×10^{8} diffuse X-rays between 7.7 and 110 keV actually interacted in the central detector. The higher bit rate currently available on OSO satellites, and a better measurement of the telescope position on the wheel plane to reduce the large zones of avoidance around the earth and discrete sources, would increase the data retrieval a factor of 10. Experimentally, at least, diffuse X-rays can fulfill the hope of Morrison (1967) to provide, ". . . one of the most fruitful channels of data about the largest scales of the universe, . . ."

APPENDIX A

ANALYSIS OF AN OSO-III WHEEL EXPERIMENT

1. Orbit Calculation

Six constants, any independent functions of the three components of initial position and initial velocity, specify the solution for the motion of a point object in a given potential field. The Kepler ellipse solution for motion in the field of a sphere motivates the constants, called orbit parameters, generally used in describing the motion of satellites in the Earth's gravitational field. The orbit parameters a (semi-major axis), ϵ (eccentricity), i (inclination of the orbital plane), Ω (right ascension of ascending node), and ω (argument of perigee) specify the shape and orientation of the ellipse at an arbitrary time T_o (time of epoch). The satellite moves around this ellipse with angular frequency

$$n_o = \sqrt{GM/a^3} \quad \text{(radians per second)}, \tag{20}$$

with G the universal gravitation constant and M the mass of the earth. For the sixth parameter I use σ (mean anomaly), the angle on the ellipse from perigee to the satellite at time of epoch. Following the treatment of Escobal (1965), define the true anomaly v as the angle at the center of the sphere from perigee to the satellite position on the ellipse, and eccentric anomaly E as the angle from perigee to the projection perpendicular to line of perigee of the satellite position onto the circumscribing circle (Figure 41). The equations

ANGLES USED FOR ORBIT CALCULATION

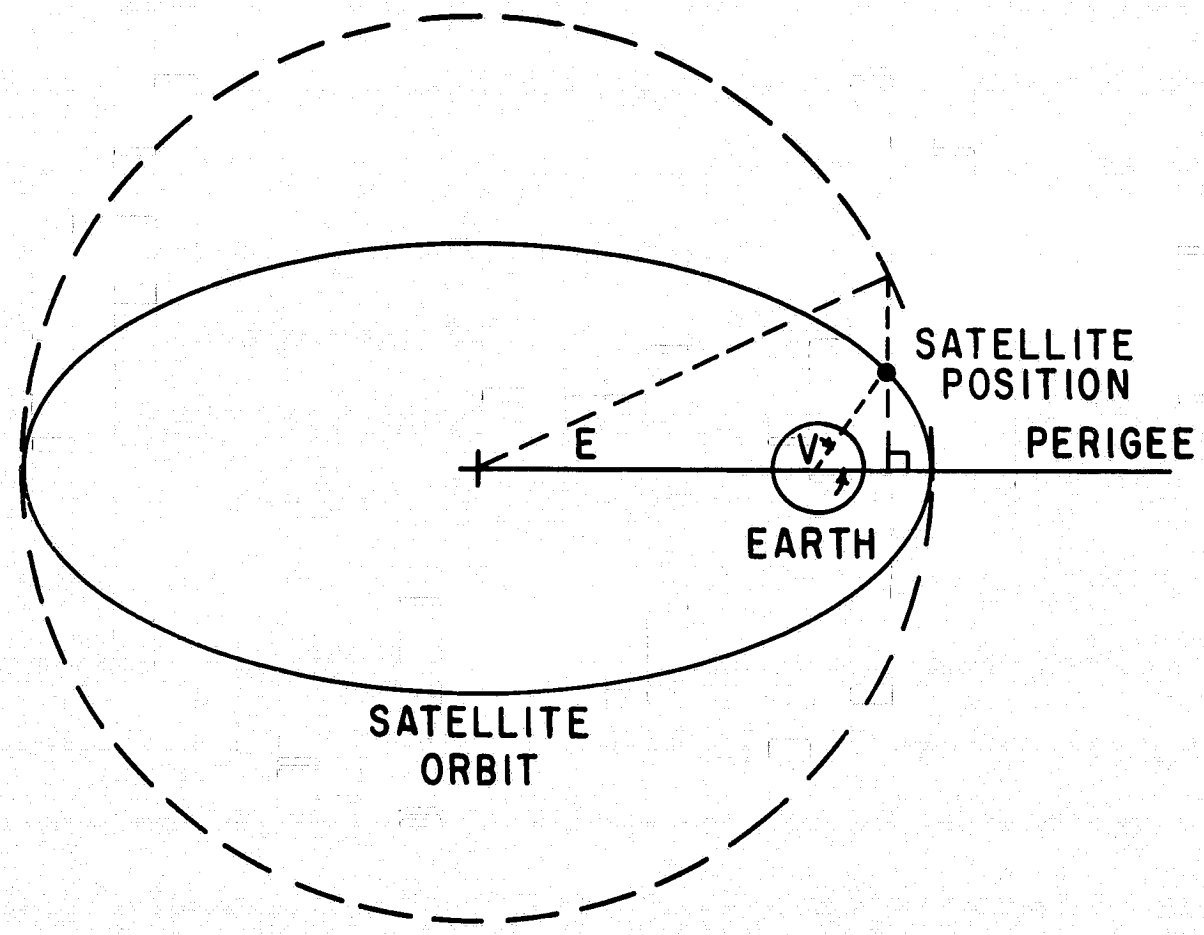

Fig. 41 Definition of the true anomaly v and the eccentric anomaly E, for the instantaneously elliptical orbit.

$$\tan v = \frac{\sqrt{1-\epsilon^2}\,\sin E}{\cos E - \epsilon}\,, \tag{21}$$

$$E - \epsilon \sin E = n_o(t-t_o) + \sigma \tag{22}$$

parametrically determine the position of the particle on the ellipse at time t. Then the distance from the center of the earth

$$r = \frac{a(1+\epsilon^2)}{1+\epsilon \cos v}\,, \tag{23}$$

the latitude $\Theta = \arcsin [\sin i \sin(v + \omega)]$, (24)

and the right ascension $\alpha = \Omega + \arctan [\cos i \tan(v + \omega)]$. (25)

Expand the potential of the azimuthally symmetric earth:

$$V(r,\Theta) = -\frac{GM}{r}\left(1 + \sum_{n=2}^{\infty} J_n \frac{P_n(\sin\Theta)}{r^n}\right),$$

with r in units of earth radii a_e. Kozai (1964) used $GM = 3.986032 \times 10^{20}$ cm^3/sec^2, $a_e = 6378.165$ km, and obtained J_n to n = 14 by least squares fit to observations of the motion of nine satellites. He reported as the best solution:

$$J_2 = (1082.645 \pm .006) \times 10^{-6}$$

$$J_3 = (-2.546 \pm .020) \times 10^{-6}$$

$$J_4 = (-1.649 \pm .016) \times 10^{-6}$$

$$J_5 = (-0.210 \pm .025) \times 10^{-6}$$

$$J_6 = (0.646 \pm .030) \times 10^{-6}.$$

The Kepler ellipse approximates the orbit because

$$1 \gg J_2 \gg J_2^2 \cong J_3 \cong J_4 .$$

Many authors [Brouwer (1959); Kozai (1959); Garfinkel (1959); Escobal (1965)] have used perturbation theory to calculate the effects of the J_2, J_3, and J_4 terms. In this theory the orbit parameters still specify a Kepler ellipse solution at any time, but the parameters vary in time linearly (secular terms), periodically with v (short period terms), and periodically with ω (long period terms). The parameters a, ϵ, and i have no secular variation. For these I use the values given by the Goddard Space Flight Center predicted world map which the flight operations group calculates about a week in advance based on all previous observations of the satellite. To order J_2, Escobal (1965) gives the formulas

$$\sigma = \sigma_o + \dot{\sigma}\, t,$$

$$\omega = \omega_o + \dot{\omega}\, t,$$

and

$$\Omega = \Omega_o + \dot{\Omega}\, t, \qquad (26)$$

where

$$\dot{\sigma} = 3/2\, J_2 \frac{n_o \sqrt{1-\epsilon^2}}{a^2(1-\epsilon^2)^2} (1 - 3/2 \sin^2 i)$$

$$\dot{\omega} = 3/2\, J_2 \frac{n_o}{a^2(1-\epsilon^2)^2} (2 - 5/2 \sin^2 i)$$

$$\dot{\Omega} = - 3/2 \frac{J_2\, n_o \cos i}{a^2 (1-\epsilon^2)^2} .$$

For the OSO-III orbit $a \cong 1.087$, $\epsilon \cong 0.0022$, $i \cong 33^{\circ}$ so $\dot{\sigma} \cong 0.3$, $\dot{\omega} \cong 0.6$, and $\dot{\Omega} \cong -0.4$, in degrees per orbital period. The presence of ϵ as a factor allows the neglect of other first order perturbation terms for the nearly circular orbit. Because of the nearly circular orbit I can solve equations (21) and (22) by

$$E = \ell + \epsilon \sin \ell + \frac{\epsilon^2 \sin 2\ell}{2} + O(\epsilon^3)$$

$$v = E + \epsilon \sin E + \frac{\epsilon^2}{4} \sin 2E + O(\epsilon^3)$$

$$= \ell + 2\epsilon \sin \ell + 5/4\ \epsilon^2 \sin (2\ell) + O(\epsilon^3)$$

where

$$\ell = n_o\ t + \sigma\ .$$

The predicted world maps supplied by Goddard Space Flight Center give satellite latitude, longitude, and altitude at every minute U.T. I use equations (23), (24), and (25) to update σ, ω, and Ω once each orbit. For convenience I take the time of northbound equator crossing, so the altitude gives σ via equation (23), $\Theta = 0$ gives $\omega_o = -v$ in equation (24), and converting the world map long tude λ into right ascension gives Ω_o. By definition $\Omega_o = \alpha = S + T\ (1.00273791) + \lambda$, where S equals the angle from the first point of Aries to the 0^h UT line (called mean sidereal time at 0^h UT) and depends on the day of year, λ equals the geographic longitude in hours east of Greenwich, and the numerical factor converts universal time UT into sidereal time.

I calculate ω and Ω according to equation (26). Ignoring $\dot{\sigma}$ has no significant effect on the accuracy. Instead of calculating n_o from equation (20) above, the computer program uses a period determined by averaging the times between a northbound equator crossing and the next arrival at the same right ascension. These periods differ by less than nine seconds so the true anomaly error $dv = tdn_o = t\frac{dT}{T^2} \leq \frac{9}{5739} < .0016$ radian, a negligible angular difference even for an entire pass.

The accuracy with which one can determine the Earth's magnetic field as a function of position in space, and the spatial rate of change of the magnetic field vector, define the accuracy requirements for the orbit calculation. For magnetic field calculations I use the INVAR package of routines by A. Hassitt and C. E. McIlwain (1966). These routines give the magnetic field direction to an accuracy of 1^o. I have the orbit calculated by the data reduction spot checked against predicted world maps and find the differences $< 1^o$ longitude, $< \frac{1}{2}^o$ latitude, and < 20 km altitude in magnitude. I ran a series of test programs about a grid of positions every 30^o longitude, every 10^o latitude between -30, and $+30^o$, and at 550 km altitude. I varied one of the spherical coordinates in each program: the altitude by 10 km between 530 and 570, the latitude by 0.5^o between $+1^o$ and -1^o from the central value, and the longitude by 1^o between $+2^o$ and -2^o from the central value. I found that the orbital uncertainty led to maximum changes of the magnetic field direction from the direction at the grid position of 1.2^o and maximum changes of 1 percent in the magnetic field magnitude and $\frac{1}{2}$ percent in the McIlwain L parameter.

I consider a count of celestial origin only when the aspect solution puts the center of the telescope at least 20° from the edge of the solid Earth. Thus a 1° error in the position of the Earth still cannot give a .1 cm^2 exposure to albedo X-rays.

2. Aspect Solution

The reduction routines must know the direction in which the telescope points at any time. The solution and terminology used here follow a draft of the BBRC aspect reference manual (1964) which I have revised and corrected as necessary. I assume a constant spin axis position for an entire orbit. The spin axis direction actually changes slowly, about 1° per day as the wheel plane follows the sun around the sky. At any universal time t, I can calculate the angle Θ in the wheel plane by

$$\Theta = \omega (t - t_o) + \Theta_o \qquad (27)$$

with ω the known, constant (for the usable data) OSO-III spin frequency. A spacecraft function measures the time t_o when the instrument points at the reference angle Θ_o. A spacecraft sun pulse generated by a solar sensor rotating with the wheel provides the reference during orbit day. At night a magnetometer pulse generated by the increasing null of the earth's magnetic field provides a reference, which the 99 coefficient Hendricks and Cain (1966) model of the earth's magnetic field connects to an angle fixed in space. BBRC (1966) measured $\Theta_o = 18.02^{\circ}$ for the angle between the spacecraft sun sensor and the UCSD optical axis, and $\Theta_o = 89.19^{\circ}$ for the angle between the magnetometer reference and UCSD optical axis. The final orbit tapes provided by GSFC give the universal

time of telemetry words. A scaler then determines t_o in universal time within 2.5 ms by counting the number of 400 cps clock pulses between the first word of each DSM frame and the next reference pulse.

An analogue spin monitor provides a rough spin rate, to about 1 percent. During orbit day the wheel analogue subcommutator contains the state of a 32-step counter advanced by each revolution past the sun. We determine this rate from the listing of the quick-look main frame data, in advance of the reduction runs. This gave us day spin periods of 1.55 to 1.62 seconds between March, 1967, and May, 1968. During orbit night the sail structure rotates with the wheel, increasing the moment of inertia and therefore the spin period by a factor of 1.13. In the data reduction programs, knowing the spin period T within a few percent, we can use the data determining t_o in equation (27) to give a highly accurate spin rate every 25.6 seconds. Let t_1 and t_2 (measured to 2.5 ms) equal the times from the start of successive DSM frames to the next reference pulses. Then in $25.600 + t_2 - t_1$ seconds the wheel has made $N = N'$ = greatest integer in $(25.6/T)$ revolutions, if $t_2 < t_1$, or $N = N' + 1$ revolutions if $t_2 > t_1$. At night the wheel has made $N + \frac{\Delta\theta}{360}$ revolutions with $\Delta\theta$ the change of magnetic null direction in the wheel plane during the time from t_1 to t_2. This change may vary from 0° to 7°, but usually $\Delta\theta \cong 1^\circ$. The period

$$T = \frac{25.600 + t_2 - t_1}{\text{number of revolutions}} .$$

The relative time error

$$E_t \cong \frac{(.025)/2}{25.6} \cong 10^{-4},$$

and the relative error in the number of revolutions

$$E_N \cong \frac{1^\circ/360^\circ}{14} = \frac{1}{5000} = 2\text{x}10^{-4} \text{ at night}$$

due to error in magnetic field direction, and less than

$$\frac{(1/8)^\circ}{360^\circ} \; / \; 16 = \frac{1}{45000} = 0.2\text{x}10^{-4}$$

due to error in triggering the solar sensor during day. Thus the relative rms error in the period,

$$E_T \leq .01 \text{ to } .03 \text{ percent.}$$

When the satellite enters the sunlit portion of the orbit, torque motors lock the sail structure to the sun and within about 90 seconds the wheel plane spins up to a stable day period. At night the motors merely stop servoing the sail, which gradually spins up due to friction in the bearings. Thus it requires about six minutes for the wheel to spin down to a stable night period. I do not analyze direction counts while the spin rate changes.

I calculate the direction of the spin axis in the "ecliptic" coordinate system. These cartesian axes originate in the spacecraft, with x_e-axis pointing toward the sun, z_e-axis pointing north perpendicular to the earth's orbital plane (ecliptic plane), and $\hat{y}_e = \hat{z}_e \times \hat{x}_e$. One obtains the transformation to celestial coordinates by a rotation about $\hat{z}_e$ through minus the angle S of the sun in the ecliptic plane

past the line of Aries, a known function of time, and then about the new $\hat{x}$-axis through minus the inclination $\epsilon = 23.45^{\circ}$ of the ecliptic plane to the equator. One obtains the "spacecraft system" from the ecliptic system by a rotation about $\hat{x}_e$ of φ, called the roll angle, followed by a rotation about $\hat{y}_s$ of η, called the pitch angle.

Thus the pitch angle equals the angle between the said plane and a plane perpendicular to the solar direction, positive when the actual sail structure tilts away from the sun. One calculates pitch angle by the measured difference in output of a pair of solar cells which receive different amounts of sunlight as the sail is tilted out of the $\hat{y}_e$ - $\hat{z}_e$ plane. The spacecraft logic digitizes the voltage range corresponding to $\pm 5.2^{\circ}$ into 256 steps, and telemeters a reading once every 30.72 analogue subcommutator period. The flight operations group at GSFC energizes a magnetic torque coil by ground command into one of three states depending on the average orientation of the spacecraft and earth's magnetic field over a period of the order of two weeks. When necessary they command a gas jet in the arms to fire, so that the magnitude of the pitch angle remains less than 3°. BBRC (1964) reported errors in the pitch angle determination of less than $.15^{\circ}$ due to the analogue to digital conversion, plus possible long term change in sensor gain causing systematic error of 5 to 10 percent of the pitch angle.

I use the known sun and calculated magnetic field directions, and the measured angle Θ_m in the wheel plane between the magnetometer increasing null and the sun pulse, to determine the roll angle. During orbit day, the number N_c of 400 cps clock pulses from a rising zero

crossing to the next sun pulse measures θ_m through $\theta_m = \frac{2\pi}{T}\frac{N_c}{400} + \theta_o$, with T the known spin period and θ_o the fixed angle in the wheel between the magnetometer and the sun sensor. BBRC (1966) measured $\theta_o = 71.17^o$.

Let the magnetic rising null vector have components $\vec{N} = (n_1, n_2, 0)_s$ in the spacecraft coordinate system. Then $n_1 = \cos\theta_m$ and $n_2 = -\sin\theta_m$ (θ_m measured positive from $\vec{N}$ to $\hat{x}_s$). From the definition, one obtains the components of a vector in spacecraft coordinates from the components in ecliptic coordinates by matrix multiplication by PR where

$$R = \begin{Bmatrix} 1 & 0 & 0 \\ 0 & \cos\varphi & \sin\varphi \\ 0 & -\sin\varphi & \cos\varphi \end{Bmatrix}$$

and

$$P = \begin{Bmatrix} \cos\eta & 0 & -\sin\eta \\ 0 & 1 & 0 \\ \sin\eta & 0 & \cos\eta \end{Bmatrix}.$$

Thus the components of $\vec{N}$ in ecliptic coordinates:

$$\vec{N} = R^{-1} P^{-1} \begin{Bmatrix} n_1 \\ n_2 \\ 0 \end{Bmatrix} = \begin{Bmatrix} \cos\eta & 0 & \sin\eta \\ \sin\eta\cos\varphi & \cos\varphi & -\cos\eta\sin\varphi \\ -\sin\eta\cos\varphi & \sin\varphi & \cos\eta\cos\varphi \end{Bmatrix} \begin{Bmatrix} \cos\theta_m \\ -\sin\theta_m \\ 0 \end{Bmatrix}$$

$$= \begin{Bmatrix} \cos\theta_m\cos\eta \\ \cos\theta_m\sin\eta\sin\varphi - \sin\theta_m\cos\varphi \\ -\cos\theta_m\sin\eta\cos\varphi - \sin\theta_m\sin\varphi \end{Bmatrix}.$$

If $\vec{H}$ represents the magnetic field vector in ecliptic coordinates, $\vec{H} \cdot \vec{N} = 0$ gives an equation for φ:

$$0 = h_1 \cos\theta_m \cos\eta + h_2 (\cos\theta_m \sin\eta \sin\varphi - \sin\theta_m \cos\varphi)$$

$$+ h_3 (-\cos\theta_m \sin\eta \cos\varphi - \sin\theta_m \sin\varphi) =$$

$$\sin\varphi (h_2 \cos\theta_m \sin\eta - h_3 \sin\theta_m) + \cos\varphi (-h_3 \cos\theta_m \sin\eta - h_2 \sin\theta_m)$$

$$+ h_1 \cos\theta_m \cos\eta,$$

or $$C = A \sin\varphi + B \cos\varphi,$$

where $$A = h_2 \cos\theta_m \sin\eta - h_3 \sin\theta_m$$

$$B = h_3 \cos\theta_m \sin\eta - h_2 \sin\theta_m$$

$$C = h_1 \cos\theta_m \cos\eta.$$

I solve this by letting

$$\cos y = \frac{A}{\sqrt{A^2 + B^2}},$$

and

$$\sin y = \frac{B}{\sqrt{A^2 + B^2}}, \qquad (28)$$

since then

$$\frac{C}{\sqrt{A^2 + B^2}} = \sin\varphi \cos y + \cos\varphi \sin y,$$

$$= \begin{cases} \sin(\varphi+y) \\ \quad \text{or} \\ \sin(\varphi-\varphi-y) \end{cases}$$

so that we have the two solutions:

$$\varphi = \pi - \sin^{-1}\left[\frac{C}{\sqrt{A^2 + B^2}}\right] - \tan^{-1} (B/A), \text{ and}$$

$$\varphi = \sin^{-1}\left[\frac{C}{\sqrt{A^2 + B^2}}\right] - \tan^{-1}(B/A).$$

The pair of equations (28) uniquely define $\tan^{-1}(B/A)$, but $\pm\sqrt{A^2 + B^2}$ both solve equation (28). The two solutions arise, as shown in Figure 2.3 on page 2-6 of the BBRC Aspect Manual (1964), because reflection in a plane defined by $\vec{H}$ and $\hat{x}_s$ gives another possible wheel plane and preserves the angle between the magnetic null vector and the sun line of sight with the sense of the spin reversed. As the satellite moves about the orbit the magnetic field direction and thus the mirror plane change. I choose the correct roll angle solution by the fact that the true spin axis direction does not change and thus the mirror spin axis changes position twice as fast as the magnetic field direction.

The geometrical relationship of the magnetic field and sun directions greatly influences the accuracy of the roll angle solution. For example, with zero pitch angle, $\vec{H}$ perpendicular to the sun line implies that the null vector lies along the roll axis and the wheel angle $\Theta_m = 0$ or $= \pi$ for any roll angle φ. For $\vec{H}$ perpendicular to the sun line the wheel angle $\Theta_m = \pi/2$ for any φ. In general for small errors in Θ_m, η, or the magnetic field direction, one can estimate the error in roll angle by

$$d\varphi = \frac{\partial\varphi}{\partial\Theta_m} d\Theta_m + \frac{\partial\varphi}{\partial\eta} d\eta + \frac{\partial\varphi}{\partial\alpha} d\alpha + \frac{\partial\varphi}{\partial\beta} d\beta .$$

The angles α and β represent the azimuth and polar angle of $\vec{H}$ in ecliptic coordinates:

$$h_3 = \cos\beta,\ h_2 = \sin\beta \sin\alpha,\ h_1 = \sin\beta \cos\alpha \cdot$$

Note that errors in direction due to α and β depend on each other; if $d\Psi$ represents the angle between $\vec{H}$ and $\vec{H} + d\vec{H}$, then $(d\Psi)^2 = (d\beta)^2 + \sin^2\beta\,(d\alpha)^2$. The direction error $d\Psi \cong 1^0$, so

$$d\beta = \frac{1}{\sqrt{2}} \text{ degrees and } d\alpha = \frac{1}{\sqrt{2}\sin\beta} \text{ degrees.}$$

For favorable configurations, approximately 15 of about 150 magnetometer to sun measurements each pass give an acceptable roll solution. For acceptance I require that the roll angle differs by less than 10^0 from the previously determined roll, and that the absolute values

$$\left|\frac{\partial\varphi}{\partial\theta}_m\right| \le 1.0,\ \left|\frac{\partial\varphi}{\partial\eta}\right| \le 5.0,\ \left|\frac{\partial\varphi}{\partial\beta}\right| \le 1.0,\ \left|\frac{\partial\varphi}{\sin\beta\,\partial\alpha}\right| \le 1.0.$$

We compared the spin axis position with that calculated by the MIT OSO Group [Clark (1968)] using a least squares fit to an assumed position. When the BBRC method yields a solution, it generally agrees with the MIT position to better than 3^0. I use the MIT solutions for periods of data that do not yield a solution according to the above criteria.

One can now easily determine the celestial coordinates of the look direction defined by any angle θ in the wheel plane. In matrix notation:

$$\begin{Bmatrix} x \\ y \\ z \end{Bmatrix} = \begin{Bmatrix} 1 & 0 & 0 \\ 0 & \cos\epsilon & -\sin\epsilon \\ 0 & \sin\epsilon & \cos\epsilon \end{Bmatrix} \begin{Bmatrix} \cos S & -\sin S & 0 \\ \sin S & \cos S & 0 \\ 0 & 0 & 1 \end{Bmatrix} \cdot$$

$$\begin{Bmatrix} 1 & 0 & 0 \\ 0 & \cos\varphi & -\sin\varphi \\ 0 & \sin\varphi & \cos\varphi \end{Bmatrix} \begin{Bmatrix} \cos\eta & 0 & -\sin\eta \\ 0 & 1 & 0 \\ \sin\eta & 0 & \cos\eta \end{Bmatrix} \begin{Bmatrix} \cos\Theta \\ \sin\Theta \\ 0 \end{Bmatrix}$$

gives the components x, y, z in celestial coordinates of a unit vector in the wheel plane at an angle Θ past the projection of the sun direction.

3. Timing

Each STADAN station records about two minutes real time data from OSO-III before or after playback. By the DSM frame count, the Goddard data reduction programs provide universal time T_{mf} of a first word of main frame every 96 main frames, approximately one minute. The spacecraft clock varies from 400 cps by about one part in 5000, or about one second per pass. I use the average main frame rate R calculated each file, instead of the nominal .64000 seconds per frame. Telemetering of the California word occurs .14 seconds past the start of a main frame. The equation

$$T_{cal} = T_{mf} + N \cdot R + .14$$

gives the universal time T_{cal} of the California word appearing in the Nth main frame after the time measurement.

APPENDIX B

EFFECT OF SAMPLING PROCEDURE ON ANGULAR RESULUTION

In this discussion I distinguished between the sector of the scan circle defined by one scaler step of 37.5 milliseconds or $(360)(\frac{.0375}{T})$ degrees, where T = spin period in seconds, and the sector of the scan circle defined by the 6^{o} bins into which the analysis program accumulates counts. I refer to these as a "step" and a "sector" respectively. I take the independent variable as time, rather than angle along the scan circle; $\theta = 360\,\frac{t}{T}$ converts a time t seconds into an angle of θ degrees. The origin of either occurs at the telescope optical axis position at the time the sun gate or magnetometer pulse resets the step number to one. For both day and night data, I take the origin of the sectors at the day step reset, thus the sun position always corresponds to sector 3.7. The lack of synchronization of the steps with the spin rate causes the complications dealt with in this appendix.

Let N equal the greatest integer in T/.0375. (In a common case, T = 1.606 and N = 42). The step N always receives the full .0375 second exposure, step N + 1 receives partial or full exposure every spin, step N + 2 never receives full exposure and may have none at all, and step 1 receives zero to a maximum .0375 seconds. I thus treat steps 2 through N the same, a "normal" step, and steps 1, N + 1, and N + 2 as special cases. In general, the telemetry sampling logic becomes available to receive a count before the start of a given step, and would not telemeter until after the step has ended. I treat separately the case when

the step may have started before the sample scaler became "live." This occurs for high counting rates $\lambda(.0375) \geq \ln(2)$, or $\lambda \geq 18\ \text{sec}^{-1}$. Such a condition may prevail due to the sun, the strongest discrete sources, or the presence of charged particles.

The conditional probability density that a count arrived at the precise time Θ, given that a count does occur in the step, equals the integral over all possible times t at which the step may have started of the probability density that the step did start at t multiplied by the conditional probability density $\frac{\lambda e^{-\lambda(\Theta-t)}}{P_o}$ that if the step started at time t the first count would arrive at time Θ. P_o = the probability that a count does occur within a step, thus $P_o = 1 - e^{-.0375\lambda}$ for a normal step. I consider that λ = true count rate does not vary during a step. This assumption holds because the full width telescope aperture for half maximum response spans about three step angles, and because the density functions turn out to depend only weakly on λ for $\lambda \leq 10\ \text{sec}^{-1}$.

I assume a uniform probability density P_s for the time t at which a step starts over the time period in which it can possibly start. For a two-minute stretch of data this fails because the clock systematically displaces every step by (T - .0375 N) or [T - .0375 (N+1)] seconds on each successive spin. I can use the assumption because the telemetry accepts no more than one count per spin period, and because it holds true on the time scale of 10^5 seconds over which I average diffuse X-ray data. Thus for a normal step $P_s = \frac{1}{w}$, where w = .0375 seconds.

A normal step n starts between (n-2)w seconds after reset (for step one very short) and (n-1)w seconds after reset (step one the full .0375 seconds). Measuring θ from (n-2)w we have

$$\rho_n(\theta) = \int_{\max(0,\theta-w)}^{\min(\theta,w)} \frac{1}{w} e^{-\lambda(\theta-t)} \frac{\lambda dt}{1-e^{-\lambda w}}$$

$$= \frac{e^{-\lambda\theta}}{w(1-e^{-\lambda w})} \begin{cases} e^{\lambda\theta}-1 & \text{if } 0 \le \theta \le w \\ e^{\lambda w}-e^{\lambda(\theta-w)} & \text{if } w \le \theta \le 2w. \end{cases}$$

The lower limits of integration reflect the fact that the step could not have started before time zero or more than w seconds before the count arrived; the upper limits that the step must have started by time w or by the time the count arrived.

Let $\tau = T - .0375N$ seconds. Step N + 2 starts between .0375 N and T (given that it occurs at all), so $P_s = \frac{1}{\tau}$. However, N + 2 only lasts $\tau - t$ seconds, with t the start time measured from Nw, so

$$P_o = 1 - e^{-(\tau-t)}.$$

Thus $\rho_{N+2}(\theta) = \int_0^\theta \frac{1}{\tau} \frac{e^{-\lambda(\theta-t)} \lambda dt}{1-e^{-\lambda(\tau-t)}}$

$$= \frac{1}{\tau} e^{-\lambda(\theta-\tau)} \log \frac{1-e^{-\lambda\tau}}{1-e^{-\lambda(\tau-\theta)}}.$$

Step N+1 definitely starts at some time between (N-1)w and Nw, therefore $P_s = 1/w$. Measuring times from (N-1)w, if N+1 starts before τ, $(t \le \tau)$, it lasts w seconds and has a probability $P_o = 1 - e^{-\lambda w}$ for receiving a count. If N+1 starts after τ, $(t \ge \tau)$, it lasts a time

$w + \tau - t$ and $P_o = 1 - e^{-\lambda w} e^{-\lambda(\tau - t)}$. Using the Heaviside symbol

$$H(x) = \begin{cases} 0 & \text{if } x < 0 \\ 1 & \text{if } x \geq 0 , \end{cases}$$

$$\rho_{N+1}(\theta) = \int_{\max(\theta-w,0)}^{\min(\tau,\theta)} \frac{1}{w} \frac{e^{-\lambda(\theta-t)}}{1-e^{-\lambda w}} \lambda dt$$

$$+ H(\theta-\tau) \int_{\tau}^{\min(\theta,w)} \frac{1}{w} \frac{e^{-\lambda(\theta-t)} \lambda dt}{1-e^{-\lambda(w+\tau)} e^{\lambda t}}$$

$$= \frac{e^{-\lambda\theta}}{w(1-e^{-\lambda w})} \cdot \begin{cases} e^{\lambda\theta} - 1 & \text{if } 0 \leq \theta \leq \tau \\ e^{\lambda\tau} - 1 & \text{if } \tau \leq \theta \leq w \\ e^{\lambda\tau} - e^{\lambda(\theta-w)} & \text{if } w \leq \theta \leq w + \tau \end{cases}$$

$$+ \begin{cases} 0 & \text{if } \theta \leq \tau \\ \frac{e^{-\lambda\theta}}{w} e^{\lambda(w+\tau)} \cdot \begin{cases} \log \frac{1-e^{-\lambda w}}{1-e^{-\lambda(w+\tau)} e^{\lambda\theta}} & \text{if } \tau \leq \theta \leq w \\ \log \frac{1-e^{-\lambda w}}{1-e^{-\lambda\tau}} & \text{if } w \leq \theta \leq w + \tau. \end{cases} \end{cases}$$

Step one definitely starts at time zero, therefore I integrate over the time t at which it might turn off. I use $\frac{1}{w}$ for the uniform probability density of turning off. The probability of receiving a count, $P_o = 1 - e^{-\lambda t}$. If a count arrives at time θ, then $\theta \leq t \leq w$, and

$$\rho_1(\theta) = \int_{\theta}^{w} \frac{1}{w} \frac{\lambda e^{-\lambda\theta} dt}{1-e^{-\lambda t}} = \frac{\lambda}{w} e^{-\lambda\theta} \left[w-\theta + \frac{1}{\lambda} \log \frac{1-e^{-\lambda w}}{1-e^{-\lambda\theta}} \right] .$$

For computer analysis I use the distribution function

$$F(x) = \int_0^x \rho(\theta)\ d\theta$$

and solve for x in

$$F(x) = \text{RANF}(-1). \tag{29}$$

The UCSD Computer Center function RANF(-1) provides uniformly distributed pseudo-random numbers between 0 and 1. These distribution formulas consider x measured from the minimum time at which the given step could have turned on:

$$F_n(x) = \frac{1}{w(1-e^{-\lambda w})} \cdot \begin{cases} x+\frac{1}{\lambda}\,(e^{-\lambda x}-1) & \text{if } 0 \le x \le w \\ w+e^{-\lambda w}(\frac{1}{\lambda}+w-x) - \frac{1}{\lambda}\,e^{-\lambda(x-w)} & \text{if } w \le x \le 2w \end{cases} \tag{30}$$

where $2 \le n \le N$;

$$F_1(x) = 1-e^{-\lambda x}(1-\frac{x}{w}) + \frac{1}{w\lambda}\,(1-e^{-\lambda x})\,\log\left[\frac{1-e^{-\lambda w}}{1-e^{\lambda x}}\right] \tag{31}$$

for $0 \le x \le w$;

$$F_{N+1}(x) = \frac{1}{w(1-e^{-\lambda w})}\ [x + \frac{1}{\lambda}\,(e^{-\lambda x}-1)]$$

if $0 \le x \le \tau$;

or

$$= \frac{1}{w(1-e^{-\lambda w})}\ [\tau - \frac{1}{\lambda}\,e^{-\lambda x}(e^{\lambda \tau}-1)] + \frac{e^{\lambda(w+\tau)}}{w}\left\{xe^{-\lambda x}\right.$$

$$\left. - \tau e^{-\lambda(w+\tau)} + \frac{1}{\lambda}\,(e^{-\lambda x} - e^{-\lambda(w+x)})\,\log\left[\frac{e^{-\lambda x}-e^{-\lambda(w+\tau)}}{1-e^{-\lambda w}}\right]\right\}$$

if $\tau \le x \le w$,

or

$$= \frac{e^{\lambda(w+\tau)}}{\lambda w} \left(e^{-\lambda x} - e^{-\lambda(w+\tau)}\right) \log \frac{1-e^{-\lambda\tau}}{1-e^{-\lambda w}} + 1 - \frac{\tau}{w}$$

$$+ \frac{1}{w\left(1-e^{-\lambda w}\right)} \left[\tau - e^{-\lambda w}\left(x-w-\frac{1}{\lambda}\right) - \frac{1}{\lambda} e^{-\lambda(x-\tau)}\right] \qquad (32)$$

$$\text{if } w \le x \le w+\tau \ ;$$

$$F_{N+2}(x) = \left[\left(e^{-\lambda\tau} - e^{-\lambda x}\right) \log \left[\frac{1-e^{-\lambda\tau}}{e^{-\lambda x} - e^{-\lambda\tau}}\right] + \lambda x e^{-\lambda x}\right] \frac{e^{\lambda\tau}}{\lambda\tau} \qquad (33)$$

$$\text{for } 0 \le x \le \tau \ .$$

Note the normalization, F=0 for $x \le 0$, and F = 1 for $x \ge 2w$, w, $w + \tau$, or τ, the respective maximum times at which the count could occur.

When the step could begin before the telemetry became live, then P_s, P_o, and the limits of integration all depend on the possible live exposure time of the step. I derive and use the distribution functions for the seven different possibilities. These functions depend very weakly on λ. When the aspect solution reveals that a step in which a count occurred might not have received full exposure before telemetering, then another special set of probability density functions apply. For simplicity, I assume that the step did receive normal exposure, since with λ = 1.0 to 3.0 the probability of not receiving a count until the end of the telemetry sampling period does not exceed 1.0 to .01 percent, and because in this case the live time of 1.26 or 1.90 seconds greatly exceeds the maximum possible timing error of .0375 seconds.

For each count the computer routine generates a random number. It then solves equation (29) using the appropriate distribution function by incrementing x in .0025 second intervals until F ≥ RANF(-1). I then assign x as the arrival time of the count. For the usual case normal step, equation (30), I approximate the density by a discontinuous triangular density

$$\rho'(\theta) = \begin{cases} \alpha\theta & \text{if } 0 \le \theta \le w \\ \beta\,(2w-\theta) & \text{if } w \le \theta \le 2w. \end{cases}$$

I choose α and β for normalization,

$$1 = \int_0^{2w} \rho'(\theta)\, d\theta ,$$

and so that ρ' gives the same expectation value for live time within the step,

$$< t > = \int_0^{2w} t\rho_n(t)\, dt = \frac{w}{2} + \frac{1}{\lambda} - \frac{w}{e^{\lambda w}-1} = \int_0^{2w} t\rho'(t)dt.$$

These imply

$$\alpha = \frac{2}{w^2} - \beta \text{ and } \beta = \frac{1}{w^2}\left(\frac{3}{\lambda w} - \frac{3}{e^{\lambda w}-1} - \tfrac{1}{2}\right).$$

This approximation transforms equation (29) to a quadradic equation, with an exact solution for x. Figure 42 illustrates the validity of the triangular response for $\lambda \le 10$ sec^{-1}.

An ambiguity exists for counts arriving in steps which occur within (1.90-T) seconds after the telemetry becomes live. For $\lambda \tilde{=} 1.0$, the telescope had a reasonable chance of making one complete spin scan before receiving the count. I treat this as any other count, but also

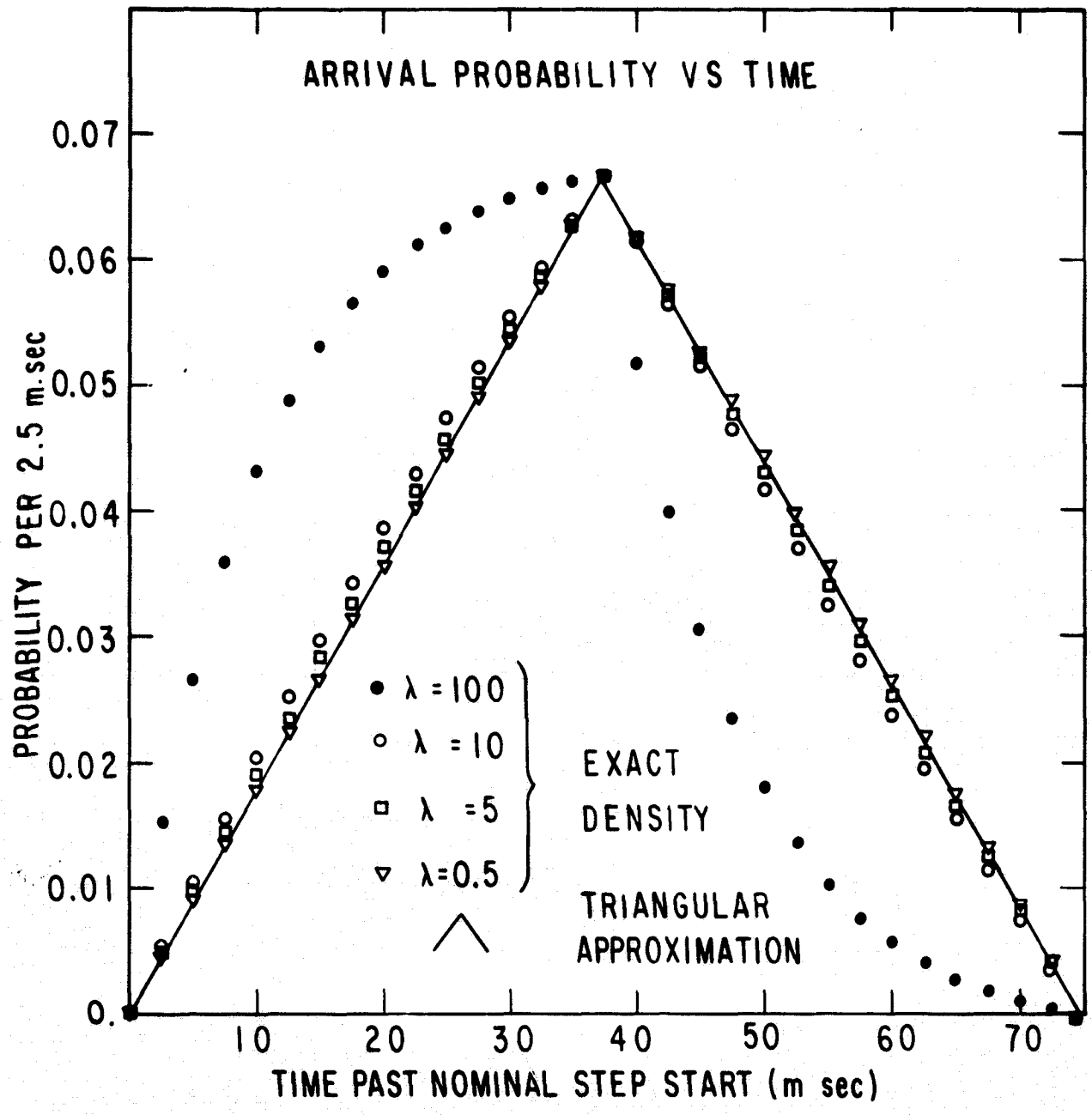

Fig. 42 Probability density for the exact arrival time as a function of time past when the scaler step might have started. Points represent the exact calculation; solid line represents the approximate function used in data analysis.

add $(T/60)(1-e^{-\lambda T})$ seconds to every sector.

For the direction of arrival I smear the count over all sectors included in the step by adding the difference of the distribution functions at the times corresponding to the end and beginning of the sector.

Generally, I simply take λ equal to the total counts received divided by the 115.2 second energy channel time. During a sun event I use a different λ for each of the first seven sectors, based on the sun gate rate and the effective solar exposure for the sector. For the remaining sectors I either correct the total counts for the solar contribution, possible only during small events, or merely use a fixed λ based on the diffuse component count rates determined for each energy channel during some preliminary analysis runs.

In the presence of charged particle fluxes greater than 36 sec^{-1} the routine uses the rate determined by the sun gate for the given energy channel, since the total counts will overflow the 12-bit register in 115 seconds. When $\lambda \geq 20$ sec^{-1} the errors in solving equation (29) and the breakdown of the assumption of a constant λ within a step cause systematic overestimation of the live time.

I calculate the expected live time and variance for each sector energy channel, assuming λ gives the true time average counting rate. In the two minutes there occur 30 samples which may last 1.90 seconds and 30 which may last 1.26 seconds.

$$< t > = 30[1.9e^{-1.9\lambda} + \int_0^{1.9} t\ \lambda e^{-\lambda t}\ dt]$$

$$+ 30[1.26e^{-1.26\lambda} + \int_0^{1.26} t\ \lambda e^{-\lambda t}\ dt]$$

$$= \frac{1}{\lambda}\ [60 - 30\ (e^{-1.9\lambda} + e^{-1.26\lambda})];$$

$$\sigma^2 = <t^2> - <t>^2 = \frac{1}{\lambda^2}\ [60 - 60\lambda\ (1.9e^{-1.9\lambda} + 1.26e^{-1.26\lambda})$$

$$- 30(e^{-2\lambda(1.9)} + e^{-2\lambda(1.26)})].$$

The analysis program rejects sector energy channels for which the deduced live time varies by more than 3σ from $< t >$.

Figure 43 illustrates the discrete source contamination problems. The bottom line gives the fixed sector positions, the middle line a set of step intervals. At various times a given step may start anywhere within its own interval, thus ending anywhere in the next interval. Thus steps k, k + 1, and k + 2 all contribute counts to sector j. A discrete source on the scan plane 18° away from a step edge can contribute 2 percent of its strength to that step. Thus, a strong source at point A can contribute to step k, and a source at C to step k + 2, so a 76° band along the scan plane must be free of sources to assure that sector j has less than 1 percent contamination.

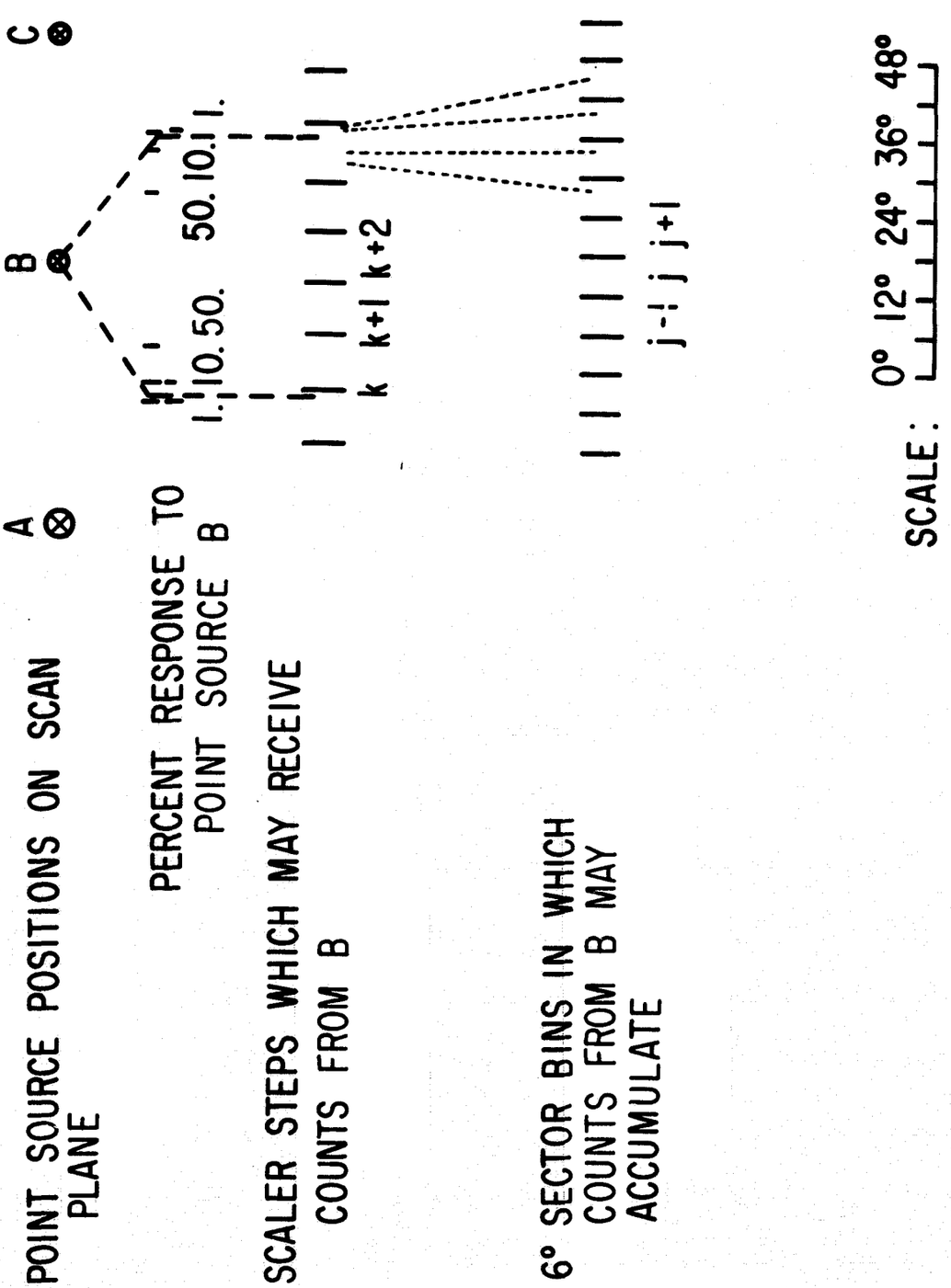

Fig. 43 One percent of the counts from B may accumulate in scaler steps k-1 or k+4, and thus become smeared from bin j-4 to bin j+5. Sources A or C can contribute one percent of their count rate to bin j.

REFERENCES

Arnold, J. R., Metzger, A. E., Anderson, E. C., and Van Dilla, M. A. 1962, J. Geophys. Res., 67, 4878.

Ball Brothers Research Corporation 1963, TM63-1.

_____. 1964 (private communication).

_____. 1966, TN65-315.

Bergamini, R., Londrillo, P., and Setti, G. 1967, Nuovo Cimento, 52B, 495.

Birks, J. B. 1964, The Theory and Practice of Scintillation Counting (New York: The MacMillan Company).

Blatt, J. M., and Weisskopf, V. F. 1952, Theoretical Nuclear Physics (New York: John Wiley and Sons), pp. 673-684.

Bleeker, J. A. M., Burger, J. J., Deerenberg, A. J. M., Scheepmaker, A., Swanenburg, B. N., Tanaka, Y., Hayakawa, S., Makino, F., and Ogawa, H. 1968, Canadian J. Phys., 46, S461.

Bleeker, J. A. M., and Deerenberg, A. J. M. 1969 (preprint, submitted to Ap. J.).

Bok, B. J. 1966, Ann. Rev. Astr. and Ap., 4, 95.

Boldt, E. A., Desai, U. D., Holt, S. S., and Serlemitsos, P. J. 1969, I. A. U. Symp. No. 37 (in press).

Bowyer, S., Byram, E. T., Chubb, T. A., and Friedman, H. 1964, Science, 146, 912.

Bracewell, R. N., and Roberts, J. A. 1954, Aust. J. Phys., 7, 615.

Brecher, K., and Morrison, P. 1969 (preprint, submitted to Ap. J.).

Brouwer, D. 1959, A. J., 64, 378.

Bunner, A. N., Coleman, P. C., Kraushaar, W. L., McCammon, D., Palmieri, T. M., Shilepsky, A., and Ulmer, M. 1969 (preprint).

Burnight, T. R. 1949, Phys. Rev., 76, 165.

Chodil, G., Mark, H., Rodrigues, R., Seward, F., Swift, C. D., Hiltner, W. A., Wallerstein, G., and Mannery, E. J. 1967, Phys. Rev. Letters, 19, 681.

Clark, G. 1968 (private communication).

Clark, G. W., Garmire, G. P., and Kraushaar, W. L. 1968, Ap. J. (Letters), 153, L203.

Clark, G. W., Lewin, W. H. G., and Smith, W. B. 1968, Ap. J., 151, 21.

Compton, A. H., and Getting, I. A. 1935, Phys. Rev., 47, 817.

Conklin, E. K. 1969, Nature, 222, 971.

Conklin, E. K., and Bracewell, R. N. 1967, Phys. Rev. Letters, 18, 614.

Cooke, B. A., Griffiths, R. E., and Pounds, K. A. 1969 (preprint, submitted to Nature).

de Vaucouleurs, G. 1953, A. J., 58, 30.

_____.1958, A. J., 63, 253.

Ducros, G., Ducros, R., Rocchia, R., and Tarrius, A. 1969 (preprint).

Escobal, P. R. 1965, Methods of Orbit Determination (New York: John Wiley and Sons).

Fanselow, J. L. 1968, Ap. J., 152, 783.

Felten, J. E. 1965, unpublished Ph. D. thesis, Cornell University.

Felten, J. E., and Gould, R. J. 1966, Phys. Rev. Letters, 17, 401.

Felten, J. E., and Morrison, P. 1966, Ap. J., 146, 686.

Felten, J. E., and Rees, M. J. 1969, Nature, 221, 924.

Freden, S. C. 1969, Space Sci. Rev., 9, 198.

Freier, P. S., and Waddington, C. J. 1968, J. Geophys. Res., 73, 4261.

Friedman, H., Byram, E. T., and Chubb, T. A. 1967, Science, 156, 374.

Garfinkel, B. 1959, A. J., 64, 353.

Giacconi, R., Gursky, H., Paolini, F., and Rossi, B. 1962, Phys. Rev. Letters, 9, 439.

Gleeson, L. J., and Axford, W. I. 1968, Ap. and Space Sci., 2, 431.

Gorenstein, P., Gursky, H., and Garmire, G. 1968, Ap. J., 153, 885.

Gorenstein, P., Kellogg, E. M., and Gursky, H. 1969, Ap. J., 156, 315.

Gould, R. J. 1965, Phys. Rev. Letters, 15, 511.

_____. 1967, Amer. J. of Phys., 35, 376.

Gould, R. J., and Burbidge, G. R. 1963, Ap. J., 138, 969.

_____. 1965, Ann. d'ap., 28, 171.

Green, D. W., Wilson, B. G., and Baxter, A. J. 1968, in Space Research IX, ed. K. S. W. Champion, P. A. Smith, and R. L. Rose-Smith (Amsterdam: North-Holland Publishing Company), p. 222.

Guest, P. G. 1961, Numerical Methods of Curve Fitting (Cambridge: Cambridge University Press).

Gursky, H., Giacconi, R., Gorenstein, P., Waters, J., Oda, M., Bradt, H., Garmire, G., and Sreekantan, B. V. 1966, Ap. J., 144, 1249.

Hassitt, A., and McIlwain, C. E. 1966, "Guide for the Use of the B and L Programs," (unpublished note).

Hayakawa, S., Matsuoka, M., and Sugimoto, D. 1966, Space Sci. Rev., 5, 109.

Haymes, R. C., Ellis, D. V., Fishman, G. J., Kurfess, J. D., and Tucker, W. H. 1968, Ap. J. (Letters), 151, L9.

Hendricks, S. J., and Cain, J. C. 1966, J. Geophys. Res., 71, 3467.

Henry, R. C., Fritz, G., Meekins, J. F., Friedman, H., and Byram, E. T. 1968, Ap. J. (Letters), 153, L11.

Hicks, D. B., Reid, L., Jr., and Peterson, L. E. 1965, IEEE Trans. Nucl. Sci., NS-12, 54.

Hudson, H. S., Peterson, L. E., and Schwartz, D. A. 1969a (preprint, submitted to Ap. J.).

_____. 1969b, Ap. J., 157, 389.

_____. 1969c, Solar Phys., 6, 205.

Hudson, H. S., Primbsch, J. H., and Anderson, K. A. 1966, J. Geophys. Res., 71, 5665.

Hudson, H. S., Schwartz, D. A., and Peterson, L. E. 1967, Bull. Am. Phys. Soc., 12, 1066.

Hudson, H. S., Schwartz, D. A., and Peterson, L. E. 1968a, A. J., 73, 5.

_____. 1968b, Trans. AGU, 49, 274.

Hudson, H. S., Schwartz, D. A., Peterson, L. E., Zirin, H., and Ingham, W. H. 1968c, Trans. AGU, 49, 725.

Jacobson, A. S. 1968, unpublished Ph. D. thesis, University of California, San Diego.

Jacobson, A. S., and Peterson, L. E. 1969 (in preparation).

Kozai, Y. 1959, A. J., 64, 367.

_____. 1964, Smithsonian Astrophysical Observatory Spec. Rept. No. 165.

Liden, K., and Starfelt, N. 1954, Ark. f. Fys., 7, 427.

Mark, H., Price, R., Rodrigues, R., Seward, F. D., and Swift, C. D. 1969, Ap. J. (Letters), 155, L143.

Matsuoka, M., Oda, M., Ogawara, Y., Hayakawa, S., and Kato, T. 1968, Canadian J. Phys., 46, S466.

Metzger, A. E., Anderson, E. C., Van Dilla, M. A., and Arnold, J. R. 1964, Nature, 204, 766.

Morrison, P. 1958, Nuovo Cimento, 7, 858.

_____. 1967, Ann. Rev. Astr. and Ap., 5, 325.

Oda, M., Bradt, H., Garmire, G., Spada, G., Sreekantan, B. V., Gursky, H., Giacconi, R., Gorenstein, P., and Waters, J. R. 1967, Ap. J. (Letters), 148, L5.

Partridge, R. B., and Wilkinson, D. T. 1967, Phys. Rev. Letters, 18, 557.

Penzias, A. A., Schraml, J., and Wilson, R. W. 1969, Ap. J. (Letters), 157, L49.

Peterson, L. E. 1965, J. Geophys. Res., 70, 1762.

_____. 1968, UCSD-SP 68-1.

_____. 1969, I. A. U. Symp. No. 37 (in press).

Peterson, L. E., Hudson, H. S., and Schwartz, D. A. 1967, UCSD-SP 67-10.

Peterson, L. E., and Schwartz, D. A. 1969 (in preparation).

Peterson, L. E., and Winckler, J. R. 1959, J. Geophys. Res., 64, 697.

Rees, M. J. 1967, M. N. R. A. S., 137, 429.

Rocchia, R., Rothenflug, R., Boclet, D., Ducros, G., and Labeyrie, J. 1966, Space Research VII, ed. R. L. Smith-Rose (Amsterdam: North-Holland Publishing Company), p. 1327.

Sachs, R. K., and Wolfe, A. M. 1967, Ap. J., 147, 73.

Savedoff, M. P. 1959, Nuovo Cimento, 13, 12.

Schwartz, D. A., Hudson, H. S., and Peterson, L. E. 1967, Bull. Am. Phys. Soc., 12, 1058.

_____. 1968a, UCSD-SP 67-11.

_____. 1968b, Trans. AGU, 49, 720.

Seward, F., Chodil, G., Mark, H., Swift, C., and Toor, A. 1967, Ap. J., 150, 845.

Silk, J. 1968, Ap. J. (Letters), 151, L19.

Smart, D. F., and Shea, M. A. 1967, J. Geophys. Res., 72, 3447.

Stewart, J. M., and Sciama, D. W. 1967, Nature, 216, 748.

Vette, J. I., Lucero, A. B., and Wright, J. A. 1966, NASA SP-3024.

Vette, J. I., Matteson, J. L., Gruber, D., and Peterson, L. E. 1969, I. A. U. Symp. No. 37 (in press).

Weintraub, S. 1963, Tables of the Cumulative Binomial Probability Distribution for Small Values of p (London: Collier-MacMillan Limited).

Wolfe, A. 1969, Ap. J., 156, 803.